

EllipseFit

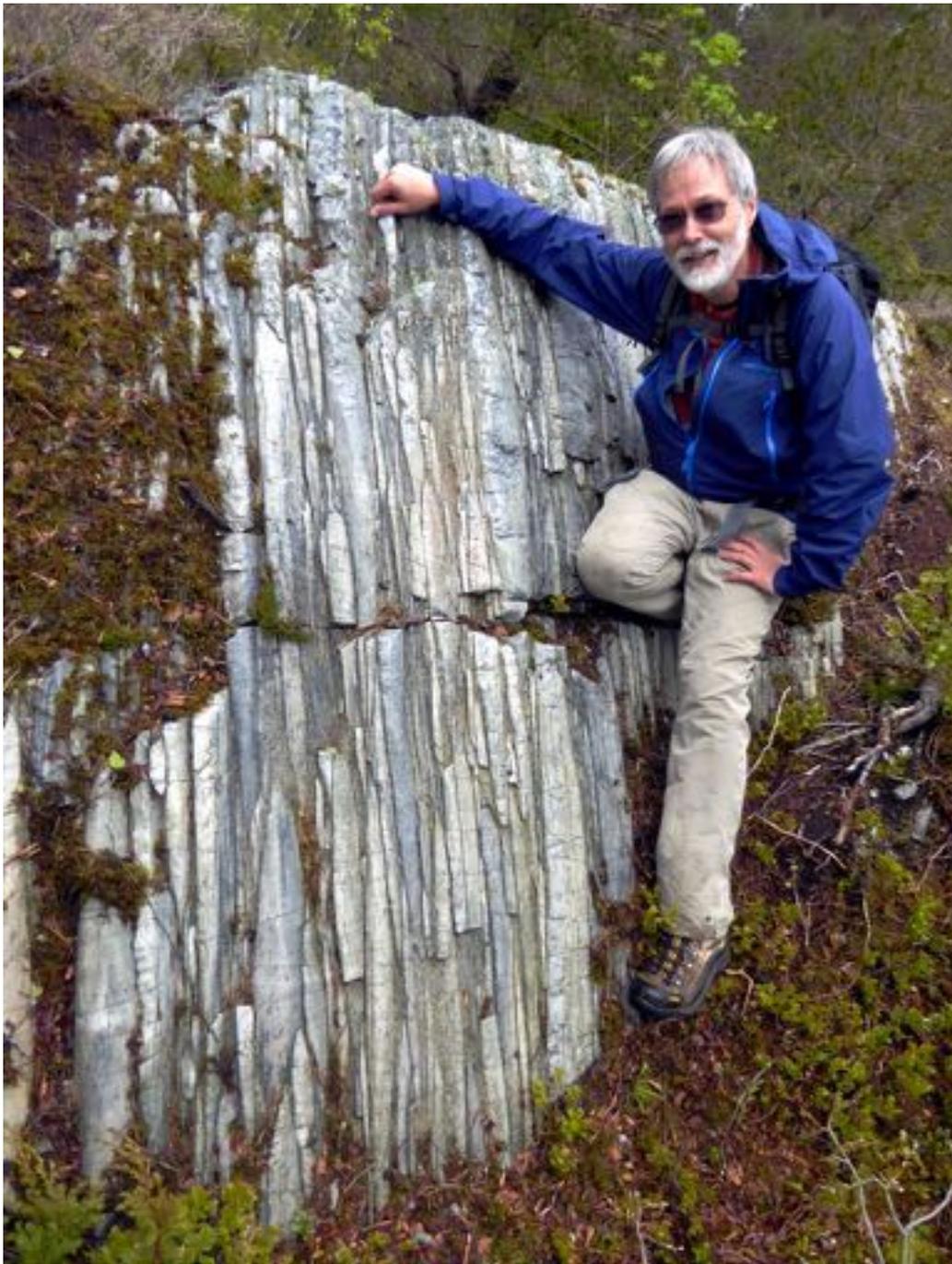
Fabric and Strain Analysis Software

Frederick W. Vollmer

Version 3.11.0
November 27, 2022



This page intentionally left blank



Frontispiece: Strained quartz cobble conglomerate at Sandviksfjellet, Bergen, Norway. The formation is folded and highly deformed, here prolate, cigar-shaped, cobbles indicate a strong constrictional strain (Holst and Fossen, 1987; Fossen, 1988). Photograph by E. Lubicich.

Cover: Bygden conglomerate, deformed beneath the Jotun Nappe, Bygdin area, Norway, locality of the classic strain study of Hossack (1968). Photograph by F.W. Vollmer.

Preface

License

EllipseFit software and accompanying documentation are Copyright © Frederick W. Vollmer. They come with no warranties or guarantees of any kind. The software is free and may be downloaded and used without cost, however the author retains all rights to the source, binary code and accompanying files. It may not be redistributed or posted online. The only stipulation for usage is that citation be given for any usage that leads to publications or presentations.

The software is provided "as is", without warranty of any kind, express or implied, including but not limited to the warranties of merchantability, fitness for a particular purpose and noninfringement. In no event shall the authors or copyright holders be liable for any claim, damages or other liability, whether in an action of contract, tort or otherwise, arising from, out of or in connection with the software or the use or other dealings in the software.

Citation

EllipseFit is the result of countless hours of work for over several decades. Algorithms used in the program come from numerous sources, which I have attempted to cite properly, however many have been developed by the author. Some of these have not yet been published and are the subject of papers in preparation. The program is released freely with the hope that the structure and tectonics community will find it useful, and will respect priority of unpublished algorithms.

In return for free use, use of the software for digitizing, analyzing data, or preparing diagrams should be cited in publications, presentations, or other works. Please cite the following, which contains the core projection and contouring algorithms:

Vollmer, F.W., 2018. Automatic contouring of geologic fabric and finite strain data on the unit hyperboloid. *Computers & Geosciences*. <http://dx.doi.org/10.1016/j.cageo.2018.03.006> .

and any of the following as appropriate:

Vollmer, 2019. Calculation of the best-fit homogeneous strain from a displacement using a displacement stretch plot and strain probe theory. *Geological Society of America Abstracts with Programs*, v. 51, n. 5, doi: 10.1130/abs/2019AM-340051.

Vollmer, F. W., 2018. Automated calculation and error analysis of fabric and strain ellipsoids from multiple section data. *Geological Society of America Abstracts with Programs*. Vol. 50, No. 6, ISSN 0016-7592 doi: 10.1130/abs/2018AM-324674.

Vollmer, F.W., 2017. Software for the quantification, error analysis, and visualization of strain and fold geometry in undergraduate field and structural geology laboratory experiences. *Geological Society of America Abstracts with Programs*, v. 49, n. 2. doi: 10.1130/abs/2017NE-291027.

Vollmer, F.W., 2011. Best-fit strain from multiple angles of shear and implementation in a computer program for geological strain analysis. *Geological Society of America Abstracts with Programs*, v. 43, n. 1, p. 147.

Vollmer, F.W., 2010. A comparison of ellipse-fitting techniques for two and three-dimensional strain analysis, and their implementation in an integrated computer program designed for field-based studies. Abstract T21B-2166, Fall Meeting, American Geophysical Union, San Francisco, California.

Registration

Please consider registering the software, registration is free and helps determine the software usage and justify the time spent in it's upkeep. To register, simply send an email to me at vollmerf@gmail.com with your user name, affiliation, and usage. I will send you an email in reply with my thanks, and will

not place you on a mailing list. For example, send me an email with something like:

User: Frederick Vollmer

Affiliation: SUNY New Paltz, Geology Department

Usage: Undergraduate structural geology course and research

The author is happy to take emails with questions and suggestions, either at the university (SUNY New Paltz) or at the gmail address used on his website. However he is not reliable about checking email, so please forgive him if he is slow in answering, he will try to respond in as timely a fashion as possible.

Installation

EllipseFit runs on the majority of modern desktop computers. It is compiled for 64 bit macOS, Windows (Intel), and Linux Ubuntu (Intel) operating systems, and is currently tested on macOS 10.13, 12.1, Windows 7, and Ubuntu 18.04. There are two versions for macOS, if you have a newer M1 (Silicon) Mac, download the ARM version which will be substantially faster.

On Macintosh macOS, double click the disk image file (dmg), and drag the EllipseFit application to your *Applications* folder, or other desired location. Do not try to run the software from the disk image installation window, it must be moved to another location on your computer. The Example Data folder can then also be copied to the same location.

Gatekeeper in macOS must be set to allow applications other than from the *App Store* to be opened. To do so, open the macOS *System Preferences* and the *Security & Privacy* option. Under *General* select *Allow apps downloaded from: Anywhere*. If that is not available, try *App Store and identified developers*. The first time you run EllipseFit *Control-Click* on the icon, and select *Open*. In recent versions of macOS, Apple has become increasingly strict about requiring developers to register. This requires a \$99 annual fee, which I am reluctant to pay as a free software developer. If you can not run EllipseFit, please let me know, including any error messages, and details of your system, from "About This Mac".

On Windows, unzip the zip file using the *Extract All* option, and drag the EllipseFit application to any desired location. Make sure to entirely extract EllipseFit from the zip file, this is the most common installation problem. The Example Data folder can also be copied to the same location.

On Linux (Ubuntu) unpack the tar file (tgz), and copy EllipseFit to any desired location. The Example Data folder can be copied to the same location.

The Example Data folder contains example data and images, these are referred to in this guide. After installing a new version, if any problems arise try starting EllipseFit while holding down the *Shift* key. This will allow resetting the preferences to default values. The preferences are stored in the file EllipseFit.json, which is located in the folder EllipseFit in your operating system's application preferences folder. To deinstall simply delete the EllipseFit application, and optionally delete the preference folder. No other files are installed. No administrative permissions are required to install EllipseFit, and it is possible to keep a copy on a thumb drive to run on any computer.

I can email SHA-256 hash files for any download package if required. These can be used to verify the package integrity, i.e., that it has not been modified and is the same file that was uploaded by the author.

Contents

1	Introduction	1
1.1	Overview	1
1.2	Symbols and Fields	3
2	Data Entry and Export	5
2.1	Data Files	5
2.1.1	Spreadsheet Files	5
2.1.2	Example Data Files	6
2.1.3	Crystal Size Distribution Files	7
2.2	Digitizing	7
2.2.1	Coordinate System	7
2.2.2	Center Point	8
2.2.3	Ellipse Axes	8
2.2.4	5-Point Ellipse	8
2.2.5	Quadrilateral	8
2.2.6	Shape	8
2.2.7	Filled Shape	9
2.2.8	Line Pair	9
2.2.9	Line	9
2.2.10	Centered Ellipse	9
2.3	Graphics Export	9
3	Point Distribution Analysis	12
3.1	Fry Analysis	12
3.2	Normalization	17
3.3	Objective Void Fitting	19
3.3.1	Enhanced	19
3.3.2	Delaunay Neighbors	22
3.3.3	Density Contrast	26
3.3.4	Exponential Edge Detection	28
3.3.5	Mean Log Likelihood	32
3.3.6	Weighted Least-Squares	34
3.3.7	Error Analysis	38
3.3.8	Comparison of Void Fitting Methods	38
4	Strain from Displacements	41
4.1	Displacement Stretch Plot	41
4.2	Strain Probe	44
4.3	Comparison of Methods	46
4.4	Strain from Velocities	46
5	Line Data Analysis	50
5.1	Wellman Analysis	50
5.2	Line Stretch Analysis	53
5.3	Apparent Dip Analysis	55
6	Ellipse and Shape Analysis	57
6.1	Moment Ellipses	58
6.2	Ellipse Plots	58
6.2.1	Elliott Polar Plot	59
6.2.2	R_f/ϕ Plot	59

6.2.3	Hyperbolic Plots	60
6.2.4	Cloos Plot	62
6.3	Contouring Fabric Data	62
6.3.1	Equal-Area Fabric Plot	63
6.4	Fabric Anisotropy	64
6.5	Mean Ellipse Calculation	64
6.5.1	Simple Means and Centroids	64
6.5.2	Shape Matrix Eigenvector	65
6.5.3	Mean Radial Length	65
6.5.4	Hyperbolic Vector Mean	65
6.5.5	Comparison of Mean Calculations	66
6.6	Error Analysis	66
6.7	Data Transformation	67
6.8	Data Synthesis	67
7	Fabric and Strain Ellipsoids	68
7.1	Ellipsoid Plots	68
7.1.1	Flinn-Ramsay Plot	68
7.1.2	Nadai-Hsu Plot	69
7.1.3	Shade Plot	71
7.2	Global Coordinates and Sample Collection	72
7.3	Ellipsoid Calculation	73
7.3.1	Robin Method	74
7.3.2	Shan Method	74
7.3.3	Comparison of Ellipsoid Methods	75
7.3.4	Lineation Data	76
7.4	Error Analysis	77
7.4.1	Monte Carlo With Section Data	78
7.4.2	Monte Carlo Without Section Data	82
7.4.3	Bootstrap With Section Data	86
7.4.4	Bootstrap With Section Resamples	88
8	Image Processing	90
8.1	Edge Fabric Ellipse	90
8.2	Filters and Edge Detection	92
8.2.1	Image Filters	92
8.2.2	Edge Detection	92
	Acknowledgements	94
	References	94

1 Introduction

EllipseFit is an integrated program for geological fabric and strain analysis. It is used for determining two and three-dimensional fabric from oriented photographs, and is designed for field and laboratory based structural geology studies. The graphical interface and multi-platform deployment make it ideal for introductory or advanced structural geology laboratories. The software is used at numerous universities, including the author's home institution, where many hundreds of students have used it in laboratory and field studies.

The EllipseFit project was begun in order to integrate diverse techniques for all stages of a study, from data collection to three-dimensional strain calculation. Hundreds of graphical and mathematical techniques have been devised and implemented on various platforms, including Excel, Fortran, MATLAB, Mathematica, R, Python, Java, and other languages making it challenging to have access to many of them. The natively compiled binaries used for EllipseFit are very fast, and allow the implementation of error analysis using computationally intensive bootstrap techniques, making it much easier to evaluate solutions.

Early versions of the EllipseFit code were written in 1983 in Fortran, and later translated into C++. EllipseFit 2, a full rewrite released in 2010, was widely used, including for a workshop at the 2012 Structural Geology and Tectonics Forum at Williams College. EllipseFit 3 was a full rewrite using a much faster cross-platform compiler. It was used for a strain analysis workshop at the 2014 Structural Geology and Tectonics Forum, at the Colorado School of Mines with Paul Karabinos and Matty Mookerjee, and has been adopted at many universities for teaching and research.

The author is a professor of structural geology, who has taught for over 30 years at SUNY New Paltz. He had the good fortune to be introduced to analytical structural geology as a student, and is particularly grateful to mentors Rob Twiss, Win Means, and Peter Hudleston whose clear thinking inspired him. He was introduced to programming as a grade school student, when his dear mother required him to take a summer school course. He subsequently joined the Computer Club, one of three members, spent countless hours on a terminal connected remotely to a "mainframe", and became obsessed with coding.

1.1 Overview

When attempting to unravel the geometry and origins of geologic structures in regions or mountain belts, a geologist starts with a hand sample or a single outcrop. The lithology, textures, and mineralogy give clues about their sedimentary, igneous, and metamorphic history. Geologists have devised numerous techniques, such as high resolution chemical and isotopic analyses, paleomagnetism, and geochronology, to extract additional information, these are commonly used in concert to piece together the Earth's history and inner workings. Finite strain analysis is one such technique that is used to unravel the deformation history, a critical piece of the puzzle.

Geological strain analysis and theory is an important aspect of structural geology that is covered in numerous textbooks (Ramsay, 1967; Means, 1976; Hobbs et al., 1976; Marshak and Mitra, 1988; Van der Pluijm and Marshak, 2004; Pollard and Fletcher, 2005; Twiss and Moores, 2007; Ragan, 2009; Davis et al., 2011; Fossen, 2016). Ragan (2009) and Ramsay and Huber (1983) provide excellent overviews of techniques for the analysis of strain in deformed rocks. Two dimensional strain markers can be grouped into four general categories:

- Points - Collections of objects whose spacial arrangement defines a fabric.
- Geometric - Objects or groups of objects with known pre-strain geometries.
- Ellipses - Objects whose shapes can be approximated by ellipses.
- Shapes - Closed polygons or curves outlining arbitrarily shaped objects.

The analysis of *points* (Chapter 3) includes Fry (Fry, 1979) and nearest neighbor (Ramsay, 1967) methods. These are based on the assumption of an initially uniform distribution of particles with a cutoff distance, commonly twice the average particle radius. Points are the simplest type of data, however, it can be difficult to objectively extract strain from point distributions. Numerous procedures are

provided for this type of analysis, including objective void fitting. In deformation experiments, slope creep studies, and continental scale deformation surveys, strains or strain-rates may be determined from the *displacements* of survey markers (Robin, 2019), this is covered in Chapter 4.

Geometric methods apply to fossils and other objects of known pre-strain geometry, including line lengths and angles, to which equations of finite strain can be applied (Ramsay, 1967; Ramsay and Huber, 1983; Ragan, 2009). These techniques are useful for specific locations or samples (Wellman, 1962; Waldron, 1988), but are less broadly applicable. The analysis of line data depends on the known initial lengths of, or angles between, lines, and is important for some data sets, such as deformed fossils (Chapter 5).

Methods using *ellipses* to approximate the shapes of particles, such as clasts in sandstones and conglomerates, have been widely used, and include graphical and analytical techniques (Cloos, 1947, 1971; Ramsay, 1967; Elliott, 1970; Shimamoto and Ikeda, 1976; Ramsay and Huber, 1983; Lisle, 1985). Common two-dimensional graphical techniques include R_f/ϕ and Elliott polar plots. These techniques assume that the particles come from a population of randomly oriented ellipses with a range of initial shapes, and that deformation has modified that distribution. These methods are covered in Chapter 6, which includes the analytical calculation of fabric means and their statistical evaluation.

Particles of *any shape*, such as irregular clasts and fossils, can be analyzed with the same methods used for ellipses, providing that the shapes were initially randomly oriented, and that the shapes are transformed into equivalent ellipses (Mulchrone and Choudhury, 2004; Yamaji, 2013; Yamaji and Maeda, 2013). This allows the use of a wide variety of particles for fabric and strain analysis, including those making up breccias and fossil hashes. The term *moment ellipse* is used here to distinguish such an ellipse from an ellipse derived using other methods, such as least-squares fitting, which is not recommended.

It has been shown that the common two-dimensional fabric plots, including R_f/ϕ and Elliott polar plots, are subcategories of a family of hyperboloidal projections (Yamaji, 2008, 2013; Vollmer, 2018b), which are analogous to the spherical projections used to create stereonet (Wulff nets) and equal-area (Schmidt) nets. Other hyperboloidal projections have useful properties for strain analysis, such as the *equal-area fabric plot*, which is recommended when the density distribution is important. It is possible to objectively contour fabric data on these projections (Vollmer, 2018b), using a procedure analogous to that used for directional orientation data (Vollmer, 1995).

Chapter 7 covers *ellipsoid* calculation and three-dimensional fabrics. This includes Flinn-Ramsay, and Nadia-Hsu plots used to display ellipsoid data, and the more complex steps involved in determining three-dimensional fabric and strain ellipsoids from oriented sections for which the two-dimensional strain ellipse has been determined. Error analysis techniques are discussed with example calculations of confidence intervals.

Chapter 8 discusses *image analysis* techniques, including the calculation of *edge fabric ellipses* (Glazner and Walker, 2020), filtering and edge detection, that can aid in highlighting particle edges prior to digitizing.

It is essential to be aware of the assumptions involved in strain analysis. In general, a sample of particles can be analyzed to determine a rock fabric, but interpreting the fabric as a strain requires certain assumptions, which may be difficult to evaluate. One important consideration is whether particles, such as fossils or clasts, record the same deformation as the rock. In particular, this may not be true if there was a viscosity contrast between the particles and the matrix that encloses them. Using both point and ellipse methods may help to resolve this.

A second problem to consider is whether there was an initial preferred orientation of particles, such as a primary fabric due to sedimentation or compaction. Unimodal, or orthogonal, sedimentary fabrics are equivalent to a homogeneous transformation that is indistinguishable from a tectonic strain. Mathematically, the superposition of two homogeneous transformations results in a homogeneous transformation, which is impossible to decompose without additional information. The topic of initial fabrics is discussed in Sections 6.3 and 6.4. Similarly, volume change, or dilatation, is difficult to quantify, and is often assumed to be zero. This may not be correct (Goldstein et al., 1998), and has various consequences for strain analysis, but it should not effect the measurement of strain ratios, the

most common measure of deformation.

1.2 Symbols and Fields

Table 1.1 lists the symbols used in this manual, and the corresponding field, if displayed, in the data spreadsheet window and corresponding data files. The fields are case independent variable names using alphanumeric characters (A..Z, 0..9, etc.), used when reading and writing data files (Section 2.1). The fields that are calculated (read only) are indicated by a checkmark in the *Calc* column. By default, each data column is displayed when corresponding data is available. The *Data columns* command can be used to change the default behavior, and hide or show individual columns.

Symbol	Column	Calc	Definition
	<i>ID</i>		Unique integer id for measurement, added if not input.
	<i>Station</i>		Alphanumeric marker ID for determining strain from displacement.
	<i>Time ID</i>		Sequential integer ID to identify the time for a marker location.
<i>i</i>			Index of particle for ellipse calculation in a section.
<i>j</i>			Index of a section for ellipsoid calculation.
<i>k</i>			Index of ellipsoid axis, 1...3.
<i>x</i>	<i>X</i>		X coordinate of point or ellipse in local coordinates, normally parallel to strike.
<i>y</i>	<i>Y</i>		Y coordinate of point or ellipse in local coordinates, normally parallel to dip.
<i>a</i>	<i>Max</i>		Maximum radius of ellipse.
<i>b</i>	<i>Min</i>		Minimum radius of ellipse.
<i>A</i>	<i>Max</i>	(✓)	Maximum radius of ellipsoid.
<i>B</i>	<i>Int</i>	(✓)	Intermediate radius of ellipsoid.
<i>C</i>	<i>Min</i>	(✓)	Minimum radius of ellipsoid.
	<i>Area</i>	✓	Area of ellipse, $ab\pi$.
<i>b</i>			Ellipse or ellipsoid shape matrix.
<i>b</i>*			Optimal or best-fit shape matrix.
<i>R</i>	<i>R</i>	(✓)	Ellipse ratio, $R = a/b$ (calculated if <i>a</i> and <i>b</i> are input).
ϕ	<i>Phi</i>		Orientation of ellipse long axis clockwise from X axis.
<i>R_{AC}</i>	<i>Max/Min</i>	✓	Ratio of ellipsoid major axis to minor axis.
<i>R_{BC}</i>	<i>Int/Min</i>	✓	Ratio of ellipsoid major axis to intermediate axis, x axis of Flinn plot.
<i>R_{AB}</i>	<i>Max/Int</i>	✓	Ratio of ellipsoid major axis to intermediate axis, y axis of Flinn plot.
<i>k_F</i>	<i>KF</i>	✓	Shape parameter (slope) on Flinn plot, Eq 7.1.
<i>k_R</i>	<i>KR</i>	✓	Shape parameter (slope) on Ramsay plot, Eq 7.3.
\vec{g}			Image lightness gradient.
<i>h_x, h_y</i>			Image correlation/convolution kernels.
<i>S</i>			Stretch, $S = L_f/L_i$, with principle stretches $S_1 \geq S_2 \geq S_3$.
<i>e</i>			Elongation, $e = (L_f - L_i)/L_i$.
ϵ			Natural strain, $\epsilon = \ln(1 + e) = \ln(S)$.
γ_0			Natural octahedral unit shear (Eq 7.5).
ϵ_S	<i>Epsilon</i>	✓	Amount of strain, radial coordinate of Nadia-Hsu plot (Eq 7.4).
ν_S	<i>Nu</i>	✓	Symmetry of strain, polar coordinate of Nadia-Hsu plot (Eq 7.6).
θ	<i>Strike</i>		Strike of section ellipse for three-dimensional analysis.
δ	<i>Dip</i>		Dip of section ellipse for three-dimensional analysis.
<i>t₁</i>	<i>Max Dec</i>	✓	Declination (trend) of maximum axis <i>A</i> of <i>b</i> *
<i>p₁</i>	<i>Max Inc</i>	✓	Inclination (plunge) of maximum axis <i>A</i> of <i>b</i> *
<i>t₂</i>	<i>Int Dec</i>	✓	Declination (trend) of intermediate axis <i>B</i> of <i>b</i> *
<i>p₂</i>	<i>Int Inc</i>	✓	Inclination (plunge) of intermediate axis <i>B</i> of <i>b</i> *
<i>t₃</i>	<i>Min Dec</i>	✓	Declination (trend) of minimum axis <i>C</i> of <i>b</i> *
<i>p₃</i>	<i>Min Inc</i>	✓	Inclination (plunge) of minimum axis <i>C</i> of <i>b</i> *
	<i>Max 95%</i>	✓	95% confidence interval for maximum <i>A</i> axis of <i>b</i> *
	<i>Int 95%</i>	✓	95% confidence interval for intermediate <i>B</i> axis of <i>b</i> *
	<i>Min 95%</i>	✓	95% confidence interval for minimum <i>C</i> axis of <i>b</i> *
<i>R</i> *	<i>R Est</i>	✓	Section ellipse <i>R</i> estimate from <i>b</i> *
ϕ *	<i>Phi Est</i>	✓	Section ellipse ϕ estimate from <i>b</i> *
ΔR	<i>R Res</i>	✓	Residual between <i>R</i> * estimate and <i>R</i> data.
$\Delta \phi$	<i>Phi Res</i>	✓	Residual between ϕ * estimate and ϕ data.
Δd_H	<i>Dist Res</i>	✓	Hyperbolic distance residual between estimated and data sections.
	<i>X11, Y11</i>		First endpoint of first line of pair.
	<i>X12, Y12</i>		Second endpoint of first line of pair.
	<i>Alpha 1</i>	✓	Directed angle of first line clockwise from X axis.
	<i>X21, Y21</i>		First endpoint of second line of pair.
	<i>X22, Y22</i>		Second endpoint of second line of pair.
	<i>Alpha 2</i>	✓	Directed angle of second line clockwise from X axis.
	<i>Beta</i>	✓	Directed angle between two lines of pair.
<i>L_i</i>	<i>Li</i>		Initial line length.
<i>L_f</i>	<i>Lf</i>		Final line length.
α	<i>Alpha</i>		Final measured angle of line defined by <i>L_i</i> and <i>L_f</i> .

Table 1.1: Symbols and *column* headers. The column header is displayed in spreadsheet and data files. *Calc* indicates columns that are read only, calculated from other parameters.

2 Data Entry and Export

EllipseFit includes procedures for complete fabric and strain analyses, including image processing, digitizing, calculation of two-dimensional sectional ellipses, and combination of sections to obtain three-dimensional ellipsoids. Each data file represents a sample of particle measurements that define a fabric which can be analyzed in various ways. The fabric, if certain important assumptions are met, can be interpreted as a strain associated with tectonic deformation. The fabric, however, may also have formed due to primary sedimentary or igneous processes, or may be a combination of primary and tectonic fabrics. It can be difficult, or impossible, to factor out the effects of primary versus tectonic fabrics. The design and goals of the investigation will determine which of these is of interest, and what assumptions can be made about their relative effects on the fabric.

Data can be entered directly by digitizing images in EllipseFit, or by importing data from another application, such as ImageJ or MATLAB. Additionally, while EllipseFit includes options for image analysis, such as thresholding, it may be desirable to preprocess images in other software, such as Adobe Photoshop, GIMP, Adobe Illustrator, or Inkscape, such as when it is necessary to manually outline grains shapes for analysis using the *Filled Shape* routine covered in Section 2.2.7.

2.1 Data Files

EllipseFit files are saved in simple spreadsheet formats compatible with spreadsheet software such as Microsoft Excel and LibreOffice Calc. EllipseFit reads and writes a variety of formats, including comma separated (csv), tab separated (tsv or txt), LibreOffice Open Document (ods), and Excel (xlsx) formats. This allows keeping data in standard non-proprietary formats for archiving data sets. Tab separated value (tsv) files have a particularly simple text format, and can be opened in any text or word processing program, so are recommended for archiving. Comma separated value (csv) files are another simple option. Text format files (csv and tsv) use decimal point separators in numbers.

In addition to standard spreadsheet files, it is possible to export crystal size distribution (csd) files, a special format that is commonly used to analyze fabrics defined by crystals in igneous rocks, which can provide insight on igneous solidification processes. Using EllipseFit for data collection can provide a workflow that is more rapid than using, for example, first Photoshop or GIMP to outline images, and then ImageJ or MATLAB to calculate ellipses.

2.1.1 Spreadsheet Files

EllipseFit reads and writes a variety of formats, including comma separated (csv), tab separated (tsv or txt), LibreOffice OpenDocument (ods), and Excel (xlsx) formats. In addition to lines of data, each file must include a simple one line header, which indicates the type of data in each column. Angles are in degrees. Comments may be included to save metadata, such as collection localities, sample numbers, processing dates, and the names of investigators.

Note that some spreadsheet programs, including Microsoft Excel, lock open files so that other programs can not access them simultaneously. Close any such files before attempting to open them in EllipseFit. Table 1.1 lists the available file headers. The order of the headers, and data columns, does not matter. Unrecognized headers and columns are ignored, and are not saved internally. Lines beginning with a double slash, '//', are treated as comments. All initial comment lines, before the header line, are treated as metadata and can be edited and will be saved. Any additional comment lines, after the header or lines of data, are be ignored and will not be preserved if the input file is subsequently saved.

The required input parameters depend on the desired analysis, for example a basic Fry analysis (Section 3.1) requires only $[X, Y]$, however a normalized Fry analysis (Section 3.2) requires $[X, Y, R, Phi]$ or $[X, Y, Min, Max, Phi]$ parameters to be specified. Typical two-dimensional ellipse calculations also require $[X, Y, R, Phi]$ or $[X, Y, Min, Max, Phi]$ parameters, while three-dimensional ellipsoid calculations require section data to be input as $[R, Phi, Strike, Dip]$ or $[Max, Min, Phi, Strike, Dip]$ (Chapter 7). Section 2.1.2 gives example data files for various calculations.

Data may also be copied and pasted from spreadsheet files, or the EllipseFit data window. When copying from spreadsheets, make sure to include the header row so the data attributes can be correctly assigned.

2.1.2 Example Data Files

The included example files and images can be used to determine input data formats. The following are example files in the Ellipse folder for particle ellipse data, Fry-type, or mean ellipse calculations:

Ramsay and Huber 1983 F7-7.tsv
 Ramsay and Huber 1983 F7-7.jpg
 Ramsay and Huber 1983 F7-7 (large).jpg

These give an example of data digitized from a thin section photomicrograph (Ramsay and Huber, 1983). The $[X, Y]$ coordinates can be used for Fry-type analyses, or the $[X, Y, A, B, R, Phi]$ data for normalized Fry or mean ellipse analysis. Note that there are small and large versions, the large version (in the Points folder), which does not include a data file, may be used for teaching purposes.

For Wellman analysis (Vollmer, 2011b) from line angular shear data, the files:

Ragan 1985 F10-1a.tsv
 Ragan 1985 F10-1a.png

in the Lines folder contain example line angular shear data and an image (Ragan, 1985). Each data point requires the endpoints of two lines, $[X11, X12, X21, X22]$, that originally had a constant angle between them. This is an analytical solution to the classic multiple brachiopod problem illustrated in a number of structural geology texts. For strain analysis using line stretch data, the file:

Ramsay and Huber 1983 F6-8.csv

contains example line stretch data for lines with known initial and final lengths, such as boudins and folds. In this example, the data is from three stretched belemnites from the Swiss Alps (Ramsay and Huber, 1983, Figure 6.8).

For three-dimensional strain plots, the file:

Hossack 1968 A1.tsv

contains example ellipsoid data from deformed conglomerates in the Bygdin area of Norway (Hossack, 1968) with $[Max, Int, Min]$ axes data to demonstrate Flinn-Ramsay, and Hsu-Nadai plots (Section 7.1).

Data required for ellipsoid calculation from ellipse section data is given in the file:

Owens 1984 T1.tsv

This contains example ellipse section data measured from reduction spots in a sample of slate from Dinworwic, Wales, (Owens, 1984) for calculating a strain ellipsoid from three or more faces using the methods of Robin (2002) or Shan (2008). The strikes and dips of each section must be included, so the particle data must include $[Max, Min, Phi, Strike, Dip]$ (Section 7.3).

The folder Ellipsoid/Gunks contains four files with measurements from three near-perpendicular faces of a sample of Shawangunk Formation conglomerate, New York (Klemm et al., 2012, 2013). Three files are the measured section data ellipses, the fourth contains the section orientations, best-fit section ellipses, and the names of the three data files. These are used to demonstrate a typical three-dimensional strain ellipsoid analysis with confidence regions using the methods of Robin (2002) and

Shan (2008) (Section 7.4).

2.1.3 Crystal Size Distribution Files

The analysis of primary igneous fabrics can shed light on igneous solidification processes, but is complicated by the fact that section data includes cross sections through crystals of different forms. The topic has an extensive literature that is beyond the scope of this document, see Marsh (1988), Cashman and Marsh (1988), and Higgens (2000) for explanations of the theory and collection methodology for crystal size distribution (CSD) data.

EllipseFit does not attempt to duplicate the functions of existing CSD software, but offers a workflow that can improve the speed of data collection. Particle outlines can be directly traced as shapes (Sections 2.2.6 and 2.2.7) or quadrilaterals (Section 2.2.5), and the resulting moment ellipses output in a *csd* file compatible with *CSD Corrections* software using the *Export CSD* command. This workflow has been successfully used by Dr. K. Patwardhan in the SUNY New Paltz Igneous Petrology Laboratory, and continues to undergo refinement. Any additional input is appreciated.

2.2 Digitizing

Digitizing data from images is a crucial, if tedious, aspect of fabric and strain analysis. While there are numerous suggested techniques for automatic and semi-automatic extraction of fabric parameters from images (Section 8), it is generally recognized that in most cases a trained human eye is required to reliably digitize particle shapes. Image software including Photoshop, Illustrator, GIMP, and Inkscape are often used to outline particles by hand. The resulting images of particle outlines can then be imported to image analysis software, such as ImageJ or MATLAB to calculate equivalent ellipses, which are then used for fabric analysis. EllipseFit offers a simpler workflow, in that images can be opened, processed, digitized, and analyzed in one program.

Most of the digitizing methods support *rubberband* mode, where a line is drawn from the last point digitized to the current mouse location. This can be slow for some computers or high resolution images, so can be turned off in the *Preferences - Digitize* pane.

2.2.1 Coordinate System

In most cases it is satisfactory to digitize using the default coordinates, which are in pixels with the *X* axis to the right, and the *Y* axis down. This is chosen due to the common geologic convention of measuring strike and dip on a plane using the *right hand rule*. Using this convention, *X* is the right if the plane dips toward the observer, and lineations are measured as a pitch, ϕ , clockwise from the strike (Figure 7.7). Most fabric analysis methods do not use absolute sizes or areas, so are scale independent. If necessary, pixel data can be converted to absolute units at a later date provided the image and a scale are preserved. However, if necessary, absolute scaling can be done by one of two methods.

The easiest method is to select the units in the *Preferences* dialog *Digitize* pane, and then enter the scaling factor in pixels per inch or pixels per centimeter. Note that this is not the same as the image dpi (dots per inch) as reported in Photoshop or GIMP, which have no knowledge of the actual image scale. The scale needs to be calculated using an object of known physical size, such as a photographed scale bar or coin. This can be done using the mouse coordinates in pixels at both sides of an object of known dimensions.

A second method is to use a *Window*, with the known width and height of the image. If required, this can additionally include the *X, Y* coordinate of the image origin. Select *Preserve aspect* if the vertical and horizontal scales are equal, as is normally the case.

Although not recommended, it is possible to switch coordinate systems so that the *Y* axis is up, or the *X* axis is to the left. Normally, the *X* axis should be horizontal for three-dimensional analysis. However, it is possible to set the pitch of the *X* axis, its positive inclination in the section plane from horizontal. Modifications to the coordinate system can introduce user errors, so using the conventional

coordinates is recommended. Section 7.2 covers coordinate systems for three-dimensional fabric analysis.

2.2.2 Center Point

Digitizing particle centers is the most rapid method of data collection, although it limits the possible analyses. Select *Image - Digitize Image - Center Point* from the menu or toolbar, and sequentially select particle centers. This type of data entry allows various Fry-type analyses (Section 3.1), but not normalized Fry or mean ellipse calculations. Also, if the Fry analysis is to be used for irregular polygons (McNaught, 1994), digitizing as described in Sections 2.2.6 or 2.2.7 is required.

2.2.3 Ellipse Axes

This method provides rapid, four point, input of particles with well defined axes, however it is not generally recommended for most particles, as the quadrilateral, shape, and filled shape methods are more accurate. The *Image - Digitize Image - Ellipse Axes* command uses the first two points to define the radius and orientation of one ellipse axis, and the second two points to define the radius of the second axis (the orientation is not used). Shapes approximating a rectangle, general quadrilateral or triangle can more accurately be digitized using the quadrilateral method (Section 2.2.5). Shapes with more irregular outlines should be digitized with either the shape or filled shape methods (Sections 2.2.6 or 2.2.7).

2.2.4 5-Point Ellipse

This method provides rapid, five point, input of particles that closely approximate ellipses, such as ooids. However it is not generally recommended for most particles, as the shape and filled shape methods are more accurate. The *Image - Digitize Image - 5 Point Ellipse* command uses five points, the minimum required to define a general ellipse, to be digitized on the perimeter of a particle, which are then fit to an ellipse using a least-squares method. Particles with more irregular outlines should be digitized with either of the two shape methods (Sections 2.2.6 or 2.2.7).

2.2.5 Quadrilateral

Quadrilateral digitizing can be used for digitizing rectangles, rhombuses, or other quadrilaterals. Triangles may be digitized by selecting the three vertices and an additional point on one side. Points should be digitized in clockwise or counterclockwise order to form a closed, nonintersecting quadrilateral. This mode is useful when digitizing phenocrysts for crystal size distribution (CSD, Section 2.1.3) or strain analysis. The resulting moment ellipse will have the same area and moment axes as the quadrilateral. The result is identical to digitizing quadrilaterals as shapes, but requires digitizing only 4 points.

2.2.6 Shape

The *Image - Digitize Image - Shape* command provides the best method for digitizing most particles. A particle shape is approximated by a polygon using as many points as necessary, and closed by clicking on the first point. Points should be digitized in clockwise or counterclockwise order to form a closed, nonintersecting polygon, which may be concave. The polygonal shape is converted to an ellipse that has equivalent moments, referred to here as a *moment ellipse*, the moments include area, center of mass, and three inertia terms, which are calculated from the digitized shapes (Steger, 1996; Mulchrone and Choudhury, 2004).

Samples of moment ellipses can be shown mathematically to give equivalent results as elliptical particles, allowing irregular shapes to be used in place of ellipses (Mulchrone and Choudhury, 2004; Yamaji, 2013; Yamaji and Maeda, 2013). Additionally, as discussed in Section 3.2, this method extends the Fry method to irregular shapes. Note that this technique for calculating ellipses is *not*

a least squares best-fit, which will give inaccurate results for irregular particles (McNaught, 1994; Mulchrone and Choudhury, 2004). Also, a least squares ellipse requires a minimum of five points, while a moment ellipse requires only three.

2.2.7 Filled Shape

The *Image - Digitize Image - Filled Shape* command gives similar results as the *Image - Digitize Image - Shape* command, but differs in the method of calculation, using pixel summation for calculation of the moments. In this case an image of particle outlines is required, normally black outlines on a white background (Figure 2.1b). Clicking inside the outline uses a seed fill algorithm (Heckbert, 1990) to sum pixels as masses and calculate an ellipse with equivalent first and second moments (Steger, 1996), similar to procedures available in ImageJ and MATLAB. This is an excellent method for digitizing particles, but requires the additional step of outlining particles in an image editing program such as Adobe Photoshop or GIMP. The image *Diamictite Tracing.png*, a diamictite deformed below the Williard thrust, Antelope Island, Utah, is provided in the *Example Data/Shapes* folder (Figure 2.1b).

2.2.8 Line Pair

Digitizing line pairs is used for the Wellman method of strain analysis, where each particle, typically a fossil, has two identifiable lines that originally had a known angle between them that was subsequently modified by deformation. In this case select *Image - Digitize Image - Line Pair* and digitize each line pair in sequence. An example analysis is given in Section 5.1.

2.2.9 Line

Digitizing lines is mainly for apparent dip analysis, where planes intersect each of two or more exposure planes. These lines are the *traces* of planes on exposed surfaces. The trace of a plane is a line contained in the plane, and two or more of these can be used to define the plane. For this mode select *Image - Digitize Image - Line* and digitize each line in sequence. Details of an example analysis are given in Section 5.3.

2.2.10 Centered Ellipse

The centered ellipse method is only available on a Fry plot, and is used for manually fitting an ellipse through points around the edge of the elliptical void. As many points as desired can be digitized around the void, when done click on the start point, and a least-squares best-fit ellipse centered on the origin will be calculated. See Section 3.1 for an example application.

2.3 Graphics Export

Plots can be output to bitmap (raster) and vector graphics files (Table 2.1). Bitmap files are compatible with image editing programs such as Adobe Photoshop and GIMP, and can be imported into most word processing programs. Formats include Portable Networks Graphics (PNG), Windows Bitmap (BMP), Tagged Image File Format (TIFF or TIF) and Joint Photographic Experts Group (JPEG or JPG). The default format is a png file, a widely supported optimally compressed non-lossy format. bmp and tiff files are also non-lossy and widely supported. The jpg file format was designed mainly for photographic images, and is less suitable for plots and illustrations.

Vector graphics files allow editing in programs such as Adobe Illustrator, CorelDRAW, InkScape, and Computer Aided Design (CAD) programs such as AutoCAD and QCAD. Orient supports Scaled Vector Graphics (SVG), Portable Document Format (PDF), Encapsulated PostScript (EPS), and AutoCAD Drawing Exchange (DXF) formats. The SVG vector format is an open standard vector graphics format that is supported by most modern browsers and vector graphics editing software, including



(a)



(b)

Figure 2.1: Example of an image suitable for digitizing using the shape commands. The sample is a diamictite deformed below the Williard thrust, Antelope Island, Utah, see Yonkee et al. (2013) for geologic context. Note the presence of an inclined cleavage at the lower left. U.S. penny for scale. The images are in the Example Data/Shapes folder. Photograph by F.W. Vollmer. (a) Original image suitable for digitizing using the *Image - Digitize Image - Shape* command. (b) Tracing of particle outlines done in Photoshop, suitable for digitizing using the *Image - Digitize Image - Filled Shape* command.

Adobe Illustrator, Inkscape, and CorelDRAW. Opening a svg file in Firefox, for example will display the image, or identify any errors.

The vector graphics file formats vary in their support of drawing features. SVG is the most complete, including full support for transparency. SVG graphics can easily be rescaled in a vector graphics editing program. SVG can include bitmaps with transparency, such as color gradients. These will have a width and height in pixels as set in the *Page Size* dialog. Bitmaps in svg are compressed in png format and have an alpha channel to support transparency. SVG does not support layers, but grouped elements can be moved to layers once opened in a vector graphics editing program.

The PDF graphics implementation is almost as complete as SVG, however, transparency (alpha channel) is not supported for vector objects such as polygons. Vector objects with transparency will appear as a solid color, and will obscure any underlying objects. Transparency is, however, supported for bitmap images, such as gradients.

EPS is also a good choice for vector graphics, and can include bitmaps. Transparency is not supported for vector objects or bitmaps however. Bitmaps, such as multiple gradient fills, are flattened so multiple gradient layers will appear brighter, but they will not be transparent and will obscure underlying objects.

The DXF format supports layers, but not transparency. Only simple polygon fills are supported, and line styles, text, and colors may vary from other formats.

The svg files generated by EllipseFit conform to the World Wide Web Consortium (W3C) standard, however some, mostly older, versions of Adobe Illustrator contain bugs that prevent it from opening valid svg files. A work around is to open the svg file in another program, such as Inkscape, and save it in different format, such as pdf. Another option is to save the plot as a pdf or eps file which Illustrator should be able to open. Finally, try opening svg file in your browser, and save it as a pdf which should open in Adobe Illustrator in vector format.

Format	Extension	Format	Notes
Portable Network Graphics	png	Bitmap	Best for bitmap
Tagged Image File Format	tif or tiff	Bitmap	Good for bitmap
Windows Bitmap	bmp	Bitmap	Good for bitmap
Joint Photographic Experts Group	jpg or jpeg	Bitmap	Poor for line art, good for photos
Scaled Vector Graphics	svg	Vector	Best for vector graphics
Portable Document Format	pdf	Vector	Good, Adobe format, partial transparency
Encapsulated PostScript	eps	Vector	Good, Adobe format, no transparency
AutoCAD Drawing Exchange	dxf	Vector	Poor, but standard for CAD software

Table 2.1: Summary of supported graphics file output formats.

3 Point Distribution Analysis

It is common in nature for objects to be distributed relatively uniformly, but with a minimum cutoff distance between them. Such a distribution in space follows a truncated Poisson distribution (Fry, 1979; Davis, 1986; Waldron and Wallace, 2007; Shan and Xiao, 2011). This can be imagined by filling an empty fish tank by tossing in pingpong balls. As the centers of the pingpong balls can never touch, no object center can be closer to another object center than twice the radius of a balls, giving a cutoff distance of twice the radius.

The basic idea, simplified for two dimensions (Ramsay and Huber, 1983), is that the minimum distance between the object centers is initially the same in all directions. If each data point is sequentially translated to the origin, and the distances and directions to all other points are plotted, they define a cloud with a circular void defined by the minimum distances between object centers. After a homogeneous deformation, the particle centers are closer in some directions and further in others, so the post-strain point distribution defines an elliptical void. This void is referred to here as the *central void*.

Examples of this type of data include the centers of clasts in sedimentary rocks such as sandstones and conglomerates. The centers of phenocrysts in igneous rocks, where nucleation of crystals is prevented in proximity to existing crystals due to the chemical gradient, is another example. Two dimensional examples include the centers of skolithos burrows and dewatering structures.

If the viscosity of the particles is identical to the viscosity of the enclosing matrix, point distribution methods should give similar results to mean ellipse methods (Section 6.5). If the particles have a different viscosity, or are even perfectly rigid, it may be possible to determine the *strain partitioning* between the rock and the inclosed particles using both point distribution and ellipse fitting methods.

Two general point distribution methods have been proposed, a nearest neighbors approach (Ramsay, 1967; Ramsay and Huber, 1983), and an all object separation approach (Fry, 1979), commonly referred to as the Fry method. The latter, initially graphical, approach has many variations, one of the most common is the *normalized Fry method* (Erslev, 1988; Erslev and Ge, 1990). It is important to note that the normalized Fry method requires the particle shape, and therefore loses complete independence from mean ellipse methods.

The nearest neighbors approach (Section 3.3.2) has been enabled computationally by the availability of *Delaunay triangulation* algorithms (Preparata and Shamos, 1985; Vollmer, 1998; Mulchrone, 2002, 2013), an approach used in *EllipseFit 1* (Vollmer, 1998). The primary advantage of using Delaunay triangulation is that it decreases the number of points required to be examined, reducing computational time. However, there is a tradeoff in statistical confidence. As most calculations in *EllipseFit* are fast, reducing the number of points examined using Delaunay triangulation should not be necessary. It is therefore an option, which may be used if desired (Section 3.3.2), an alternative option is to reduce the number of points to by specifying a *clip radius*.

A critical problem in point distribution analysis is to determine the fabric ellipse from the central void. The enhanced normalized Fry method (Erslev and Ge, 1990) was developed to solve this, but requires the particle ellipses, blurring the distinction between point and ellipse methods. Numerous solutions to the void fitting problem have been proposed, Section 3.3 discusses some of these methods with additional variations.

3.1 Fry Analysis

Fry analysis (Fry, 1979) is a widely used technique for analyzing point distribution data, and there is an extensive literature on it and its variations (Hanna and Fry, 1979; Crespi, 1986; Onasch, 1986; Erslev, 1988; Erslev and Ge, 1990; Dunne et al., 1990; McNaught, 1994, 2002; Shan and Xiao, 2011; Waldron and Wallace, 2007; Mulchrone, 2013).

A Fry analysis can be simply done with two pieces of tracing paper, first tracing all of the particle centers on one sheet, then drawing an origin point in the center of a second sheet overlain on the first. The origin is moved sequentially to each particle center point in turn, and all the other center points

are traced in. For n initial points, this generates:

$$n_f = n(n - 1) \quad (3.1)$$

To illustrate the use of the method open the image file (*File - Open Image*) Ramsay and Huber 1983 F7-7 (large).jpg. This is a photograph of a deformed ironstone oolite in thin section from Ramsay and Huber (1983) that is widely used as a test image for strain analysis. For point digitizing select *Image - Center Point*, and *Image - Add Tool*, as indicated by the toolbar icons in Figure 3.1a.



Figure 3.1: Example set up for a Fry analysis. Both *Image - Center Point* (red dot), and *Image - Add Tool* (green plus sign) must be selected. At this stage only one point has been digitized. (a) The *Image* window with the file Ramsay and Huber 1983 F7-7 (large).jpg open. (b) The initial Fry plot with a single point at the center.

Use the *Zoom In* tool to enlarge the image, and click on one particle center. The *Data* window will display a highlighted line of data. Before continuing, open the Fry plot (*Plot - Fry Plot*), as shown in Figure 3.1b. The plot will have a single point in the center.

Continue digitizing point centers, ideally working out from one point digitizing adjacent points and keeping a roughly circular area. The Fry plot will start to develop, with each new set of generated points highlighted (Figure 3.2b). If the plot is too zoomed in or out, make sure that *Auto-scale* is set on in the *Preferences* dialog *Fry Plot* pane. After digitizing about 20 points and establishing the size of the central void, the plot can be scaled by unchecking *Auto-scale*, and entering an appropriate value for the plot radius.

Use the *Hand Tool* to scroll, and the *Zoom Tool* to zoom. The *Command* (Mac) or *Control* (Windows and Linux) *Plus* and *Minus* keys are used to zoom in and out. Holding down the *Shift* key allows scrolling with the mouse. Points can be deleted by using the *Find Tool* to highlight a point, and delete it using the *Cut* command. A point can also be deleted by selecting it in the *Data* window and deleting it there. It is important to be objective, and it may be best to digitize all available points, however some particles may not meet the required assumptions. Also, note that the centers of the particles in two-dimensions do not generally correspond to their three-dimensional centers, as they lie on an arbitrary plane cutting through the rock, so the assumption of a uniform cutoff distance is weakened.

It is desirable to select approximately equal numbers of particles in all directions, so the point density is not biased by direction. This is one reason to maintain a uniform point density in a circular area while digitizing, and why having the interactive Fry plot open can assist in particle selection, this is discussed further in Section 3.1. To change the size of the digitized point symbols, open the *Preferences* dialog, where most of the preferences can be changed. The effect of changes can be previewed with the *Preview* button before committing to them with the *OK* button. The *Void fit options* should be left unchecked during digitizing, this is used for automated void fitting discussed in Section 3.3.

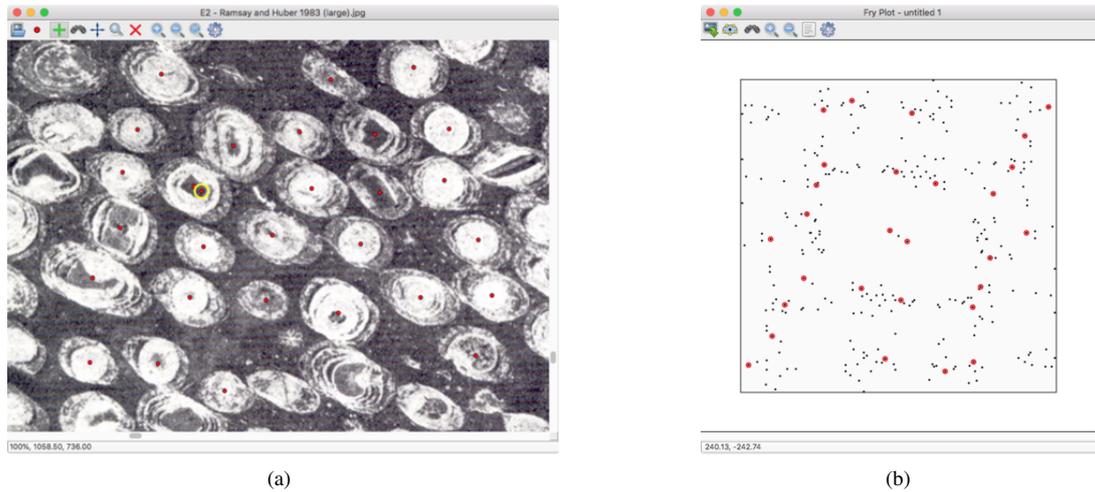


Figure 3.2: Example Fry analysis after digitizing 30 adjacent particle centers. (a) The *Image* window zoomed in. Each digitized particle center is indicated by a red dot, the dot circled in yellow is the currently selected particle center. (b) The Fry plot. The circled points are Fry points generated by the currently selected particle center. Note the presence of two points near the plot center, this indicates a spurious data point, in this case caused by digitizing a particle center twice. Since it is now selected, the *Edit - Cut* command can be used to delete it.

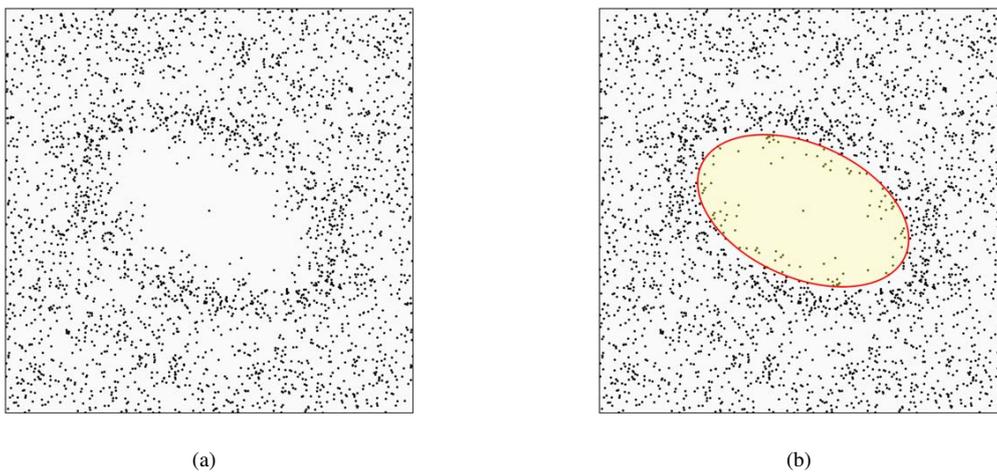


Figure 3.3: (a) Example Fry plot after digitizing all ooid centers. (b) Plot after fitting an ellipse to the central void.

Figure 3.3a shows the zoomed in central void after digitizing essentially all of the particle centers. The next step is to determine the best-fit ellipse for the central void. This can be a subjective process, and objectively choosing this ellipse is the subject of many papers (Erslev and Ge, 1990; Waldron and Wallace, 2007; Shan and Xiao, 2011; Mulchrone, 2013; Kumar et al., 2014). For the purposes of this section, it will be assumed that the void has been defined well enough to pick out the void by eye, which can be a good enough estimate, and also makes a good exercise for student laboratories. Click on the *Centered Ellipse* icon, and click at the edge of the void. An orange circle marks the starting point, subsequent points are marked by a yellow circle. When finished, click on the orange circle and the ellipse will be calculated and displayed in the *Log* window:

Void Fit Results

Ramsay and Huber 1983 F7-7

2020-06-14 17:30:59

```
=====
n           : 252
nf          : 31626 pairs
Time       : 00:00:00
Digitized
  Normalized      : False
  Delaunay       : False
Best-Fit Ellipse
  nfe            = 17
  a              = 26.996
  b              = 15.536
  R              = 1.738
  φ              = 25.79°
  RMS            = 0.1147
  SSE            = 0.2237
```

A centered ellipse was calculated from the 17 digitized points, n_{fe} . The calculation is rotationally invariant, and the best fit found by minimizing the sum of the squares of the distance of the points from the ellipse, the residuals. The minimization is solved from the linear equations using a LU decomposition.

The RMS (root mean square) is the square root of the average of the squared residuals of the data from the fitted ellipse. RMS is a common way to express goodness of fit of least squares solutions, and will be 0 for a perfect fit. It is not a measure of the error in the strain calculation, but a measure of how closely the digitized points fit the ellipse. A small RMS means that the entered points lie close to an ellipse.

Finally the calculated strain can be removed from the image and data, be sure to save a copy of your data before this step! First use the *Image - Transform Image* command and enter the results into the dialog as in Figure 3.4a. Next select the *Data - Transform Data* command and enter the calculated values as shown in Figure 3.4b. Press *Transform* and then *Accept*. The data is unstrained using the calculated values, as shown by the Fry plot in Figure 3.5a. The *Rectify* option resolves the offsets caused by the image transformation, so the data points remain centered over the particle centers (Figure 3.5b). Note that image must be transformed first for rectify to work, as the required translation is calculated during image transformation.

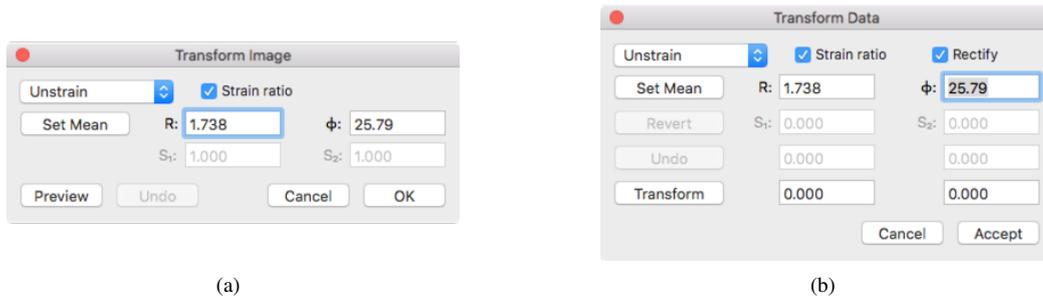


Figure 3.4: (a) The *Transform Image* dialog with values entered to unstrain the image. (b) The *Transform Data* dialog with values entered to unstrain (retrodeform) the data. *Set Mean* is only used if ellipse data is available. *Rectify* resolves the offsets caused by the image transformation, the image must be transformed for *Rectify* to work.

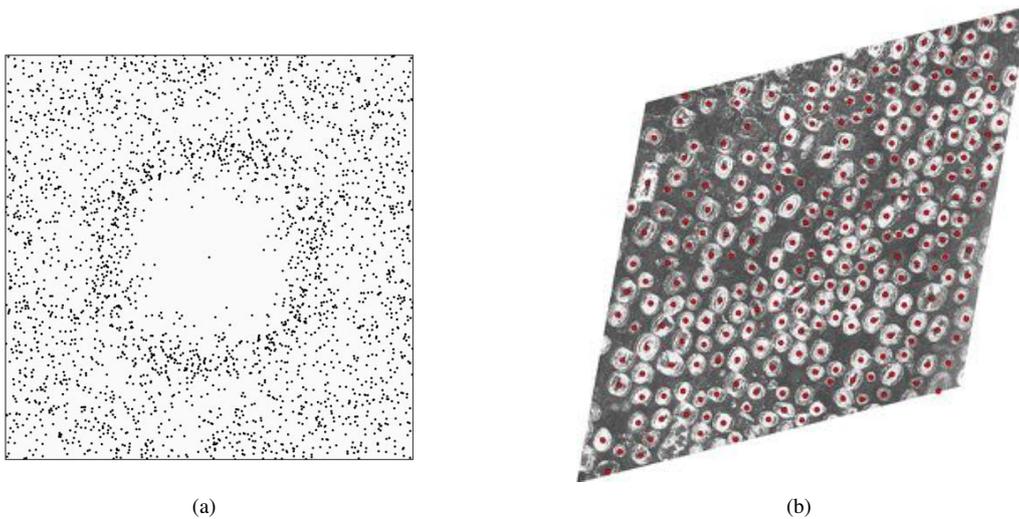


Figure 3.5: (a) Fry plot of the retrodeformed center point data after using the *Transform Data* command to unstrain (retrodeform) the data using the calculated values. (b) Unstrained (retrodeformed) image with superimposed ellipse data, formed by using the *Transform Image* command, followed by the *Transform Data* command with the *Rectify* option.

3.2 Normalization

As noted in Section 3, the Fry analysis is a two-dimensional solution to a three-dimensional problem, since initial particles are assumed circular instead of spherical. Even if the particles have a uniform size, a section through a sample will show them as different size particles. One solution developed to overcome this is the *normalized* Fry analysis (Erslev, 1988; Erslev and Ge, 1990).

The distances between particles are normalized to account for the difference in the sizes of the particles, which can greatly improve the sharpness of the central void. However, the ellipse sizes and orientations are required for this, so the particle ellipses must be digitized as discussed in Sections 2.2.3 to 2.2.7. A disadvantage of normalization is that it blurs the distinction between particle center and particle shape methods, which may be undesirable, especially for strain partitioning studies. For an example of this type of analysis, open the image file:

Ramsay and Huber 1983 F7-7.jpg

and the data file:

Ramsay and Huber 1983 F7-7.tsv

and open a Fry plot. The data is overlain on the image (Figure 3.6), and, if the *Find Tool* icon is selected, individual selected particles will be highlighted in the *Data* window, the *Image* window, and the *Fry Plot*. This selection method is implemented for most of the plots discussed in subsequent chapters. To zoom in on the central void, open the *Preferences* dialog, and in the *Fry Plot* pane, deselect *Auto-scale*, and enter 50 (pixels) for the *Plot radius*. The resulting Fry plot will look like Figure 3.7a.

To normalize the plot, select *Normalize* in the *Fry Plot* pane, and enter 1.3 for the *Norm radius*. The plot has been normalized to a unit radius, so is no longer scaled in pixels. The resulting plot will look like Figure 3.7b. Note the clear sharpening of the central void. Normalizing can be done for the enhanced normalized, exponential edge detection, Delaunay neighbors, and density gradient methods described in Section 3.3, providing object shapes, $[a_i, b_i, \phi_i]$, are available.

McNaught (1994) showed that fitting *least-squares ellipses* to particle shape outlines (polygons) for the normalized Fry method caused errors with non-elliptical particles, and suggested that the area and polygon center of mass (centroid) should be used instead. If the ellipse data is collected using the digitizing method recommended here, using *moment ellipses* (Steger, 1996), the polygon centroids and areas are maintained, and this problem is avoided.

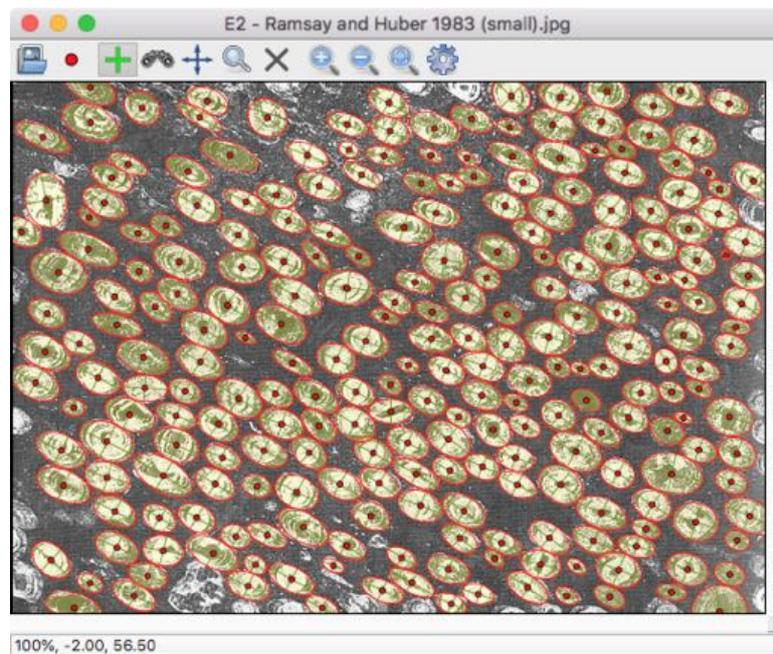


Figure 3.6: The *Image* window with image file Ramsay and Huber 1983 F7-7.jpg, and data file Ramsay and Huber 1983 F7-7.tsv open. Each particle is shown with its digitized center, and ellipse with ellipse axes. The size of the center point symbol has been reduced to 4 points in the *Preferences* dialog *Digitizing - Symbols* pane.

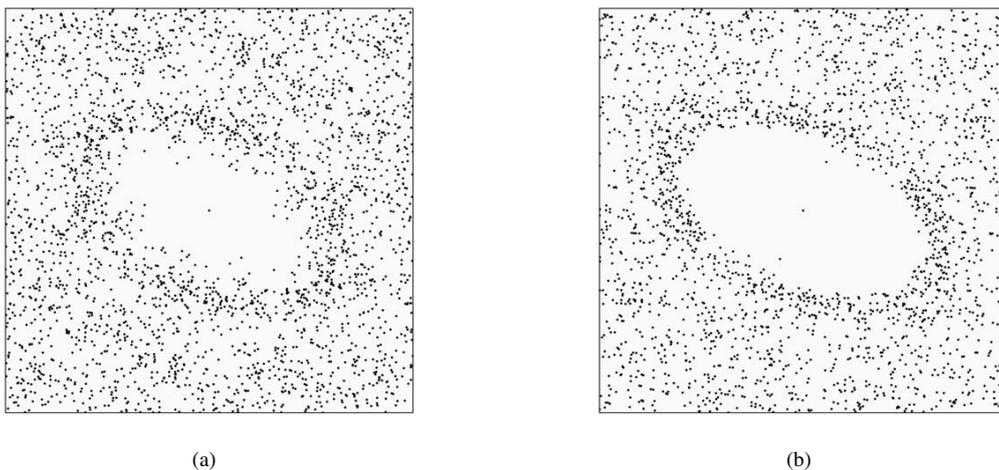


Figure 3.7: Fry plots of the Ramsay and Huber 1983 F7-7 data. (a) Fry plot without normalizing. The plot radius has been set to 50 (pixels) in the *Preferences Fry Plot* pane. (b) Normalized Fry plot, note the clear sharpening of the central void. As the plot is normalized to a unit circle, the *Norm radius* is used, here it is set to 1.3.

3.3 Objective Void Fitting

Calculating the strain from a sample of points should ideally be objective, not requiring a user to subjectively determine the best-fit ellipse, and, ideally, should not require additional information about particle shape. An objective numerical calculation is therefore desirable, and a number of methods have been proposed (Erslev and Ge, 1990; McNaught, 1994; Mulchrone, 2002, 2013; Waldron and Wallace, 2007; Lisle, 2010; Shan and Xiao, 2011; Reddy Vinta and Srivastava, 2012; Kumar et al., 2014). Methods currently implemented are accessed using the *Fit Void* command and then selected from the *Fit Void* dialog.

Kumar et al. (2014) tested six such methods, including the Delaunay triangulation nearest neighbors (DTNN), density contrast (point-count), exponential edge detection (EED, renamed here from continuous function, with approval of J. Waldron), and mean log likelihood methods, using two-dimensional simulated data sets, and concluded that of those six, exponential edge detection (Waldron and Wallace, 2007) is the most accurate, followed by the DTNN method (Mulchrone, 2013).

The enhanced, enhanced normalized (Erslev, 1988; Erslev and Ge, 1990) and related Delaunay nearest neighbors (Mulchrone, 2002) methods require particle shape information, $[a_i, b_i, \phi_i]$, ellipse radii and orientations, they differ in that the enhanced method uses the entire point cloud, that is, all object to object distances, while Delaunay methods use only the nearest neighbors distances (Ramsay and Huber, 1983).

The exponential edge detection, density contrast, and mean log likelihood methods do not require shape information. This gives them an advantage in terms of the speed of data collection, and where shape information is not available, such as in the spacing of dewatering pipes (Waldron and Wallace, 2007). Additionally, the analysis is entirely independent of particle shape, so may be used to complement ellipse based methods in strain partition studies.

Kumar et al. (2014) concluded that the exponential edge detection (EED) method was more accurate than the density contrast method, and that the DTNN, density contrast, exponential edge detection, and image analysis methods are least affected by the degree of sorting, the nature of distortion or the amount of distortion. The mean log likelihood method (Shan and Xiao, 2011), gave less accurate results, possibly because the non-random point distribution in their simulated samples violated the method's requirement of a homogeneous truncated Poisson distribution.

Void fitting methods that are not computationally intensive are suitable for bootstrap error analysis and calculation of confidence intervals. See Section 3.3.7 for a discussion of error analysis and the bootstrap methodology, and Section 3.3.8 for a relative comparison of the methods.

3.3.1 Enhanced

The enhanced Fry method (Erslev and Ge, 1990) uses a specified cutoff radius to exclude particles beyond a certain distance from the void center. This requires particle shape data, $[a_i, b_i, \phi_i]$, so can not be independently applied to particle center data. The cutoff radius is set by the selection factor, s_f , which has a default value of $s_f = 1.2$. A value between about 1.1 and 1.3 is recommended to minimize error (Mulchrone, 2002).

Using the data file Ramsay and Huber 1983 F7-7.tsv, in the *Void Fit* dialog select the *Enhanced* pane, and set *Enhanced* on, with a *Selection factor* of 1.2 (Figure 3.8). Additionally, check *Bootstrap* with 1000 resamples, this does an error analysis by resampling the data set with replacement (Section 3.3.7). As this uses random resampling, the resulting confidence intervals will vary slightly each time. Press *Preview*, and then *Run*. The best-fit ellipse through the cloud of points is calculated using a rotationally invariant least squares method. The resulting plot is shown in Figure 3.9a, and the following results are written to the *Log* window:

```
Void Fit Results
Ramsay and Huber 1983 F7-7
2020-06-28 18:47:55
```

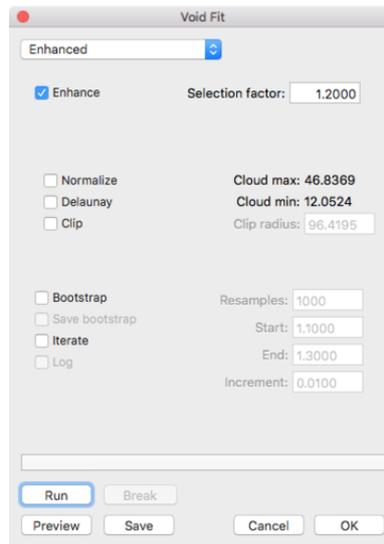


Figure 3.8: The *Void Fit* dialog displaying the *Enhanced* pane. The *Enhance* option is selected, and the *Selection factor*, s_f , is set to the default 1.2. The resulting plot after selecting *Run* is shown in Figure fig:point.obj.enhanceda.

```

=====
n          : 252
nf         : 31626 pairs
Time      : 00:00:15
Enhanced
  Normalized      : False
  Delaunay       : False
  Clip radius     : False
  Selection factor : 1.200
  Enhanced pairs  : 306
Best-Fit Ellipse
  nfe           = 306 pairs
  a             = 35.023
  b             = 21.071
  R             = 1.662
   $\phi$          = 25.83°
  RMS           = 0.2889
  SSE           = 51.0970
Bootstrap Confidence
  nr           = 1000 resamples
  R            = 1.662
   $\phi$          = 25.83°
  R 95%       = 0.142
   $\phi$  95%     = 2.78°
  dH 95%      = 5.77°

```

RMS (root mean square) is a measure of the deviations of the residuals, and can be used to refine the selection factor. However, note that smaller number of points will generally have a smaller RMS, so finding the minimum RMS is not a valid strategy. The error analysis gives estimated 95% confidence intervals for R , ϕ , and d_H . d_H is the hyperbolic distance, a single number reflecting the combined errors in R and ϕ (Sections 3.3.7 and 6.2.3). Note that, due to the random sampling, the error estimates will vary a small amount for each run.

Selecting the *Normalize* option (Figure 3.8) results in the plot shown in Figure 3.9b, and the fol-

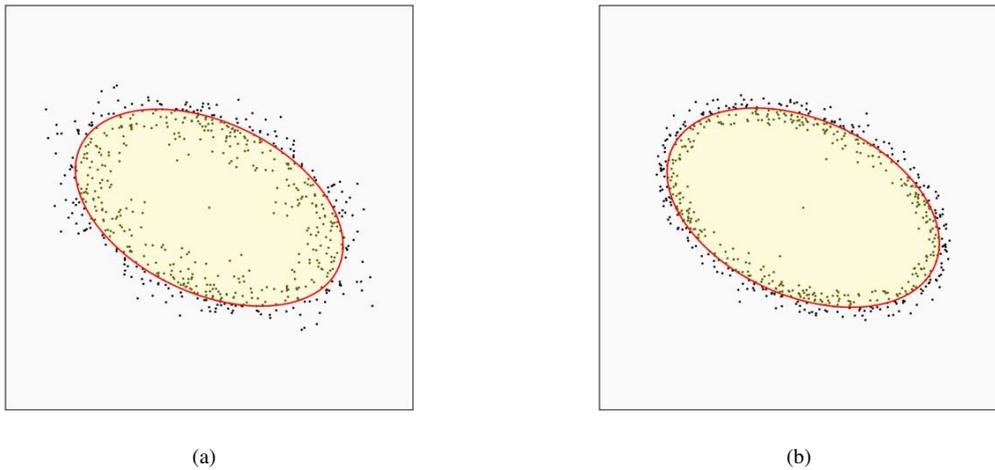


Figure 3.9: Fry plots of the data in file Ramsay and Huber 1983 F7-7. The *Selection factor* is set to 1.2. (a) Plot using the *Enhanced* method. The *Plot radius* is 50. (b) Plot using the *Enhanced* method with the *Normalized* option. The *Norm radius* is 1.3.

Following results are displayed in the *Log* window:

Void Fit Results

Ramsay and Huber 1983 F7-7

2020-06-16 16:38:28

=====

```
n          : 252
nf         : 31626 pairs
Time      : 00:00:16
Enhanced
  Normalized      : True
  Delaunay       : False
  Clip radius    : False
  Selection factor : 1.200
  Enhanced pairs  : 306
```

Best-Fit Ellipse

```
nfe      = 306 pairs
a        = 0.919
b        = 0.566
R        = 1.622
φ        = 24.43°
RMS      = 0.1582
SSE      = 15.3226
```

Bootstrap Confidence

```
nr       = 1000 resamples
R        = 1.622
φ        = 24.43°
R 95%   = 0.053
φ 95%   = 2.69°
dH 95%  = 3.23°
```

This gives results close to the enhanced analysis, with smaller confidence intervals. The bootstrap resamples can be saved and plotted for a graphical representation of the error. Figure 3.10 are plots

of the resample means used to determine the confidence intervals for the enhanced method, and Figure 3.11 for the enhanced normalized method. The bootstrap samples have been rotated (unstrained) to the mean. The smaller scatter in the normalized bootstrap means is reflected in the smaller 95% confidence intervals.

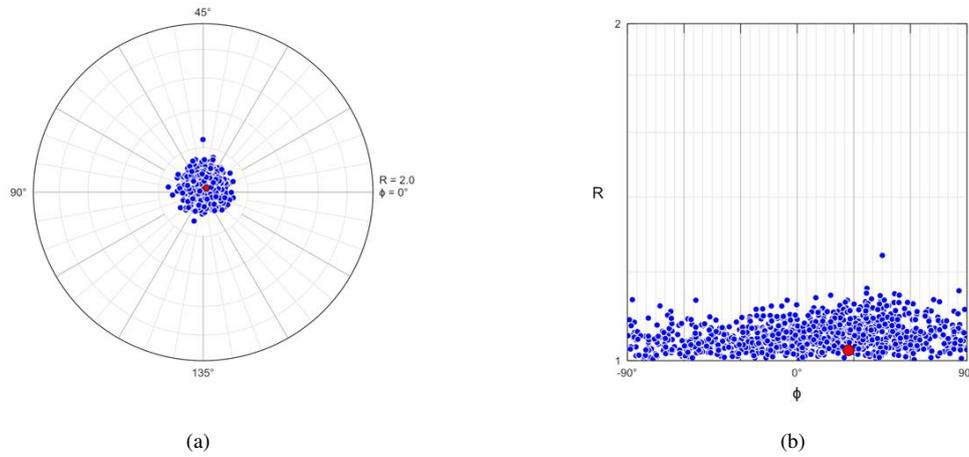


Figure 3.10: Fabric plots of the resample means of 1000 bootstrapped resamples used for determining the confidence intervals for the enhanced method. The resample means are rotated to the sample mean (undeformed), the red circle is the mean of the resample means. The low scatter in the plots reflects the confidence in the result. (a) Elliott (equidistant) polar plot. (b) $\ln R_f / \phi$ plot.

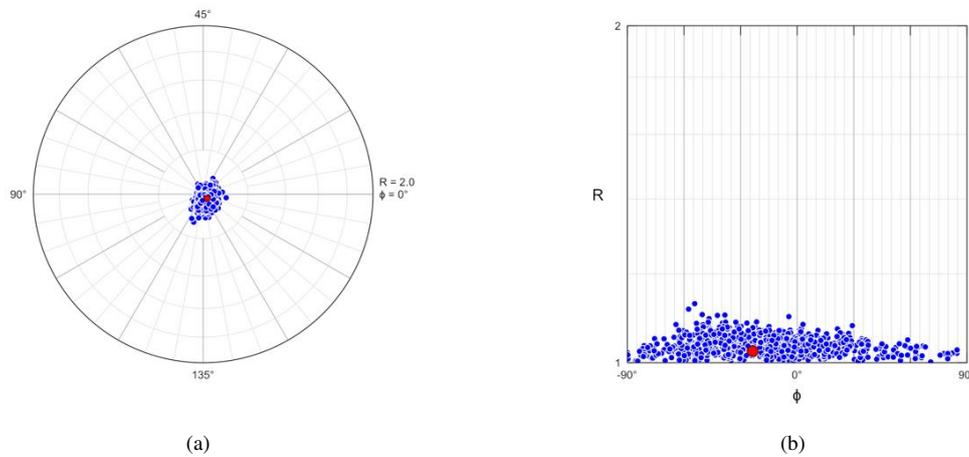


Figure 3.11: Fabric plots of the resample means of 1000 bootstrapped resamples used for the confidence intervals using the enhanced method with the normalized option. The resample means are rotated to the sample mean (undeformed), the red circle is the mean of the resample means. The low scatter in the plots reflects the confidence in the result. (a) Elliott (equidistant) fabric plot (Section 6.3.1). (b) $\ln R_f / \phi$ plot.

An additional option to aid in evaluating the effect of the value of s_f is given by the *Iterate* and *Log* options. If selected, the value of s_f is iterated by an increment, and the associated mean and confidence calculated. By default, the iteration steps through values from 1.1 to 1.3 by an increment of 0.1.

3.3.2 Delaunay Neighbors

A Fry plot contains information about the distances between all data points. An alternative methodology is to use only the nearest neighbors (Ramsay, 1967; Ramsay and Huber, 1983; Vollmer, 1998;

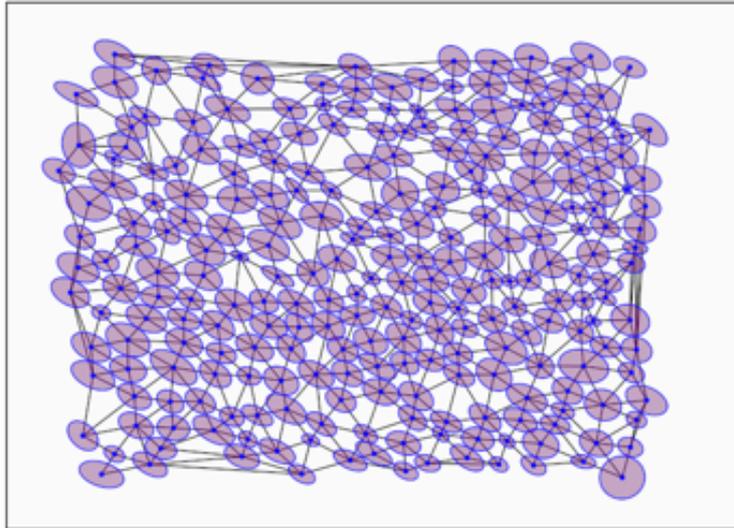


Figure 3.12: Strain map of the Ramsay and Huber 1983 F7-7 data with Delaunay triangulation excluding the bounding hull. The triangle edges are the nearest neighbor distances.

Mulchrone, 2002, 2013). A Delaunay triangulation is a triangulation of points in a plane such that no point is inside the circumcircle of any triangle, the edges of the triangles therefore define the nearest neighbor distances (Figure 3.12). There can be edge effects related to the shape of the sampled area, discarding the bounding hull helps to minimize this. Additionally, particularly at higher strains, the nearest neighbors are not guaranteed to be the same as the nearest neighbors prior to deformation. However, this subset of points can provide a less computationally intensive set for function or search minimization procedures.

The use of Delaunay nearest neighbors is an *option* in the enhanced, exponential edge detection, density contrast, and weighted least-squares methods. In each case the point cloud is reduced to the nearest neighbors using the edges of a Delaunay triangulation, reducing the number of required calculations in a search or function minimization. The methods described in this section are the enhanced Delaunay, and the enhanced normalized Delaunay methods, the latter follows the Delaunay triangulation nearest neighbors (DTNN) method of Mulchrone (2002). As these are based on the enhanced method (Section 3.3.1), they require shape data, $[a_i, b_i, \phi_i]$. Figure 3.13 compares a standard Fry plot to one using only Delaunay neighbors. The plots are zoomed out to illustrate the reduction in points. The “wings” are due to the rectangular shape of the digitized area.

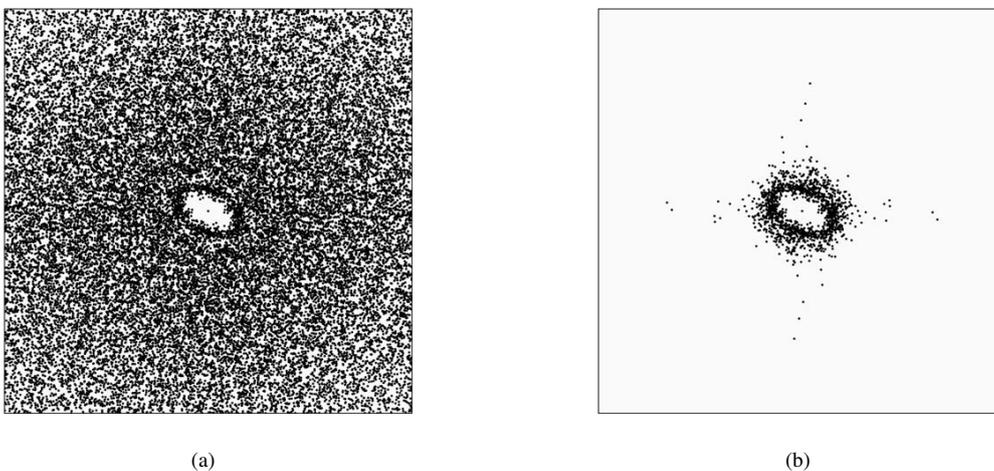


Figure 3.13: Fry plots of the data in file Ramsay and Huber 1983 F7-7. The *Selection factor* is set to 1.2. (a) Standard Fry plot with no additional options. The *Plot radius* is 200. (b) Plot using the *Delaunay* option. The *Norm radius* is 5.2.

Figure 3.8 shows the *Void Fit* dialog *Enhanced* pane. For an enhanced Delaunay plot, select *Enhanced* and *Delaunay*, and deselect *Normalize*. Additionally, select the *Bootstrap* option with 1000 resamples. The resulting plot is shown in Figure 3.14, and the log output is:

Void Fit Results

Ramsay and Huber 1983 F7-7

2020-06-16 15:20:23

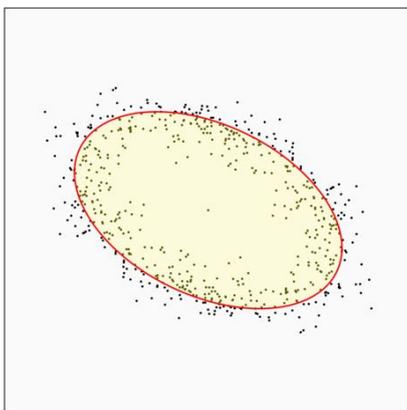
```
=====
n           : 252
nf          : 717 pairs
Time       : 00:00:00
Enhanced
  Normalized      : False
  Delaunay       : True
  Clip radius    : False
  Selection factor : 1.200
  Enhanced pairs : 305
```

Best-Fit Ellipse

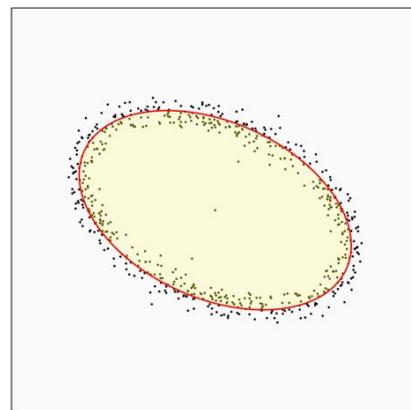
```
nfe      = 305 pairs
a        = 35.006
b        = 21.073
R        = 1.661
 $\phi$     = 25.85°
RMS     = 0.2894
SSE     = 51.0834
```

Bootstrap Confidence

```
nr       = 1000 resamples
R        = 1.661
 $\phi$     = 25.85°
R 95%   = 1.861
 $\phi$  95 % = 10.95°
dH 95%  = 47.13°
```



(a)



(b)

Figure 3.14: Fry plots of the data in file Ramsay and Huber 1983 F7-7. The *Selection factor* is set to 1.2. (a) Plot using the *Enhanced* method with the *Delaunay* option. The *Plot radius* is 50. (b) Plot using the *Enhanced* method with the *Delaunay* and *Normalized* options. The *Norm radius* is 1.3.

Comparing the results to the enhanced method (Section 3.3.1), the enhanced Delaunay option gives similar results, $[R, \phi] = [1.661, 25.85^\circ]$ as opposed to $[1.662, 25.83^\circ]$, however, 95% confidence regions are very large. Figure 3.15 shows fabric plots of 1000 bootstrap resamples illustrating the large amount of scatter that is reflected in the large confidence regions. Compare these plots to Figure 3.10, which are the bootstrap results of the enhanced method without using the Delaunay option.

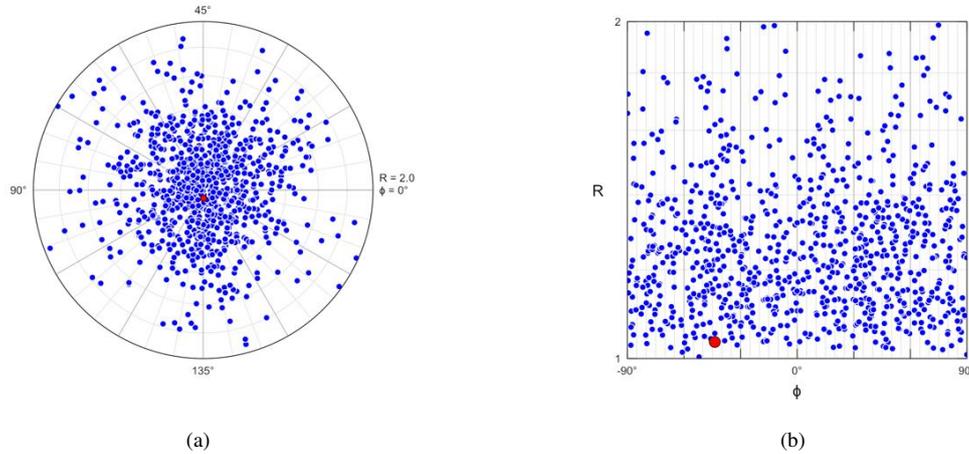


Figure 3.15: Fabric plots of the resample means of 1000 bootstrapped resamples used for determining the confidence intervals for the enhanced Delaunay method. The resample means are rotated (undeformed) to the sample mean, the red circle is the mean of the resample means. The large amount of scatter in the plots compared to Figure 3.10 reflects the decreased confidence in the result. (a) Elliott (equidistant) polar plot. (b) $\ln R_f / \phi$ plot.

A similar calculation can be done for the enhanced normalized Delaunay method, giving:

Void Fit Results

Ramsay and Huber 1983 F7-7

2020-06-18 12:34:37

=====

```
n          : 252
nf         : 717 pairs
Time       : 00:00:00
Enhanced
  Normalized      : True
  Delaunay       : True
  Clip radius    : False
  Selection factor : 1.200
  Enhanced pairs : 305
```

Best-Fit Ellipse

```
nfe      = 305 pairs
a        = 0.918
b        = 0.566
R        = 1.621
phi      = 24.45 degrees
RMS      = 0.1584
SSE      = 15.3037
```

Mean and Bootstrap Confidence

```
nr       = 1000 resamples
R        = 1.621
phi      = 24.45 degrees
```

R 95% = 0.621
 ϕ 95% = 24.45°
dH 95% = 27.69°

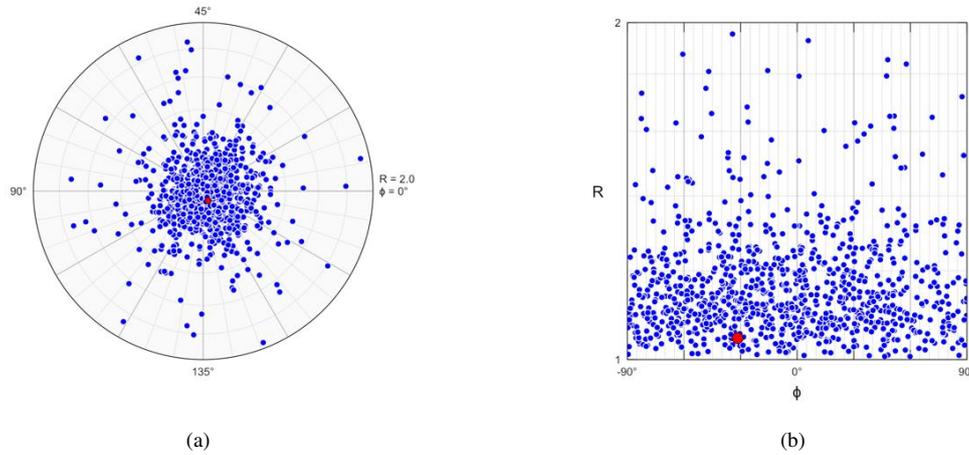


Figure 3.16: Fabric plots of the resample means of 1000 bootstrapped resamples used for the determining confidence intervals for the enhanced normalized Delaunay method. The resample means are rotated (undeformed) to the sample mean, the red circle is the mean of the resample means. The large amount of scatter in the plots compared to Figure 3.11 reflects the decreased confidence in the result. (a) Equal-area fabric plot (Section 6.3.1). (b) $\ln R_f / \phi$ plot.

Comparing the results to the enhanced normalized method (Section 3.3.1), the results are similar, but again with very large 95% confidence regions. Figure 3.16 shows fabric plots of 1000 bootstrap resamples illustrating the large amount of scatter that is reflected in the large confidence regions. Compare these plots to Figure 3.11, which are the bootstrap results of the enhanced normalized method without the Delaunay option.

Due to the much reduced Fry cloud size, the enhanced Delaunay method is faster than the enhanced method. This is most critical when calculating confidence intervals using bootstrap statistics, however, for 1000 resamples on a modern laptop, this is a savings of only a few seconds for a significant loss in confidence.

3.3.3 Density Contrast

Waldron and Wallace (2007) suggest a point counting method that does not require any information about particle shape. This gives an advantage in terms of the speed of data collection, and where shape information is not available, such as in their example of the spacing of dewatering pipes. Additionally, the analysis is entirely independent of particle shape, so may be used to complement shape-based methods. The plot can, however, be normalized if object shape data, $[a_i, b_i, \phi_i]$, are available.

The method uses two annular ellipses with the same aspect ratio. The search parameters are the minimum radius of the inner void fit ellipse, b , its aspect ratio, R , and orientation, ϕ , which are varied to maximize the density contrast, C . Waldron and Wallace (2007) vary the maximum radius of the inner void fit ellipse, a , instead of b , however it is simpler to select a default value for b , and the computation is otherwise identical. The default value for search parameter, $K = \sqrt{2}$, gives equal areas to the inner ellipse and the search annulus, as suggested by Waldron and Wallace (2007), and affirmed by Kumar et al. (2014).

The *Density contrast* dialog pane is shown in Figure 3.17. Options include minimum, maximum, and increments of the three search parameters. These can be automatically set to default values by pressing the *Set* button, or can be entered manually. The automatic parameter search settings are determined by finding the minimum Fry cloud radius, r_{fmin} , and the maximum cloud radius,

r_{fmax} , which depend on the *Clip*, *Normalize*, and *Delaunay* settings. The default search ranges and increments for the void ellipse minimum radius, b , void ellipse ratio, R , and void ellipse orientation, ϕ , are:

$$\begin{aligned} b &= [r_{min} \cdots 2r_{fmin}], \quad r_{fmin}/100 \\ R &= [1.0 \cdots 3.0], \quad 0.1 \\ \phi &= [0.0^\circ \cdots 179.9^\circ], \quad 0.1^\circ \end{aligned} \quad (3.2)$$

The clip radius is set to $8r_{fmin}$, but can be decreased to speed up the search. These defaults generally work well, but may need to be modified for specific data sets.

Figure 3.18a shows a preview of automatically selected density contrast options. The two inner blue rings represent the minimum and maximum search values for the minimum (short) void fit ellipse radius, b . The outer yellow circle is the maximum search radius. Figure 3.18b shows the best solution:

Void Fit Results

Ramsay and Huber 1983 F7-7

2020-06-17 12:28:57

=====

n : 252
nf : 3985 pairs
Time : 00:00:10

Density contrast

Normalize : False
Delaunay : False
Clip radius : 96.419
Iterations : 46521
K : 1.414

Best-Fit Ellipses

Max	Min	R	ϕ	C
25.7329	16.3904	1.570	28.00°	1.691497
25.8691	16.2699	1.590	28.50°	1.689513
25.7064	16.2699	1.580	28.50°	1.689057
25.7064	16.2699	1.580	28.30°	1.683483
25.5437	16.2699	1.570	29.40°	1.677375
25.8390	16.1494	1.600	28.00°	1.676166
25.6775	16.1494	1.590	28.00°	1.675463
25.6462	16.0289	1.600	28.40°	1.673105
25.6462	16.0289	1.600	28.00°	1.656090
25.3086	16.8724	1.500	29.00°	1.654347

Mean of Best-Fit Ellipses

ne = 10
R = 1.578
 ϕ = 28.40°
R 95% = 0.022
 ϕ 95% = 0.70°

The solutions are in decreasing order of C , so the best is the first in the list. A mean is given for the top 10 results, this may be changed by setting the parameter *Results*. As the solution is arrived at by a parameter search, it can be fairly slow. The *Optimize* option speeds up the search considerably by refining the solution rather than doing an exhaustive search.

A bootstrap confidence option is not given for the density contrast method as, even using an optimized search, the computational time required makes it impractical. Section 3.3.8 gives a comparison

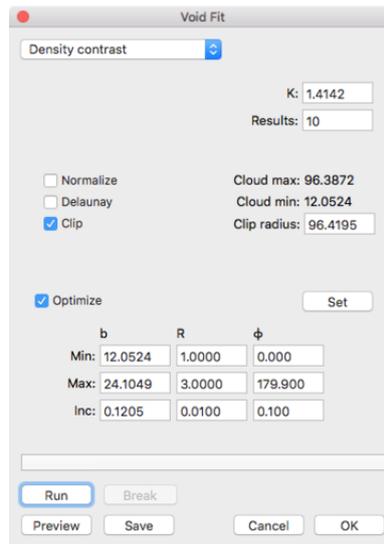


Figure 3.17: The *Void Fit* dialog displaying the *Density contrast* pane. This method uses a parameter search through increments of Radius, R , and ϕ to find the best solution.

of the void fitting methods, and suggests other methods are more accurate, and better suited for statistical analysis.

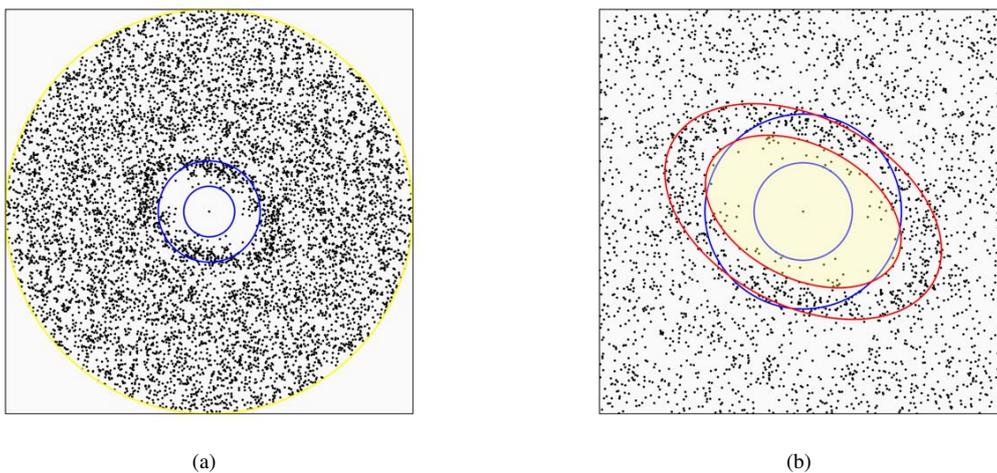


Figure 3.18: Fry plots of the data in file Ramsay and Huber 1983 F7-7 illustrating the density contrast method. The settings are automatically determined using the *Set* button, but can be modified. The *Clip radius* is reduced to 60 to speed up the search. The *Plot radius* = 60. (a) The two inner blue circles represent the minimum and maximum search values for the short axis of the void fit ellipse. The outer yellow circle is the maximum search radius. (b) Plot of the best-fit ellipse using the selected density contrast options. The red ellipses define the best-fit annulus, both have the same aspect ratio and orientation, the inner defines the void fit.

3.3.4 Exponential Edge Detection

Waldron and Wallace (2007) suggested a second method, *exponential edge detection* (EED, renamed here from *continuous function* with the approval of J. Waldron) that also does not require any information about particle shape. Again, this gives an advantage in terms of the speed of data collection, and where shape information is not available, such as their example of the spacing of dewatering pipes. Additionally, the analysis is entirely independent of particle shape, so may be used to complement ellipse based methods. If the object shape parameters $[a_i, b_i, \phi_i]$ are available, however, the plot can be normalized. The method maximizes an exponential function, $Z' = f[a, b, \phi]$, that is calculated for

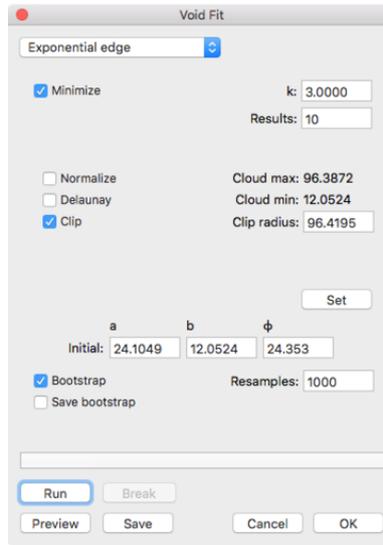


Figure 3.19: The *Void Fit* dialog displaying the *Exponential edge* pane. The *Minimize* option is selected, to use function minimization rather than a parameter search, and k , is set to the default of 3. The initial values of $[a, b, \phi]$ are estimated using the *Set* button.

all points in the search radius. The deviation of a Fry point, d_f from a solution ellipse is

$$d_f = (r_f/r_{fe}) - 1 \quad (3.3)$$

where r_f is the distance of the point from the plot center, and r_{fe} is the radius of the ellipse. d_f will be negative for points inside the ellipse, and positive for points outside. An exponential function, normalized by distance from the plot center, is

$$z = \frac{d_f}{r_f} e^{-(kd_f)^2} \quad (3.4)$$

is used to locate the steepest gradient. The sum of the z values, corrected for plot radius and number of points, Z' is

$$Z' = \frac{k^2 r_{fmax}^2}{n} \sum_{i=1}^n z_i \quad (3.5)$$

This function is minimized, to find Z'_{opt} , and the optimal value is given as a dimensionless measure of fit, Z^*

$$Z^* = \frac{Z'_{opt}}{\sqrt{ab}} \quad (3.6)$$

The minimization can done either by an optimized parameter search, as was done for the density contrast method, or more efficiently, by using function minimization (Press et al., 2007), as done in this example.

In contrast to the enhanced method, which fits an ellipse through a subset of points near the void edge, this procedure locates the ellipse that defines the edge of the void by looking for the steepest density gradient. The parameters are the void ellipse long radius, a , short radius, b , and orientation, ϕ . An additional user defined parameter, k , is by default set to $k = 3$, as suggested by Waldron and Wallace (2007), and affirmed by Kumar et al. (2014). The *Exponential edge* dialog pane is shown in Figure 3.19.

The parameters $[a, b, \phi]$ must be set to initial estimated values. These can be automatically set to suggested initial values by pressing the *Set* button, similar to the density contrast method, or can be set manually. Figure 3.20a is a Fry plot with suggested initial parameters automatically selected. The resulting solution is shown graphically in Figure 3.20b, and the results are as follows:

Void Fit Results

Ramsay and Huber 1983 F7-7

2022-06-07 12:32:58

```

=====
n          : 252
nf         : 3985 pairs
Time       : 00:00:00
Exponential edge detection
  Normalize      : False
  Delaunay       : False
  Clip radius    : 96.419
  Minimize       : True
  Iterations     : 219
  k              : 3.000

```

Best-Fit Ellipses

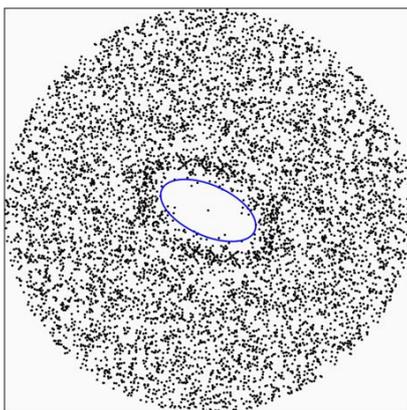
Max	Min	R	ϕ	Z'	Z^*
26.8921	16.4278	1.637	25.53°	33.205496	1.579820
26.8921	16.4278	1.637	25.53°	33.205496	1.579820
26.8921	16.4278	1.637	25.53°	33.205496	1.579820
26.8921	16.4278	1.637	25.53°	33.205496	1.579820
26.8921	16.4278	1.637	25.53°	33.205496	1.579820
26.8921	16.4278	1.637	25.53°	33.205496	1.579820
26.8921	16.4278	1.637	25.53°	33.205496	1.579820
26.8921	16.4278	1.637	25.53°	33.205496	1.579820
26.8921	16.4278	1.637	25.53°	33.205496	1.579820
26.8921	16.4278	1.637	25.53°	33.205496	1.579820
26.8921	16.4278	1.637	25.53°	33.205496	1.579820
26.8921	16.4278	1.637	25.53°	33.205496	1.579820
26.8921	16.4278	1.637	25.53°	33.205496	1.579820
26.8921	16.4278	1.637	25.53°	33.205496	1.579820
26.8921	16.4278	1.637	25.53°	33.205496	1.579820

Mean of Best-Fit Ellipses

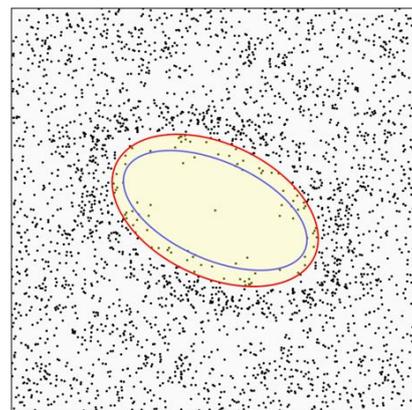
```

ne      = 10 Best-fit ellipses
R       = 1.637
 $\phi$    = 25.53°

```



(a)



(b)

Figure 3.20: Fry plots of the data in file Ramsay and Huber 1983 F7-7 illustrating the exponential edge detection method. The initial search parameters are automatically chosen using the *Set* button. (a) Preview of the exponential edge detection initial parameters shown by the blue ellipse. (b) Plot of the solution, zoomed into a radius of 50, showing the best-fit void ellipse in red.

The minimization procedure converges in less than one second, and all of the 10 best solutions are

identical at the output precision. The solutions are listed in decreasing order of Z' , so the best is the first in the list.

Confidence intervals for $[R, \phi]$ can be calculated using bootstrapping, as in the enhanced, enhanced normalized, and enhanced normalized Delaunay methods. Prior to bootstrapping, it is suggested that the minimization be done once, then repeated by entering the solution as the new initial parameters. In this example, there is no change in the output values. Then, after refining the solution, select the bootstrap option to calculate the confidence intervals. Figure 3.21 shows fabric plots of 1000 resample means used for the confidence intervals, and the results are:

Void Fit Results

Ramsay and Huber 1983 F7-7

2020-06-17 13:40:39

=====

n : 252
 nf : 3985 pairs
 Time : 00:03:08

Exponential edge detection

Normalize : False
 Delaunay : False
 Clip radius : 96.419
 Minimize : True
 Iterations : 1000
 k : 3.000

Best-Fit Ellipses

Max	Min	R	ϕ	Z'	Z^*
26.8921	16.4278	1.637	25.53°	33.205496	1.579820
26.8921	16.4278	1.637	25.53°	33.205496	1.579820
26.8921	16.4278	1.637	25.53°	33.205496	1.579820
26.8921	16.4278	1.637	25.53°	33.205496	1.579820
26.8921	16.4278	1.637	25.53°	33.205496	1.579820
26.8921	16.4278	1.637	25.53°	33.205496	1.579820
26.8921	16.4278	1.637	25.53°	33.205496	1.579820
26.8921	16.4278	1.637	25.53°	33.205496	1.579820
26.8921	16.4278	1.637	25.53°	33.205496	1.579820
26.8921	16.4278	1.637	25.53°	33.205496	1.579820
26.8921	16.4278	1.637	25.53°	33.205496	1.579820

Bootstrap Confidence

nr = 1000 Resamples
 R = 1.637
 ϕ = 25.53°
 R 95% = 0.171
 ϕ 95% = 6.20°
 dH 95% = 7.70°

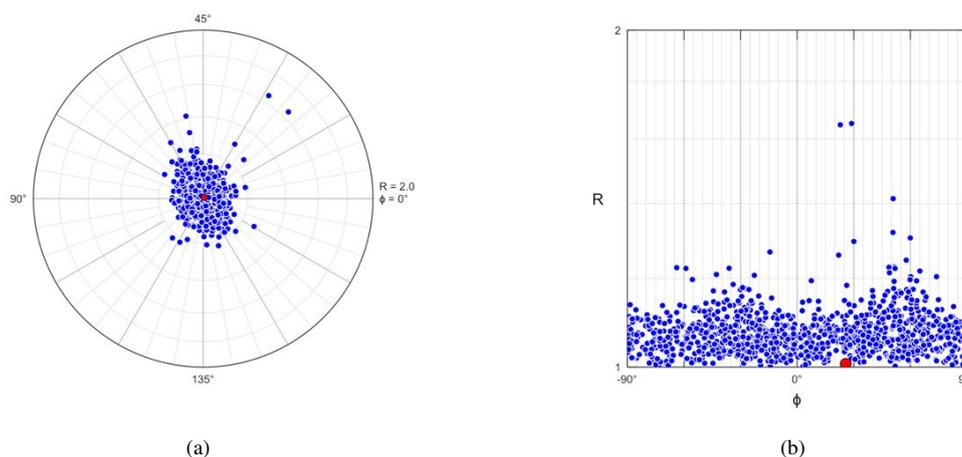


Figure 3.21: Fabric plots of the resample means of 1000 bootstrapped resamples used for the determining confidence intervals for the exponential edge detection method. The resample means are rotated (undeformed) to the sample mean, the red circle is the mean of the resample means. The scatter in the plots reflects the confidence in the result. (a) Elliott (equidistant) polar plot. (b) $\ln R_f / \phi$ plot.

3.3.5 Mean Log Likelihood

Shan and Xiao (2011) suggest a mean log likelihood function (MLLF) method where they examine the statistics of a truncated Poisson distribution, and define the MLLF as the average sum of the log probability distribution function (PDF) of each individual point in the deformed state. This is related to the density distribution around each point.

The PDF in the deformed state is related to the pre-deformation PDF by the shape and orientation of the central void, giving as parameters a cutoff distance, the ratio R , and the orientation ϕ . The function is complex however, and is solved using a parameter search to locate the maximum MLLF. The search is over the range $\phi = [0^\circ \dots 179^\circ]$ in steps of 1° , and $R = [1 \dots 20]$ in steps of 0.1. Once R and ϕ are determined, the sample is retro-deformed, and a 50 step search is done to locate the cutoff radius.

Shan and Xiao (2011) further suggest an approach to improve the results using a cross-validation technique for detecting spurious points by sequentially removing up to 10 points, and repeating the search. These algorithms were implemented by Y. Shan in a Fortran program which was reimplemented in EllipseFit after careful testing to insure that identical results are obtained.

The results are the best estimates values of R , ϕ , initial cutoff distance, and a set of neighborhood points. This method has advantages in that it is a robust numerical solution, and one that uses all of the points to define the central void. A disadvantage of the method is the computing time required to calculate the solution. In particular, the cross-validation can take several hours.

To run a test sample open the file MLLF Test 60.tsv. This data is a 60 point oolite sample carefully selected from the Ramsay and Huber 1983 F7-7.tsv data file to avoid spurious points, and to avoid a directional bias. In the *Mean log likelihood* pane of the *Void Fit* dialog, uncheck *Cross validate*, and press *Run*.

The *Void Fit* dialog displays the progress in its status bar, showing the search iteration passes in degrees, and is done at 180. The process should complete in about a minute, and the results displayed in the *Log* window, and on a Fry plot (Figure 3.22a). The green markers highlight the Fry neighbor points, those that maximize the MLLF after an intensive grid search. The results reported in the log file are:

```
Void Fit Results
MLFF Test 60
2020-06-17 14:01:49
```

=====
 N = 60

MLLF Calculations

Pass	Mean LL	R	Phi	Cutoff	Stat	Density
0	-0.31829	1.90	25.00	86.98953	0.67361	0.84687

MLLF Results

Point statistics:

Number	= 60
Calculated density	= 0.00004
Real density	= 0.00000

Results:

Mean log-likelihood	= -0.31829
R, strain ratio	= 1.90000
Phi, angle of max strain axis	= 25.00000
Cutoff radius	= 86.98953

Finished: 2020-06-17 14:03:12

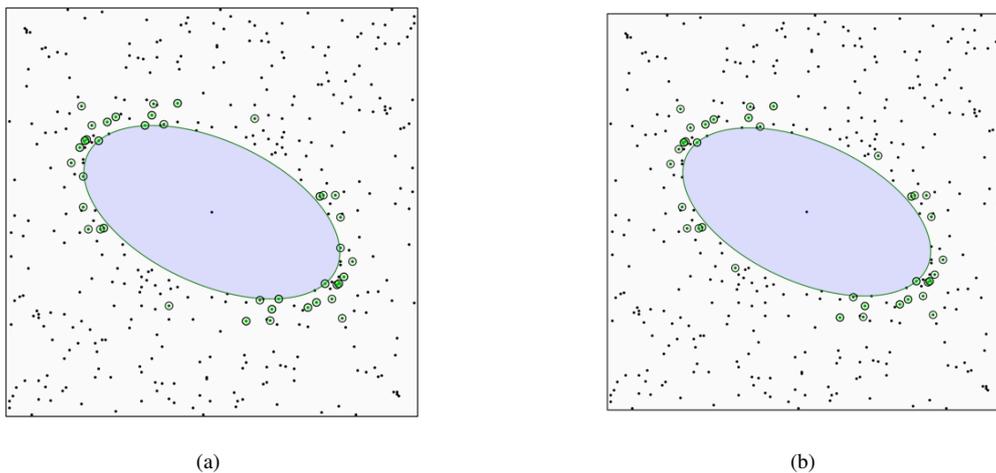


Figure 3.22: Fry plots of the data in file MLLF Test 60.tsv illustrating the mean log likelihood method (MLLF). The method uses all of the data points, so only a selected subset of the Ramsay and Huber 1983 F7-7.tsv data was used. The green markers highlight the Fry neighbor points. (a) Plot of the solution after running the method without cross validation. (b) Plot of the solution after cross-validation. .

To test the cross validation procedure, select the *Cross validation* option, and *Run*. There are now three iteration passes displayed, the first is 0 to 10, where 0 is the first calculation as done above. Passes 1 to 10 are the cross validation iterations, 1 to 60 are the data points, and 1 to 180 are the ϕ grid search in degrees. The R grid search values (0.1 to 20.0 by default), and the 1 to 50 distance search loops are not displayed. The MLLF search is computationally intensive, especially for cross-validation, this test run took about 6 hours. The search can be canceled at any time, and the results of the completed passes will be displayed.

Mean Ellipse Calculations

MLLF Test 60.tsv

2014-05-31 16:30:46

=====
 N = 60

MLLF Calculations

Pass	Mean LL	R	Phi	Cutoff	Stat	Density
0	-0.31829	1.90	25.00	86.98953	0.67361	0.84687
1	-0.31610	1.90	25.00	86.98953	0.68773	0.86122
2	-0.31603	1.90	25.00	86.98953	0.69522	0.87607
3	-0.31882	1.90	25.00	86.98953	0.67496	0.89144
4	-0.31651	1.90	25.00	86.98953	0.68968	0.90736
5	-0.31536	1.90	25.00	86.98953	0.70494	0.92386
6	-0.32428	1.80	23.00	87.24708	0.68393	0.93542
7	-0.31554	1.90	25.00	86.98953	0.69945	0.95872
8	-0.31327	1.90	25.00	86.98953	0.71578	0.97716
9	-0.31454	1.80	23.00	87.24708	0.69591	0.99044
10	-0.31451	1.90	25.00	86.98953	0.69099	1.01624

MLLF Results

Point statistics:

Number	= 52
Calculated density	= 0.00004
Real density	= 0.00004

Results:

Mean log-likelihood	= -0.31327
R, strain ratio	= 1.90000
Phi, angle of max strain axis	= 25.00000
Cutoff radius	= 86.98953

Finished: 2014-05-31 22:49:58

The results of pass 0 are identical to the previous result, however the cross-validation procedure located a slightly better solution, in pass 8 the mean log likelihood is -0.31327, instead of -0.31829. The resulting Fry plot with 8 less neighbor points is shown in Figure 3.22b.

Kumar et al. (2014) concluded that the maximum likelihood method gave less accurate results than other methods, possibly because the non-random point distribution in their simulated samples violated the method's requirement of a homogeneous truncated Poisson distribution. Section 3.3.8 compares the results to other methods.

3.3.6 Weighted Least-Squares

The weighted least squares method attempts to minimize a least-squares function fitting a one-sided data cloud boundary by applying a high weighting to points that lie inside the boundary, and a weight of 1 to points that lie outside (Cardiel, 2009; Mulchrone, 2013; Mulchrone et al., 2013). The method used follows that of Mulchrone (Mulchrone, 2013; Mulchrone et al., 2013), however using Delaunay neighbors is optional.

The solution uses a parameter search similar to the density contrast method (Section 3.3.3). This is an optimized, or exhaustive, search through the parameters, $[b, R, \phi]$, the void fit ellipse's short radius, axial ratio, and orientation of the long axis. The default search settings are given by Eq 3.2, and can be automatically determined using the *Set* button, or entered manually. The *Clip radius* can be lowered from the default to speed up the search.

The first example uses a weighted least squares search without using Delaunay nearest neighbors. Figure 3.23 shows the settings pane and Figure 3.24a is the preview of automatic function search options. The blue circles are the minimum and maximum search radii for the void ellipse short axis, b . Figure 3.24b is a zoomed in plot of the solution:

Void Fit Results

Ramsay and Huber 1983 F7-7

2020-06-17 16:15:09

```

=====
n          : 252
nf         : 3985 pairs
Time       : 00:00:12
Weighted Least Squares
  Normalize      : False
  Delaunay       : False
  Clip radius    : 96.419
  Minimize       : False
  Iterations     : 47061
   $\zeta$           : 2000
Best-Fit Ellipses
  Max   Min   R    $\phi$    g
  25.8691 16.2699 1.590 27.60° 10193724.92
  25.8691 16.2699 1.590 27.50° 10193744.76
  25.8691 16.2699 1.590 27.40° 10193794.95
  25.8691 16.2699 1.590 27.30° 10193875.42
  25.7064 16.2699 1.580 27.60° 10193963.82
  25.7064 16.2699 1.580 27.50° 10193969.02
  25.7064 16.2699 1.580 27.40° 10194002.81
  25.7064 16.2699 1.580 27.30° 10194065.15
  25.7064 16.2699 1.580 27.20° 10194155.99
  25.7064 16.2699 1.580 27.10° 10194275.28
Mean of Best-Fit Ellipses
  ne      = 10 ellipses
  R        = 1.584
   $\phi$       = 27.39°
  R 95%    = 0.004
   $\phi$  95%  = 0.13°

```

The second example is a weighted least squares search using the *Delaunay* option. *Clip* is set off as the point cloud is already reduced by the triangulation. Figure 3.25a is a zoomed in plot of the best solution:

Void Fit Results

Ramsay and Huber 1983 F7-7

2020-06-19 15:09:01

```

=====
n          : 252
nf         : 717 pairs
Time       : 00:00:02
Weighted Least Squares
  Normalize      : False
  Delaunay       : True
  Clip radius    : False
  Iterations     : 46620
   $\zeta$           : 2000
Best-Fit Ellipses

```

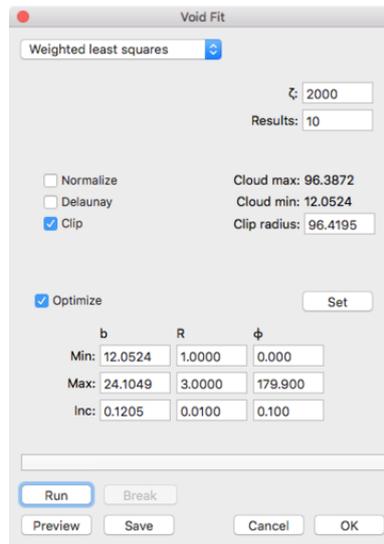


Figure 3.23: The *Void Fit* dialog displaying the *Weighted least squares* pane. This method uses a parameter search through increments of b , R , and ϕ to find the best solution. The parameter limits and increments were chosen automatically using the *Set* button, but can also be entered manually.

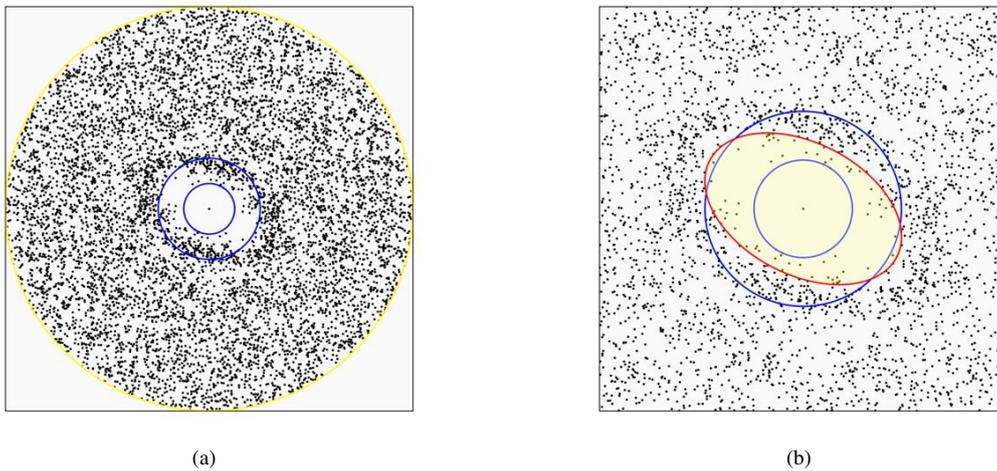


Figure 3.24: Fry plots of the data in file Ramsay and Huber 1983 F7-7 illustrating the weighted least squares method. The settings were automatically determined using the *Set* button, but can also be entered manually. The two inner blue circles represent the minimum and maximum search values for the short axis of the void fit ellipse, b . The outer yellow circle is the maximum search radius. (a) Plot showing the initialized search parameter limits. (b) Zoomed in plot of the best solution, shown by the red ellipse. The plot radius is 50.

Max	Min	R	ϕ	g
18.3966	12.7754	1.440	19.90°	351693.62
18.3966	12.7754	1.440	19.80°	351694.80
18.3966	12.7754	1.440	19.70°	351697.47
18.3966	12.7754	1.440	19.60°	351701.61
18.3966	12.7754	1.440	19.50°	351707.21
18.3966	12.7754	1.440	19.40°	351714.28
18.3966	12.7754	1.440	19.30°	351722.79
18.2688	12.7754	1.430	19.70°	351729.52
18.2688	12.7754	1.430	19.60°	351729.58
18.2688	12.7754	1.430	19.50°	351731.06

Mean of Best-Fit Ellipses
 ne = 10 ellipses
 R = 1.437
 ϕ = 19.6°
 R 95% = 0.004
 ϕ 95% = 0.17°

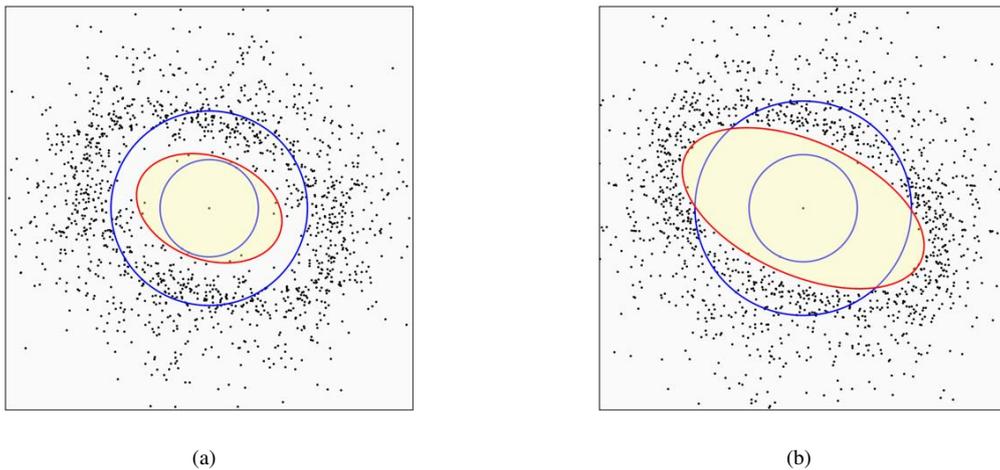


Figure 3.25: Fry plots of the data in file Ramsay and Huber 1983 F7-7 illustrating the weighted least squares method with the Delaunay option. The initial search parameters were automatically chosen using the *Set* button, but *Clip* is turned off as the cloud has already been reduced by the triangulation. The blue circles represent the search range for the ellipse short axis, *b*. The red ellipse is the best solution. (a) Plot of solution using the *Delaunay* option only. The plot radius is 50. (b) Plot of solution using the *Normalized* and *Delaunay* options. The normalized plot radius is 1.3.

The final example is a weighted least squares search using both the *Normalize* and *Delaunay* nearest neighbors options. Again, *Clip* is set off as the point cloud is already reduced by the triangulation. Figure 3.25b is a zoomed in plot of the best solution:

```

Void Fit Results
Ramsay and Huber 1983 F7-7
2020-06-19 15:32:53
=====
n          : 252
nf         : 717 pairs
Time      : 00:00:02
Weighted Least Squares
  Normalize      : True
    
```

Delaunay : True
 Clip radius : False
 Iterations : 47061
 ζ : 2000

Best-Fit Ellipses

Max	Min	R	ϕ	g
0.8243	0.4293	1.920	24.40°	209.29
0.8243	0.4293	1.920	24.30°	209.30
0.8243	0.4293	1.920	24.20°	209.30
0.8243	0.4293	1.920	24.10°	209.31
0.8243	0.4293	1.920	24.00°	209.32
0.8243	0.4293	1.920	23.90°	209.34
0.8243	0.4293	1.920	23.80°	209.36
0.8243	0.4293	1.920	23.70°	209.38
0.8261	0.4258	1.940	24.20°	209.39
0.8261	0.4258	1.940	24.10°	209.39

Mean of Best-Fit Ellipses

ne = 10 ellipses
 R = 1.924
 ϕ = 24.07°
 R 95% = 0.006
 ϕ 95% = 0.16°

3.3.7 Error Analysis

Bootstrap error analysis (Efron, 1979) is a powerful technique for calculating confidence regions. It is nonparametric, meaning that it is not necessary to assume the sample comes from a population with a particular distribution, and it may be applied to small samples, less than 25 data points. Resamples of the sample are created by random resampling with replacement, and the mean of the resample is calculated. This is done hundreds or thousands of times to create a sample of resample means. The dispersion in these means is used to determine confidence intervals (Figures 3.10, 3.11, 3.15, 3.16, and 3.21).

Bootstrap error analysis is feasible for void fitting routines that are not overly time intensive (Table 3.1). McNaught (1994) similarly used a bootstrap technique by resampling the particle data points 100 times, while McNaught (2002) used 100 resamples of the Fry points. Computational speeds now allow thousands of resamples, depending on the void fitting method used, and a minimum of 1000 is suggested.

The procedure followed is to form a resample of the data sample that is the same size as the sample, by randomly selecting data points, without removing them from the sample, that is, *with replacement*. A solution, the mean, is calculated for the resample, and the process repeated. The dispersion of the resample means is related to the confidence in the sample mean, and allows determination of 95%, or other, confidence regions, by sorting the resample means by distance from the sample mean. These are reported as R 95%, ϕ 95%, and d_H 95%. d_H 95% is the confidence as a *hyperbolic distance*, a single number that represents both R 95% and ϕ 95% (Section 6.2.3).

The bootstrap resamples can be saved to a file by selecting the *Save bootstrap* option, if available. This file can then be used to determine confidence intervals when constructing a fabric ellipsoid from section data (Section 7.4.3).

3.3.8 Comparison of Void Fitting Methods

As discussed previously, Kumar et al. (2014) reviewed six void fitting methods, including weighted least-squares Delaunay (DTN), density contrast (point-count), exponential edge detection (EED, or

continuous function), and mean log likelihood methods, using two-dimensional simulated data sets, and concluded that of those six, the EED method is the most accurate, followed by the DTN method. The weighted least-squares method with the Delaunay option implemented here follows their DTN.

Table 3.1 is a summary of the results of the example analyses presented in this chapter. While the examples presented here are a limited set of tests, some conclusions were drawn after extensive time implementing and testing the various methods.

Of the methods that are independent of particle shape $[a_i, b_i, \phi_i]$, and only depend on $[x_i, y_i]$ (Table 3.1), the exponential edge detection method is robust (Figure 3.21), and fast enough that bootstrap confidence intervals can be calculated in a few minutes. The density contrast method requires a parameter search, so is relatively slow and less suitable for bootstrapping. Kumar et al. (2014) concluded that it was less accurate. The weighted least-squares function method was found to be difficult to minimize robustly, so a parameter search is used. The maximum likelihood method (Shan and Xiao, 2011) is extremely computationally intensive, and did not return results consistent with other methods. Kumar et al. (2014) also concluded that it gave less accurate results.

Of the methods that also require particle shape, $[a_i, b_i, \phi_i]$, the enhanced normalized method is fast, robust, and suitable for bootstrapping (Figure 3.11). Restricting the method to Delaunay nearest neighbors speeds up the analysis, but significantly reduces confidence in the result (Figures 3.10, 3.11, 3.15, and 3.16; Table 3.1).

Method	R	ϕ	R 95%	ϕ 95%	d_H	x_i, y_i
Enhanced	1.662	25.83	0.142	2.78	5.77	
Enhanced Normalized	1.622	24.43	0.053	2.69	3.23	
Enhanced Delaunay	1.661	25.85	1.861	10.95	47.13	
Enhanced Normalized Delaunay	1.621	24.45	0.621	24.45	27.69	
Density Contrast	1.578	28.40				✓
Exponential Edge Detection	1.637	25.53	0.171	6.20	7.70	✓
Mean Log Likelihood (N = 60)	1.90	25.00				✓
Weighted Least-Squares	1.584	27.39				✓
Weighted Delaunay Least-Squares	1.440	19.90				✓
Weighted Normalized Delaunay Least-Squares	1.920	24.40				
Eigenvector Mean	1.628	25.74	0.034	1.00	1.44	

Table 3.1: Summary of example results of void fitting methods on data file Ramsay and Huber 1983. Bootstrap confidence intervals are given if implemented, bootstrapping was not implemented if impractical due to the required processing time (Section 3.3.7). The *Enhanced* methods all use a selection factor of 1.2. If x_i, y_i is checked, it means that ellipse data, R_i, ϕ_i is not required. The eigenvector results for the particle mean ellipse are given for comparison. Figure 3.26 is a summary comparison of the results.

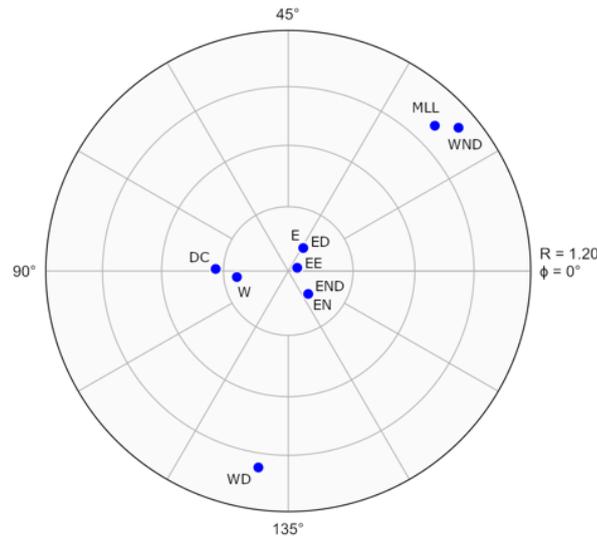


Figure 3.26: Elliott (equidistant) polar plot summarizing the results of the methods listed in Table 3.1. The results are all retrodeformed to the eigenvector mean of the particle ellipses, at center, so the radial distance is a measure of the difference between the mean particle ellipse and the void fit ellipse. DC - density contrast, E - enhanced, ED - enhanced Delaunay, EN - enhanced normalized, END - enhanced normalized Delaunay, EE - exponential edge detection, MLL - mean log likelihood (partial data set), W - weighted least-squares, WD - weighted least-squares Delaunay, WND - weighted least-squares normalized Delaunay.

4 Strain from Displacements

In certain deformation studies the positions of scattered markers are determined at intervals in time to give a displacement field, from which it is desired to estimate local or regional strains or strain rates. Examples include studies of glacier flow, intra-continental deformation using GPS survey markers, slope creep, and analogue laboratory experiments using imbedded markers (Means, 1983). The relationships between strain and displacements are given by continuum mechanics theory (Malvern, 1969). Equations describing these relationships and their geologic applications are given by Ramsay (1967), Elliott (1970), Means (1976), and Ramsay and Huber (1983). Robin (2019)) gives an excellent review of such applications with additional references.

Graphical and numerical methods for the estimation of strain from displacements are implemented. The graphical method is a *displacement stretch plot*, originally implemented by Vollmer as a Fortran program to prepare strain diagrams for analog see-through deformation experiments (Means, 1983; Vollmer, 2019). This plot can be quantified by fitting a least-squares ellipse (Vollmer, 2019). The second method is an implementation of the strain probe of Robin (2019), which gives estimates of the tensor quantities associated with the deformation.

Displacement data requires the specification of the locations, $[x_i, y_i]$, of a set of markers at sequential times. Each object, or marker, must have a unique *Station* identifier, which allows it to be tracked through time. A column *Time ID*, contains a sequential integer specifying the time frame at which the object's location was measured. The file Schweinberger (Robin 2019).ods is provided as an example data set. This is a small subset of data collected from an analogue norcamphor experiment by Schweinberger and Fueten, that is provided as an example data file by Robin (2019). The file header and first six lines of data are shown in Table 4.1.

ID	Station	Time ID	X	Y
1347	199	1	575	364
1348	199	2	575	372
1349	199	3	576	386
1350	199	4	599	400
1351	199	5	631	409
1352	199	6	664	416

Table 4.1: Example data file headers and first six lines of data for displacement analysis. The file contains data from 6 objects (*Station*: 199, 202, 208, 209, 212, and 213) at 28 time frames (*Time ID*: 1 to 28), and is a small subset of a much larger dataset. The objects were embedded particles used to track flow during a see-through analogue deformation experiment by Schweinberger and Fueten. See example file Schweinberger (Robin 2019).ods.

4.1 Displacement Stretch Plot

A graphical method was initially implemented in Fortran to estimate strain from displaced markers in see-through analogue deformation experiments of octochloropropane (Means, 1983; Vollmer, 2019), but is applicable to any similar displacement data. For a set of n initial marker object positions $[x_i, y_i]$, and final positions $[x'_i, y'_i]$ (Figure 4.3a) the stretches and their orientations are calculated for each combination of object pairs, giving:

$$n_s = n(n-1)/2 \quad (4.1)$$

object pairs. Taking the subscript $k = [1 \dots n_s]$ to denote combinations of object pairs, $[x_i, y_i]$ and $[x_j, y_j]$, the initial and final distances between them, d_k and d'_k , are:

$$\begin{aligned} d_k &= [(x_j - x_i)^2 + (y_j - y_i)^2]^{1/2} \\ d'_k &= [(x'_j - x'_i)^2 + (y'_j - y'_i)^2]^{1/2} \end{aligned} \quad (4.2)$$

and the stretches, S_k , and their orientations, α_k , are:

$$\begin{aligned} S_k &= d'_k / d_k \\ \alpha_k &= \arctan [(y'_j - y'_i) / (x'_j - x'_i)] \end{aligned} \quad (4.3)$$

The stretches and their orientations define an estimated strain ellipse with respect to the initial coordinates (Lagrangian), with coordinates:

$$\begin{aligned} x_k &= (x_i' - x_j')/d_k \\ y_k &= (y_i' - y_j')/d_k \end{aligned} \quad (4.4)$$

Since the stretches defining the ellipse are symmetrical, the number of points defining it is $n_p = 2n_s$, where for $k = [n_s + 1 \cdots 2n_s]$:

$$[x_k, y_k] = [-x_{k-n_s}, -y_{k-n_s}] \quad (4.5)$$

The example data file Schweinberger (Robin 2019).ods, with 6 points, therefore gives 30 points defining the estimated strain ellipse (Figure 4.3b).

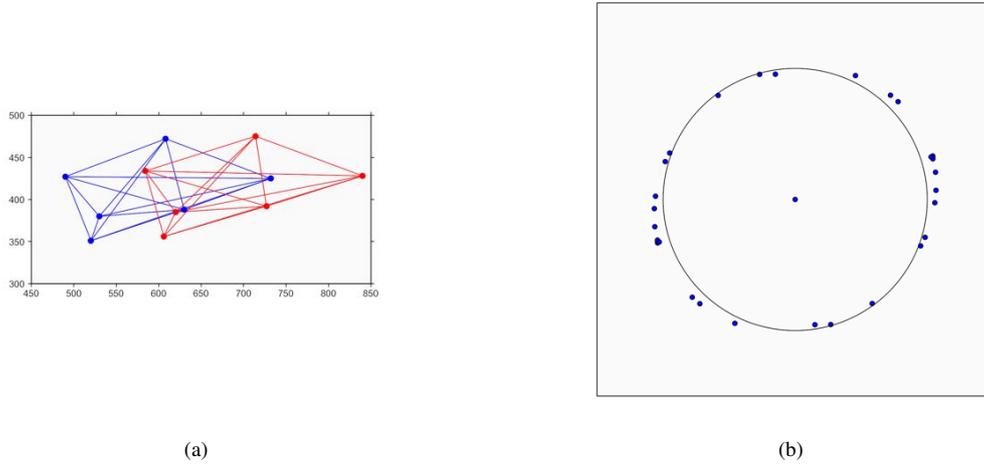


Figure 4.1: Plots of the Schweinberger (Robin 2019).ods using coordinates of 6 markers at initial time 8, final time 11, chosen to compare with the results of Robin (2019). (a) Displacement map showing the initial (blue) and final (red) coordinates of the markers. The lines are the 15 initial (blue) and final (red) lines used to calculate the stretches. (b) Displacement stretch plot of the data with unit circle superimposed.

To quantify the displacement stretch plot (Figure 4.3b), a best-fit least squares ellipse can be calculated (Vollmer, 2019). The method minimizes the sum of the squares of the radial residuals from the estimated ellipse (Fitzgibbon et al., 1996; Haliř and Flusser, 1998). This is simplified if the ellipse is centered at the origin. Given the n_p points $[x_k, y_k]$, the matrixes D and E :

$$\begin{aligned} D &= \sum_{k=1}^{n_p} \begin{bmatrix} x_k^4 & x_k^3 y_k & x_k^2 y_k^2 \\ x_k^3 y_k & x_k^2 y_k^2 & x_k y_k^3 \\ x_k^2 y_k^2 & x_k y_k^3 & y_k^4 \end{bmatrix} \\ E &= \sum_{k=1}^{n_p} \begin{bmatrix} x_k^2 \\ x_k y_k \\ y_k^2 \end{bmatrix} \end{aligned} \quad (4.6)$$

are formed, and the equation:

$$Db = E \quad (4.7)$$

is solved for b using LU decomposition, giving coefficients for the best-fit ellipse centered at the origin:

$$b_1 x^2 + b_2 xy + b_3 y^2 = 1 \quad (4.8)$$

The equation for the estimated strain ellipse can then be solved for estimates of the strain parameters S_1 , S_2 , R , ϕ , Δ_A (dilatation, change in area divided by initial area), and S_Z (vertical stretch assuming constant volume and two principle horizontal strains).

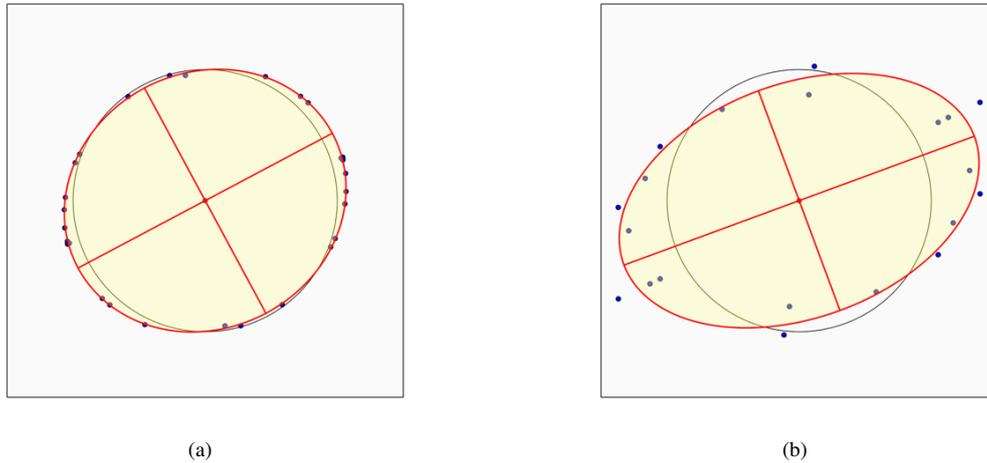


Figure 4.2: Displacement stretch plots and solution ellipses of the Schweinberger (Robin 2019).ods data using coordinates of markers at initial and final times. (a) Plot of the data from time 8 to 11. (b) Plot of the data from time 8 to 23.

To evaluate the solution, the sum of squares of errors (S_{SE}), and the RMS are calculated:

$$S_{SE} = \sum_{k=1}^{np} (b_1 x_k^2 + b_2 x_k y_k + b_3 y_k^2 - 1)^2 \quad (4.9)$$

$$RMS = \sqrt{S_{SE}/n}$$

The RMS is a measure of how well the data fits the estimated solution, and varies from 0 to 1, with 0 being a perfect fit. Figure 4.2a is a displacement stretch plot of the Schweinberger data with the least squares solution superimposed. This data consists of the initial and final coordinates of 6 markers at various times. The 6 markers, initial time 8, and final time 11, were chosen to compare with the results of Robin (2019). Figure 4.2b is a plot of the same data from time 8 to 23. The *Log* window output for time 8 to 11 is:

Displacement Strain Results
Schweinberger (Robin 2019)
2019-03-03 20:50:06

```
=====
n                = 6
Time initial     = 8
Time final      = 11
Displacement Stretch
  ns = 15 stretches
  np = 30 fitted points
Ellipse
  a          = 1.091356
  b          = 0.974929
  R          = 1.119421
  φ          = 28.1545°
Dilatation
  Δ          = 0.063995
  Sz         = 0.939854 (constant volume)
Root mean square error
  RMS       = 0.014209
Sum squared errors
```

$$\text{SSE} = 0.006057$$

4.2 Strain Probe

Robin (2019) proposed a *strain probe* method to calculate strains from displacements using a simplification resulting from a change of origin of coordinates to the object's barycenter. The following is a summary of the procedure given by Robin (2019). Robin's Eq 6 forms the basis of the method for estimating U , the deformation gradient tensor, and E , the displacement gradient tensor, from displacement data. The relationship between these tensors and the initial, $X = [x_i, y_i]$, and final, $X' = [x'_i, y'_i]$, object positions is given by:

$$\begin{aligned} X' &= UX + T \\ X' &= (I + E)X + T \\ \delta X &= EX + T \end{aligned} \quad (4.10)$$

where T is the translation of the barycenter, and I is the identity tensor. This gives estimates of U and E from which strain parameters can be extracted. For finite strain, U can be decomposed into a rotation, or spin, tensor R and a symmetric deformation tensor. Left and right decompositions are possible, however the left decomposition gives the ellipse in a Lagrangian reference frame:

$$U = U_L R \quad (4.11)$$

To perform the decomposition, the rotation angle ω and tensor R are given by:

$$\begin{aligned} \omega &= \arctan [(U_{21} - U_{12}) / (U_{11} + U_{22})] \\ R &= \begin{bmatrix} \cos \omega & -\sin \omega \\ \sin \omega & \cos \omega \end{bmatrix} \end{aligned} \quad (4.12)$$

and U_L by:

$$U_L = UR \quad (4.13)$$

The symmetric U_L tensor can then be diagonalized, and the eigenvectors give the estimated strain ellipse axes a and b , along with their orientations, ϕ and $\phi + 90^\circ$. Evaluation of the solution is done by examining the residuals, calculating S_{SE} and S_{ST} , an estimated standard deviation, σ , and a coefficient of determination, $C_D = 1 - S_{SE}/S_{ST}$, which varies from 0 to 1 with increasing goodness of fit.

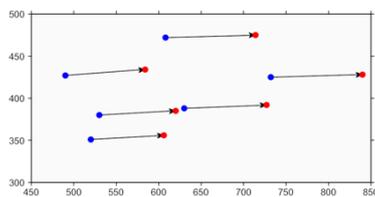
For an example calculation, open the file *Schweinberger (Robin 2019).ods*, and in the *Preferences* dialog set *Time initial* to 8, and *Time final* to 11, selecting *Strain probe Best-fit ellipse*. The log output displays:

```
Displacement Strain Results
Schweinberger (Robin 2019)
2019-03-04 14:26:50
```

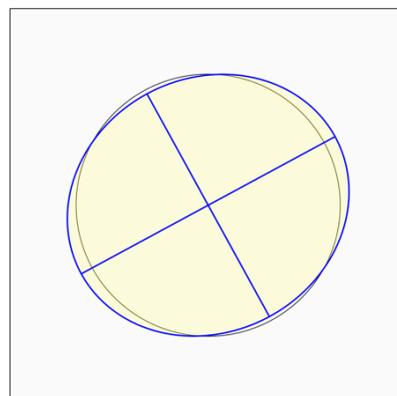
```
=====
```

```
N = 6
Time initial = 8
Time final = 11
Strain Probe
  Ellipse
    a      = 1.090186
    b      = 0.967471
    R      = 1.126842
```

ϕ = 28.6227° (61.3773°dec)
 Dilatation
 Δ = 0.054723
 S_z = 0.948116 (constant volume)
 Barycenter
 X_c = 5.850000E+002
 4.071667E+002
 Translation
 T = 9.683333E+001
 4.500000E+000
 Displacement gradient
 E = 5.931538E-002, 1.244670E-001
 -1.394354E-002, -1.712690E-003
 Rotation
 ω = -3.848367876°
 R = 9.977452E-001, 6.711620E-002
 -6.711620E-002, 9.977452E-001
 Lagrangian strain
 E_l = 6.528055E-002, 5.308916E-002
 5.308916E-002, -3.027825E-003
 Sum of squares errors
 SSE = 3.583992
 Standard deviation
 sd = 0.772873
 Sum squared total (stage ref)
 SST = 56774.000000
 Coefficient of determination (stage ref)
 CD = 0.999937
 Sum squared total (barycenter ref)
 SST = 392.333333
 Coefficient of determination (barycenter ref)
 CD = 0.990865



(a)



(b)

Figure 4.3: Plots of the Schweinberger (Robin 2019).ods using coordinates of 6 markers at initial time 8, final time 11, chosen to compare with the results of Robin (2019). (a) Displacement map showing the initial (blue) and final (red) coordinates of the markers. (b) Strain probe ellipse with unit circle superimposed.

4.3 Comparison of Methods

Tests comparing the displacement stretch plot (Vollmer, 2019), and the strain probe method (Robin, 2019), were done using example data from Robin (2019). In most cases the calculated strain ellipses are similar, however, selecting different initial and final times, can give greater disparities between the two solutions (Figure 4.4b).

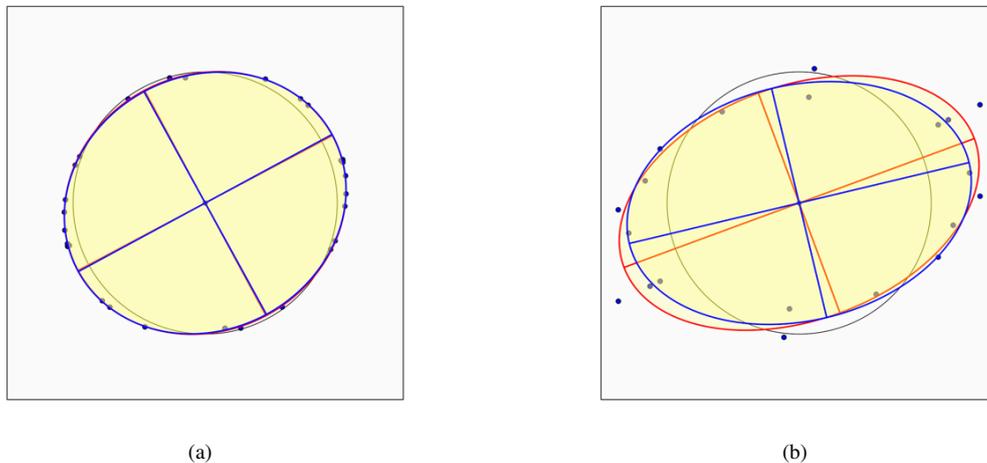


Figure 4.4: Plots of the Schweinberger (Robin 2019).ods using coordinates of 6 markers. The plots show the displacement stretch ellipse (red), the strain probe ellipse (blue) ellipse, and a unit circle (gray). (a) Plot of the data from time 8 to time 11. (b) Plot for the data at initial time 8 and final time 23.

The displacement stretch plot provides a useful representation of the data used to estimate homogeneous strain ellipse based on the measured stretches, however, the strain probe method provides estimates of the strain and the tensor quantities characterizing the deformation. The strains calculated using the strain probe method are therefore preferred over the least squares estimate.

Superimposing the displacement stretch plot on the strain probe ellipse, however, allows inspection of the data scatter, and identification of outliers. An outlier is a station whose displacement is incompatible with a homogeneous strain, and likely indicates an error or a discontinuity. The *Find* command allows the selection of such outliers, and highlights the station data in the data window.

4.4 Strain from Velocities

Neotectonic infinitesimal strain at the continental scale can be determined from the velocities of geodetic survey markers if the following data is available for each marker:

Station, E, N, VE, VN

or

Station, Lat, Long, VE, VN

Station is an alphanumeric identifier (commonly four characters), *Lat* (latitude) and *Long* (longitude) are the reference coordinates of the station, *E* and *N* are the station's easting and northing (normally in meters), and *VE* and *VN* are the east and north velocities (normally in mm/yr). If latitude and longitude are input without easting and northing, easting and northing must be calculated using the *Calculate Coordinates* command.

An example is given using 12 stations near the San Andreas fault, in the vicinity of Santa Cruz, California (Figure 4.5), which includes the epicenter of the devastating October 17, 1989 M 6.9 Loma Prieta earthquake. The data was selected from the UNAVCO GPS/GNSS velocity viewer

(<https://www.unavco.org>). It uses the North America NAM08 reference frame, with velocities in mm/yr (N, E, and Up) calculated from years of daily station surveys. The data is in the example file Santa Cruz CA velocity.ods. After opening the file, select *Edit - Select All*, then *Data - Calculate Coordinates* command, select WGS84, and press *OK* to calculate the UTM easting and northing coordinates in meters.

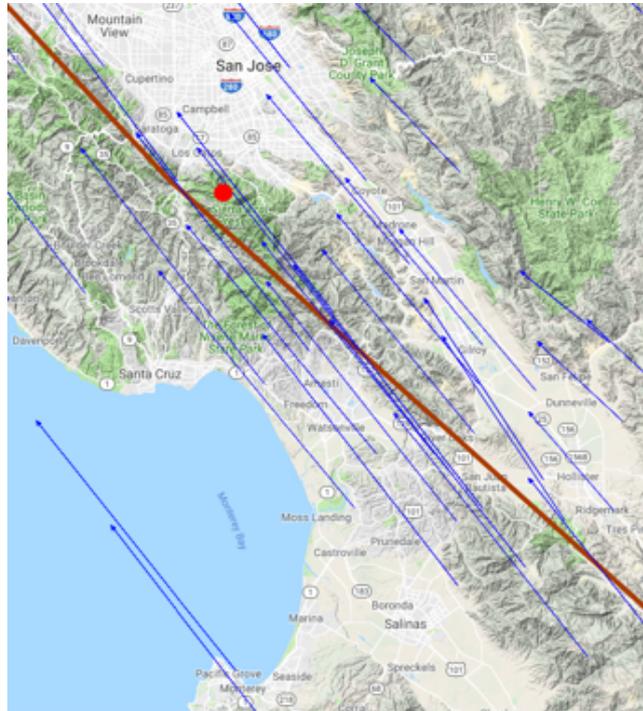


Figure 4.5: Velocity vectors in the vicinity of Santa Cruz, California. The red line is the trace of the San Andreas fault, and the red circle is the location of the October 17, 1989 M 6.9 Loma Prieta earthquake. GPS/GNSS velocity data is from the UNAVCO website. Map is a Google image.

A scaling factor must be set for the strain calculation, for this data it is scaled at 0.001 to convert the velocities in millimeters to meters. For visualization, however, the scale is set to 1000, which gives a 10^6 exaggeration (1 mm = 1000 m). Figure 4.6a is a displacement map of 12 adjacent velocity vectors (mm/yr) selected from the central portion of Figure 4.5, with a scale exaggeration of 10^6 ($Scale = 1000$). Figure 4.6b is a displacement stretch plot of the 12 velocities, with the calculated displacement stretch (blue) and strain probe (red) ellipses superimposed. This plot also has an exaggeration of 10^6 .

The displacement strain solutions, scaled at 0.001 to convert the velocities in millimeters to meters, are:

Displacement Strain Results

Santa Cruz CA velocity

2019-11-18 13:28:04

=====

N = 12

Displacement Stretch

ns = 66 stretches

np = 132 fitted points

Ellipse

a	= 1.000000
	= 191.684968 $\eta\epsilon$
b	= 1.000000
	= -289.642046 $\eta\epsilon$
R	= 1.000000

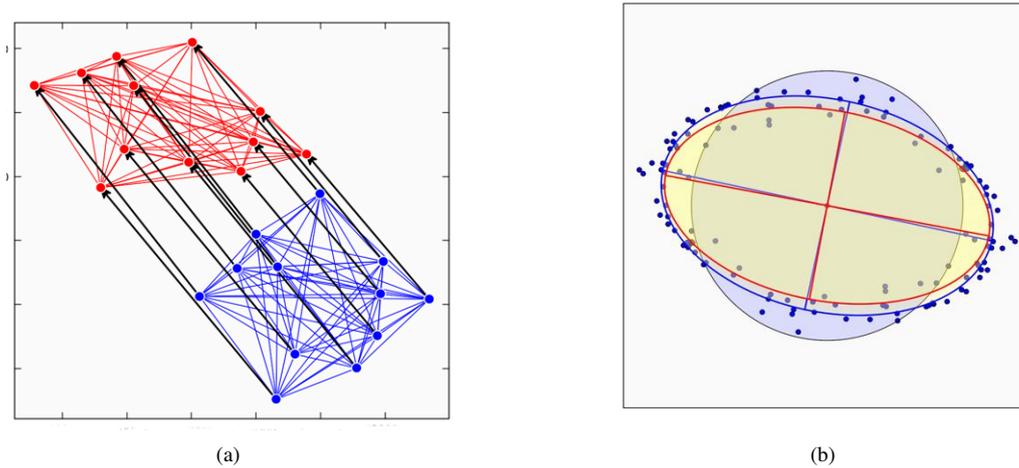


Figure 4.6: Displacement plots from the 12 selected velocities shown in Figure 4.5. The $Scale = 1000$, giving an exaggeration of 10^6 (1 mm = 1000 m). (a) Displacement map of 12 selected velocities (mm/yr) showing initial (blue) and final (red) station positions and lines used to determine the displacement stretch plot. Tick marks are spaced at 10 kilometers. (b) Displacement stretch plot of the 12 selected velocities, with the calculated displacement stretch ellipse (blue) and strain probe ellipse (red) superimposed. A unit circle is shown in blue.

$$\begin{aligned}
 &= 481.327154 \eta \epsilon \\
 \phi &= 176.1843^\circ (273.8157^\circ \text{dec}) \\
 \text{Dilatation} \\
 \Delta &= 0.000000 \\
 &= -97.957134 \eta \epsilon \\
 S_z &= 1.000000 \text{ (constant volume)} \\
 &= 97.957144 \eta \epsilon \\
 \text{Sum squared errors} \\
 SSE &= 0.000000 \\
 \text{Strain Probe} \\
 \text{Ellipse} \\
 a &= 1.000000 \\
 &= 195.836300 \eta \epsilon \\
 b &= 1.000000 \\
 &= -287.798335 \eta \epsilon \\
 R &= 1.000000 \\
 &= 483.634774 \eta \epsilon \\
 \phi &= 177.1897^\circ (272.8103^\circ \text{dec}) \\
 \text{Dilatation} \\
 \Delta &= 0.000000 \\
 &= -91.962092 \eta \epsilon \\
 S_z &= 1.000000 \text{ (constant volume)} \\
 &= 91.962101 \eta \epsilon \\
 \text{Barycenter} \\
 X_c &= 6.192401E+005 \\
 &= 4.091098E+006 \\
 \text{Translation} \\
 T &= -2.265583E-002 \\
 &= 2.799333E-002 \\
 \text{Displacement gradient} \\
 E &= 1.946737E-007, 2.457374E-007 \\
 &= -2.931053E-007, -2.866357E-007
 \end{aligned}$$

```

Rotation
  ω      = -0.000015437°
  R =    1.000000E+000, 2.694213E-007
        -2.694213E-007, 1.000000E+000
Lagrangian strain
  EI =   1.946737E-007, -2.368402E-008
        -2.368402E-008, -2.866357E-007
Sum of squares errors
  SSE    = 0.000023
Standard deviation
  sd     = 0.001120
Sum squared total (stage ref)
  SST    = 0.015849
Coefficient of determination (stage ref)
  Cd     = 0.998576
Sum squared total (barycenter ref)
  SST    = 0.000286
Coefficient of determination (barycenter ref)
  Cd     = 0.921016

```

The results are given as nano strain ($\eta\varepsilon = 10^{-9}$) per year due to the extremely small annual displacements. Easting and northing (E, N) are required for reference coordinates, normally easting and northing are UTM coordinates in meters. If latitude (*Lat*) and longitude (*Long*) are input, easting and northing can be calculated using the *Data - Calculate Coordinates* command. The standard reference coordinate system is WGS84 (World Geodetic System 1984), which gives coordinates in meters within a specified grid zone.

There are several considerations when choosing how to enter data. If survey stations straddle UTM zones, some of the stations will need to be forced into an adjacent zone. The zone for each calculated easting and northing is reported, but stations are not forced into another zone. Secondly, at high latitudes where true north and grid (UTM) north may differ significantly (convergence), a correction to the velocities (*VE*, *VN*) may be required.

The *Data - Calculate Coordinates* command option *Local* attempts to limit deviations between true north and grid north, and to avoid straddling grid zones, by setting up a local coordinate system around the stations. The local coordinate origin is centered within the stations and uses Vincenty's inverse geodetic formula (Vincenty, 1975) to calculate distances between the stations.

5 Line Data Analysis

In certain cases collections of lines may be used for the calculation of strain. This requires knowledge of initial conditions, for example the initial angles between lines, or their initial lengths. This chapter covers two two-dimensional methods, the Wellman method, a line stretch method. See Ramsay and Huber (1983) and Ragan (2009) for examples of these and related techniques. A third method is for determining the three-dimensional orientations of planar fabric elements given their traces, or intersections, with two or more sections as apparent dips.

5.1 Wellman Analysis

The Wellman method can be applied to objects in which two lines can be identified that have constant initial angles, such as brachiopod hinge and symmetry lines which are initially perpendicular (Wellman, 1962; Ramsay, 1967), Figure 5.1a. For brachiopods not parallel to a principal strain, this angle will be distorted by shear strain. Wellman's graphical technique is illustrated in many structural geology textbooks and laboratory manuals (Ramsay and Huber, 1983; Ragan, 2009; Fossen, 2016).

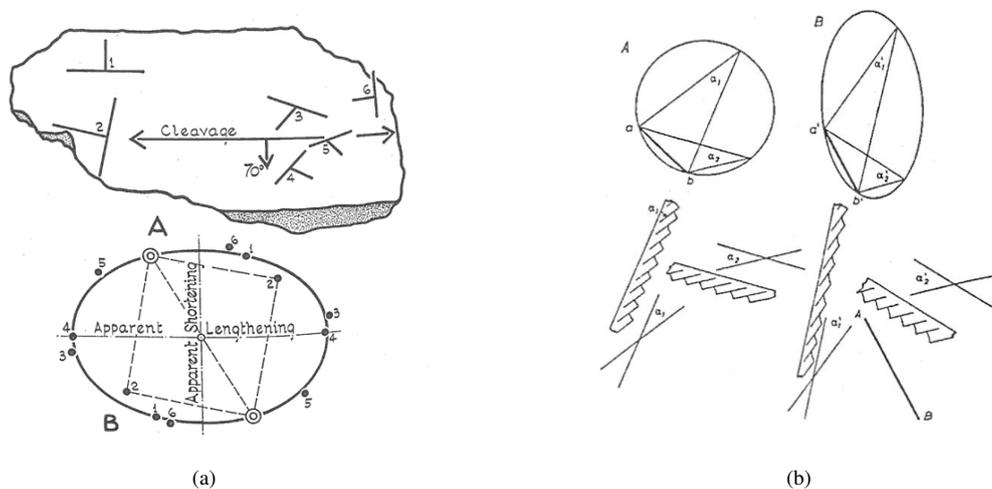


Figure 5.1: (a) Figure 1 from Wellman (1962) illustrating the application of the Wellman method to six deformed brachiopods exposed on a bedding surface. The hinge lines and symmetry lines of the fossils can be assumed to have been originally perpendicular. The method gives a strain ratio of 1.45, with the short axis perpendicular to cleavage. (b) Figure 5-69 from Ramsay (1967) showing the application of the method to graptolites, where the angles between two reference lines, the stipe and thecae, can be assumed to have been constant before deformation, but not necessarily perpendicular.

An analytical solution to the Wellman plot is given by Vollmer (2011b), and implemented here. To try the method, open the file Ragan 1985 F10-1a.png as an image. This image is from Ragan (1985), and is used in many structural geology classes as an exercise. Click on the digitizing icon and select the *Line Pair* icon, or use the menu command *Image - Digitize Image - Line Pair*. For each brachiopod click on the endpoints of each of the two lines, the hinge line and symmetry line. When done the lines appear in red, and the yellow cursor appears at the intersection. Mistakes can be corrected by using the *Cut* icon, or by deleting the line pair in the *Data* window.

The results reported in the *Log* window after digitizing all eight brachiopods are:

Wellman Ellipse Results

Ragan 1985 F10-1a

2022-05-15 16:18:32

=====

n = 8

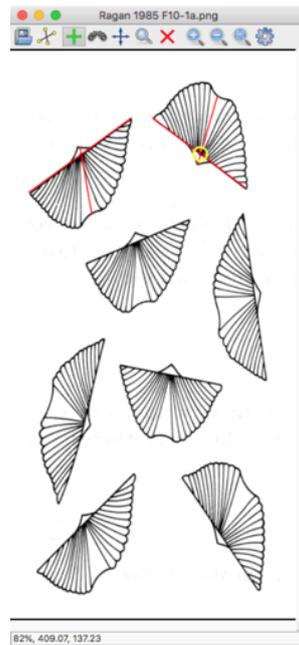


Figure 5.2: The *Image* window after opening the example data file Ragan 1985 F10-1a.png. The hinge and medial lines are assumed to have been initially perpendicular. Two line pairs have been digitized. Note that the *Line Pair* tool icon is selected.

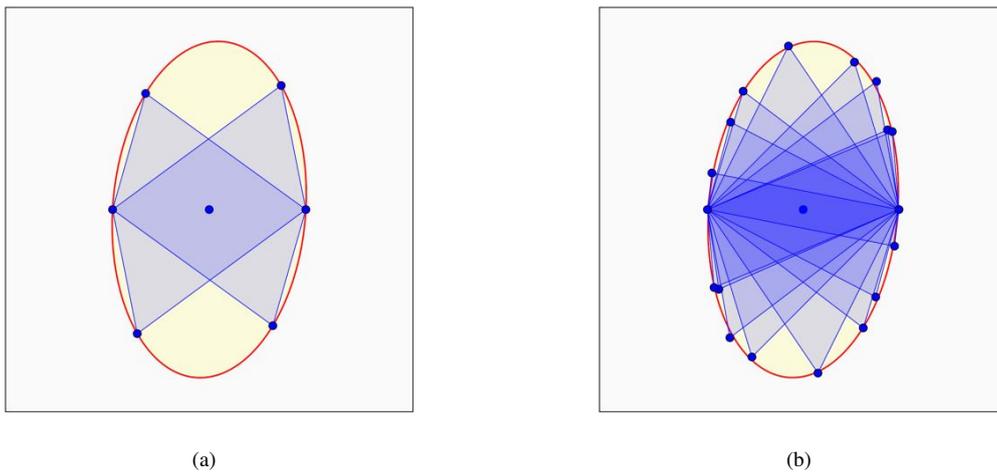


Figure 5.3: (a) Wellman plots of the brachiopod data digitized from image Ragan 1985 F10-1a.png. (a) Plot after digitizing two line pairs as shown in Figure 5.2. (b) Plot after digitizing all eight line pairs.

np = 18 fitted points

Ellipse

e1 = 0.773
 e2 = -0.015
 S1 = 1.773
 S2 = 0.985
 dA = 0.746
 R = 1.801
 ϕ = 95.16°
 np = 18

Root mean square

RMS = 0.039016

Sum squared errors

SSE = 0.027400

The ellipse-fitting calculation used is a least-squares technique minimizing the sum of the squares of the residuals of the points from an ellipse as described in Section 4.1, using Eq 4.6. The calculation includes the constriction line, so the ellipse has 9 point pairs including the 8 data points, and the number of fitted points is $n_p = 18$. The RMS (root mean square) is the square root of the average squared residuals from the fitted ellipse, and will be 0 for a perfect fit.

Graptolites that have an initially constant angle between stipe and thecae can be treated in a similar fashion (Ramsay, 1967; Ramsay and Huber, 1983), Figure 5.1b. This technique, however, requires identification of the graptolite species, as the initial angles between stipe and thecae varies by species. If available, initial thecae spacing from undeformed specimens can provide an absolute measure of strain (Goldstein et al., 1998).

Dirringer and Vollmer (2013) compared the Wellman method and the mean moment ellipse method (Section 6.1) using a sample of slate with deformed Ordovician graptolites. The sample was oriented with the slaty cleavage as the X axis. The stipe lines and thecae lines were digitized in 120 locations for the Wellman test, and the outlines of 31 whole graptolites and 38 partial graptolites were digitized for the polygon method test.



Figure 5.4: Sample of deformed graptoliferous slate used by Dirringer and Vollmer (2013) for comparison of the Wellman and mean moment ellipse methods.

The mean moment ellipse was $R = 2.079$, $\phi = 177.48^\circ$, parallel to the slaty cleavage. The moment ellipse method does not require assumptions about the initial geometry, which varies by species, but does require that they were initially randomly oriented. Interpreting the data for the Wellman method was problematic, as it resulted in many outliers. Removal of outliers, believed to be due to initial variations in thecae angle, was attempted, but deemed overly subjective, and the removal of single outliers significantly effected the result. They concluded that the necessary assumptions about initial geometry for the Wellman method were not met, and the polygonal shape method, which requires initially random orientations, but no assumptions about initial geometry, was preferred.



Figure 5.5: The graptoliferous slate sample of Figure 24 after retrodeforming to remove the strain calculated by the mean moment ellipse method, $R = 2.079$, $\phi = 177.48^\circ$

5.2 Line Stretch Analysis

A line stretch analysis is used for lines of known initial lengths, (L_i), final lengths, L_f , and final orientations, α_f . Folds and boudins are common examples of this type of data, where initial lengths can be measured along folded layers, or boudin segments (Ramsay, 1967; Mitra, 1978; Hossain, 1979; Ramsay and Huber, 1983; Lloyd and Ferguson, 1989). A minimum of three lines are required, ideally at high angles to one another.

The analytical approach taken here is to use the line stretches, $S = L_f/L_i$, as ellipse radii with orientations α_f , to construct diametrically opposed point pairs. As in Sections 4.1 and 5.1, the ellipse-fitting calculation used is a least-squares method minimizing the sum of the squares of the residuals of the points from the ellipse, using Eq 4.6. The RMS (root mean square) value is the square root of the average of the squared residuals of the data from the fitted ellipse, ranges from 0 to 1, and will be 0 for a perfect fit.

Stretched belemnites found in the Swiss Alps are classic examples of fossils suitable for strain analysis, having been reported as early as 1853 by Arnold Escher von der Linth (Letsch, 2016), Figure 5.6. An example analysis is done using three belemnites from Leytron, Valais, Switzerland (Ramsay and Huber, 1983, Figure 6.8). The data file, Ramsay and Huber 1983 F6-8, in the Example Data/Lines/Stretch folder, contains the initial lengths, L_i , final lengths, L_f , and orientations, α_f , of the three belemnites. See Lloyd and Ferguson (1989) for a discussion of methods for measuring these parameters. Figure 5.7 shows the strain ellipse derived from a stretch plot, with a unit circle superimposed, indicating a considerable positive dilation.

The results reported in the *Log* window after calling *Data - Calculate Stretch* are:

```
Stretch Ellipse Results
Ramsay and Huber 1983 F6-8
2022-05-15 16:26:17
```

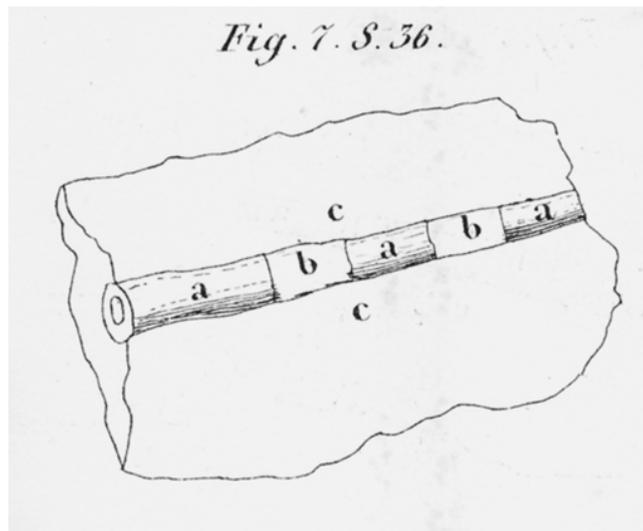


Figure 5.6: Sketch by Arnold Escher von der Linth (1853) of a stretched belemnite in the Uri Alps, Switzerland (Letsch, 2016). The recognition of such tectonic, or *mechanical*, deformation was important in the development of early orogenic theories.

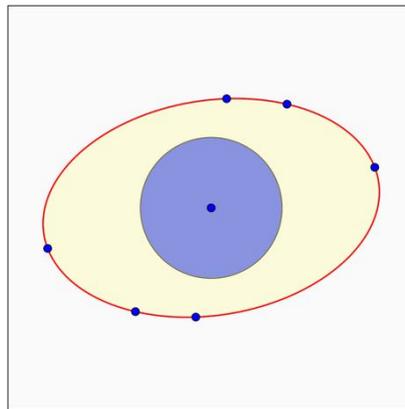


Figure 5.7: Stretch plot of the Leytron, Valais, Switzerland, belemnite data given in Ramsay and Huber 1983 F6-8.csv, from Figure 6.8 of Ramsay and Huber (1983). A unit circle is shown in blue, which indicates a large positive dilation.

```

=====
n      = 3
np    = 6 fitted points
Ellipse
  e1    = 1.390
  e2    = 0.523
  S1    = 2.390
  S2    = 1.523
  dA    = 2.638
  R     = 1.570
  φ     = 170.83°
  np    = 6
Root mean square
  RMS   = 0.000000
Sum squared errors
  SSE   = 0.000000

```

These results compare favorably with the strain calculated by Ramsay and Huber (1983) using a Mohr circle for finite strain (p. 104). Their construction gives $S_1 = 2.36$, $S_2 = 1.54$, $\Delta_A = 2.64$, $R = 1.53$, and $\phi = 170^\circ$.

5.3 Apparent Dip Analysis

The calculation of true dip from two apparent dips is a standard calculation in structural geology. Each apparent dip is a line defined by the intersection of a plane of interest and a plane of exposure, this line is called a *trace* of the plane. As each trace is contained in the plane of interest, two nonparallel traces define the plane, as shown in Figure 5.8. This is easily extended to multiple exposures each containing multiple traces.

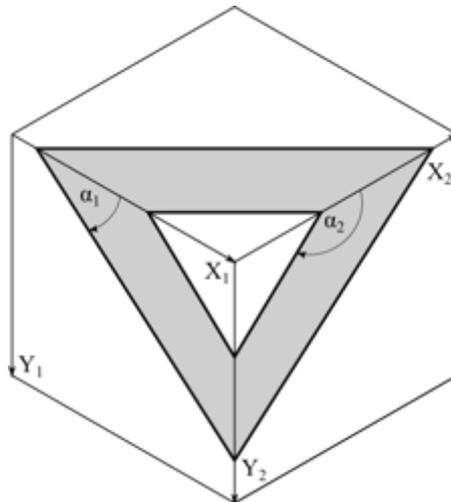


Figure 5.8: Example of a planar feature intersecting three planar exposures. Each intersection is referred to as a *trace* of the plane. As each trace is contained in the plane, two or more nonparallel traces can be used to define the plane of interest. A total of six traces, defining two parallel planes, are shown here. α_1 and α_2 are the pitches of traces for two section faces, as measured from X_1 and X_2 respectively. After digitizing, the traces in each section must be rotated to their original orientation using the software package Orient.

Given a set of sample faces for fabric analysis, typically three near-perpendicular sections, it may be of interest to define the orientations of penetrative features such as fractures or pressure solution seams, which may give information about the deformation mechanisms in operation when the fabric was formed. These may be quantified by the following procedure.

For each of the sections use the *Image - Digitize Image - Line* to create a file of the trace orientations. As the coordinate system of the image is vertical, with *X* right and *Y* down, the traces will have trends equal to the strike of the section, and plunges equal to the pitch. They will therefore need to be rotated about the section strike to restore their orientation in three dimensions. Open the file in a spreadsheet application and make the following changes:

1. Change the header "Alpha1" to "Plunge".
2. Change "Lf" to "Weight" (optional, needed if using line length to weight the result).
3. Change "X" and "Y" to "X0" and "Y0" (optional, these are not used).
4. Add a "Trend" header, and enter the strike of the section for all the traces.

The traces are now oriented in a vertical plane parallel to the section strike, and must be rotated to restore the dip. Open each section data file in Orient, and use the *Data - Rotate Data* command to rotate the data about a *Custom* axis. Enter the section strike, using the right hand rule, for the axis *Trend*, and 0 for the *Plunge*. Enter the negative complement of the dip, $\delta - 90^\circ$, as the *Angle*, press *Apply* and *Close*. This will restore the vertical image of the section to its original orientation. Save each of the rotated section data files in Orient.

Next, copy each of the rotated Orient data files into a new spreadsheet, removing all except the first header. Open the new file in Orient and determine the plane perpendicular to the minimum eigenvector of the trace orientation matrix, Figure 5.9, which is the best estimate of the plane of interest. Example files for this calculation are given in the Example Data/Lines/Apparent dip/Ordovician slate folder.

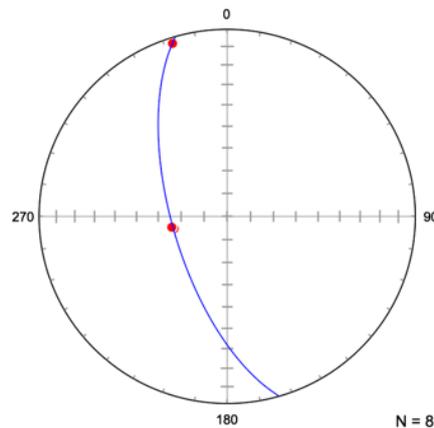


Figure 5.9: Schmidt plot of an example analysis using files given in the Example Data/Lines/Apparent dip/Ordovician slate folder. Four traces were measured in each of two sections, and rotated to their original orientations using the software Orient. The best-fit plane passing through the traces is calculated as the plane perpendicular to the minimum eigenvector of the orientation tensor.

6 Ellipse and Shape Analysis

This chapter covers methods for displaying and analyzing fabric ellipse data derived from particle ellipses and shapes. Some particles, such as pebbles, oöids (Figure 6.1), and reduction spots (Figure 6.2), can be closely approximated by ellipses. The analysis of samples of elliptical shapes is well established, forming a foundation of strain and fabric analysis (Ramsay, 1967; Dunnet, 1969; Elliott, 1970; Shimamoto and Ikeda, 1976; Ramsay and Huber, 1983).

However, the shape of deformed pebbles or cobbles often departs strongly from elliptical (Figure 7.3), and many particles are angular or irregular in shape (Figure 2.1a). For this reason, the concept that arbitrary shapes can be transformed into *moment ellipses*, is introduced. This means that irregular shapes can be analyzed using techniques previously developed for ellipses.

Plots of ellipse data are essential for evaluating fabric data, the commonly used R_f/ϕ and Elliott polar plots can be shown to be types of *hyperboloidal projections*, which has implications for understanding their properties. Other hyperboloidal plots, notably the *equal-area fabric plot*, have important properties useful for fabric analysis. Contouring data on these plots allows examination of fabric samples for outliers, multiple modes, and asymmetries. The fundamental topics of mean ellipse calculation and error analysis are also covered.

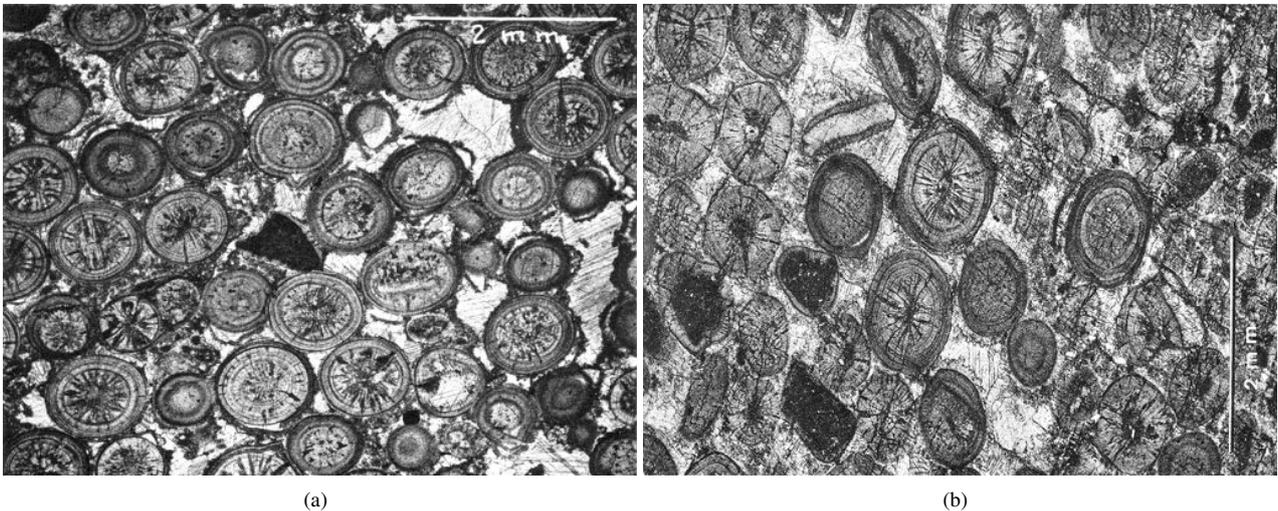


Figure 6.1: Oöids can make excellent strain markers due to their initially spherical forms. Shown here are oöids with spherulitic cores viewed in thin section, with a matrix of calcite and some mud. An important consideration is potential strain partitioning, as the strain reflected in the particles may not be identical to the strain of the entire rock. Samples from near Harrisonburg, Virginia (Cloos, 1971, Plates 9 and 11). (a) Nearly undeformed examples, with an average axial ratio of 1.16. (b) Deformed specimens with an average axial ratio of 1.56.



Figure 6.2: Examples of reduction spots, which potentially form ideal strain markers. (a) Reduction spots in the Bright Angel Formation, South Kaibab Trail, Grand Canyon National Park, Arizona. The red color of the mudstone is due to oxidized iron. The center of each spot contains a small amount of carbonaceous material, causing a spherical volume with iron in the reduced state. (b) Reduction spot in red slate, Cedar Point quarry, Vermont. Ellipsoidal reduction spots are often assumed to have been spherical in undeformed rock, however, an alternative hypothesis is that they form *after* deformation, and reflect the post-deformation anisotropy caused by cleavage (Fossen, 2016, p. 61). This emphasizes the importance of stating all assumptions when doing a strain analysis. Photographs by F.W. Vollmer.

6.1 Moment Ellipses

Numerous techniques for the analysis of populations of ellipses for fabric and strain analysis have been developed, as have more specialized methods for deformed fossils and other objects of known initial geometries (Ramsay, 1967; Ramsay and Huber, 1983). It can be shown, however, that ellipse methods can be extended to arbitrarily shapes by using ellipses that have the same moments (Mulchrone and Choudhury, 2004; Yamaji, 2013; Yamaji and Maeda, 2013), such ellipses are referred to here as *moment ellipses*. This allows randomly oriented objects of *any* initial shape to be used in strain analysis, thus extending ellipse techniques to all objects.

The calculation of moment ellipses is done in two ways. First, the *Shape* digitizing option allows direct digitizing of shapes, which are converted into ellipses (Section 2.2.6). The polygonal shapes can be in as much detail as desired. When converted to ellipses, they will have the same area, centroid, and three second order moments of inertia, as the polygonal shapes. Note that this is *not* the same as least-squares best-fit ellipses, which give incorrect results for irregular particles (McNaught, 1994). Also, least-squares ellipses are not defined for less than five points, while moment ellipses are defined for triangles and quadrilaterals.

Second, the *Filled Shape* digitizing option uses pixel summation to calculate moment ellipses (Section 2.2.7). Each pixel can be considered a point mass, and adjacent pixels are summed until a bounding edge is reached. This method generally requires tracing a black border of each particle onto a white layer using image editing software such as Adobe Photoshop or GIMP (Figure 2.1b). Similar pixel summation routines are implemented in ImageJ and MATLAB.

6.2 Ellipse Plots

In order to evaluate a sample of fabric ellipses prior to further analysis, it is important to plot the data in a way that can identify outliers, modes, and asymmetries. Such a plot is an exploratory evaluation of the density distribution of the data to determine if it can be characterized statistically by a mean and confidence interval, or if it represents a more complex distribution. The R_f/ϕ plot (Ramsay, 1967; Dunnet, 1969) and Elliott polar plot (Elliott, 1970) are standard plots for ellipse data. It can be shown that these are both equidistant hyperboloidal projections, and that other hyperboloidal projections,

such as the *equal-area fabric plot* (Section 6.3.1), have useful properties for strain analysis.

6.2.1 Elliott Polar Plot

The Elliott polar plot (Elliott, 1970) is a polar plot of the natural logarithm of the ellipse ratios, $\ln R_i$, versus twice the orientations of their long axes, $2\phi_i$. As discussed in Section 6.2.3, this logarithmic plot is an *equidistant azimuthal* hyperboloidal projection (Yamaji, 2008; Vollmer, 2018b). While all projections have inherent distortion, this plot does not distort strain magnitude radially from the center (similar to an equidistant spherical projection), and provides a better representation of the data density distribution than the R_f/ϕ plot described in Section 6.2.2. However, the Elliott plot does distort area, unlike the equal-area fabric plot described in Section 6.3.1, which provides a better representation of the density distribution.

Figure 6.3a is an Elliott polar plot of the data digitized from the oolite photomicrograph in Figure 3.6. The ellipse mean (Section 6.5) is plotted as a red circle, and the data has been contoured at 20% of the density distribution (Section 6.3). When in *Find* mode, points can be selected and the selection will automatically update on other plots and in the *Data* window. To illustrate the utility of this for detecting data outliers, Figure 6.3b shows a normalized Fry plot with the points generated by the outlier selected in Figure 6.3a. This outlier falls well inside the central void on the normalized Fry plot, probably does not meet the assumptions necessary for a Fry analysis, and could reasonably be discarded.

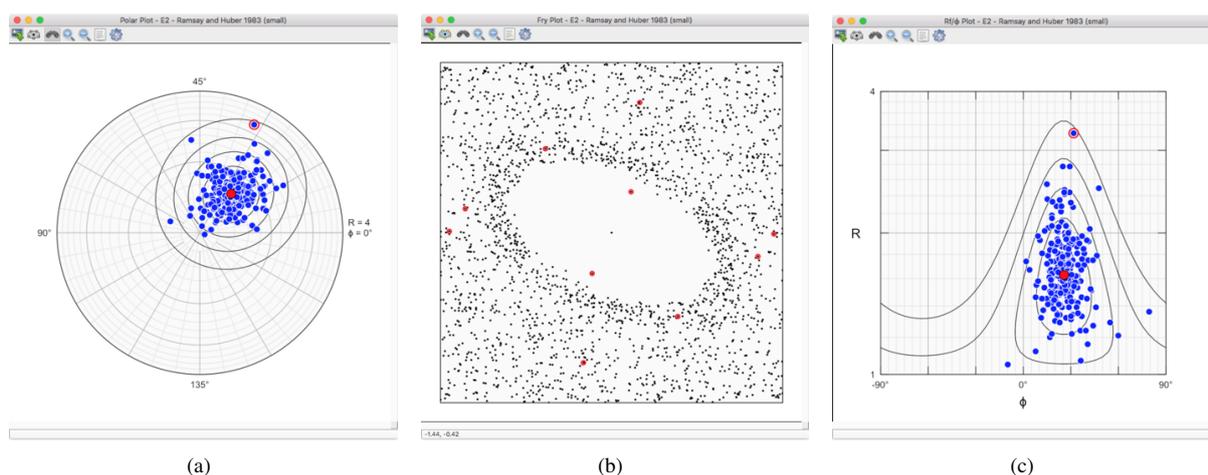


Figure 6.3: Fabric plots of the data from the oolite photomicrograph in Figure 3.6. In a and c, the mean (Section 6.5) is shown as a red circle, and the data has been contoured at 20% of the density distribution (Section 6.3). One potential outlier is selected. (a) Elliott polar plot. R is undistorted radially from the center, as it is an equidistant azimuthal projection. (b) Normalized Fry plot. (c) $\ln R_f/\phi$ plot. Distortion is apparent as increased horizontal stretching as R approaches 1, as it is an equidistant cylindrical projection, analogous to a Mercator projection.

6.2.2 R_f/ϕ Plot

The R_f/ϕ plot (Ramsay, 1967; Dunnet, 1969) is a Cartesian plot of R_f , or more commonly the natural logarithm, $\ln R_f$, versus ϕ (Figure 6.3c), and is widely used in strain analysis (Ramsay and Huber, 1983; Lisle, 1985). Although the original plot had R_f as the ordinate, it has been presented with either variable as the ordinate. This plot is probably more widely recognized and used than the Elliott polar plot, but has much greater distortion, especially at low strains, because R and ϕ are not independent parameters.

The logarithmic $\ln R_f/\phi$ plot is an *equidistant cylindrical* hyperboloidal projection (Vollmer, 2018b), and the linear version of the R_f/ϕ plot is an *exponential cylindrical* hyperboloidal projection. As progressive strain is more naturally represented on a logarithmic plot, the linear version is rarely used, however, it is important to stipulate which version of the plot is being used.

The $\ln R_f/\phi$ plot distorts the fabric density distribution strongly, especially at low strains (Vollmer, 2011a, 2018b). By analogy, a Mercator projection of the Earth projects the North and South Poles as lines rather than points, causing extreme distortion in polar regions, Greenland appears larger than South America on such a map, although it is one eighth the size (Snyder, 1987). Similarly, R_f/ϕ plots project the unit circle ($R_f = 1$) as a line instead of a point, causing extreme distortion at low strains.

6.2.3 Hyperbolic Plots

The unit hyperboloid, H^2 , is the natural parameter space for ellipse data. In this space, the difference between two strains is an angular distance, d_H , and strain is a *rotation* following a geodesic. d_H , the *hyperbolic distance*, is a better measure of the difference between two ellipses than the differences between their respective R and ϕ values, since the magnitude of ϕ at $R \approx 1$ has little significance.

Additionally, the hyperbolic vector mean is the best-fit strain (Yamaji, 2008). Hyperboloidal projections are therefore useful for plotting fabric ellipse data (Reynolds, 1993; Yamaji, 2008, 2013; Vollmer, 2018b). By analogy, the natural parameter space for directional data is the sphere, S^2 , and spherical projections are used to plot directional data (Schmidt, 1925; Fisher et al., 1987; Vollmer, 1995). The two most commonly used fabric plots can be shown to be hyperboloidal projections, the Elliott polar plot is an *azimuthal equidistant* projection (Yamaji, 2008), and the $\ln R_f/\phi$ plot is a *cylindrical equidistant* projection (Vollmer, 2018b).

Figure 6.4a shows the unit hyperboloid, H^2 , with Cartesian axes, x_0, x_1, x_2 , and point $C = [1, 0, 0]^T$, which corresponds to the circle $R = 1$. The plane x_1x_2 is the projection plane for *azimuthal* projections, such as the Elliott polar plot. Figure 6.4b illustrates the geometry of hyperbolic *cylindrical* projections, including the $\ln R_f/\phi$ plot, on which points are projected from H^2 onto a cylinder, which is then unwrapped to form a Cartesian plot (Vollmer, 2018b).

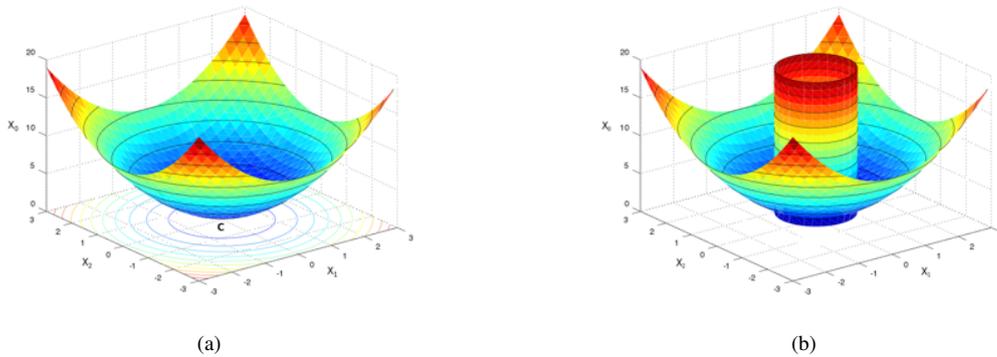


Figure 6.4: The unit hyperboloid, H^2 , showing cartesian axes, x_0, x_1, x_2 , and point $C = [1, 0, 0]^T$, which corresponds to the circle $R = 1$. From Vollmer (2018b). (a) The plane x_1x_2 is the projection plane for azimuthal projections, such as the Elliott polar plot. (b) H^2 with superimposed cylinder with axis $x_0 \geq 1$. The cylinder is the projection surface for cylindrical projections, such as the R_f/ϕ plot.

As is the case for spherical projections, there are numerous hyperboloidal projections, each of which has different properties. Figure 6.5 shows three such projections, the azimuthal equidistant projection (Elliott polar plot) which preserves distance ($\ln R$) radially, the equal-area projection which preserves area (Section 6.3.1), and the stereographic projection which preserves angles. As the stereographic projection preserves angles, contours on an initially isotropic fabric remain circular with strain (Vollmer, 2018b, Figure 6.5c).

Cylindrical plots, such as the cylindrical equidistant projection ($\ln R_f/\phi$ plot), are highly distorted at low values of R , where the magnitude of ϕ has little significance, because R and ϕ are not independent. Figure 6.6 shows three such plots, equidistant cylindrical ($\ln R_f/\phi$), exponential (linear R_f/ϕ), and radial (Vollmer, 2018b).

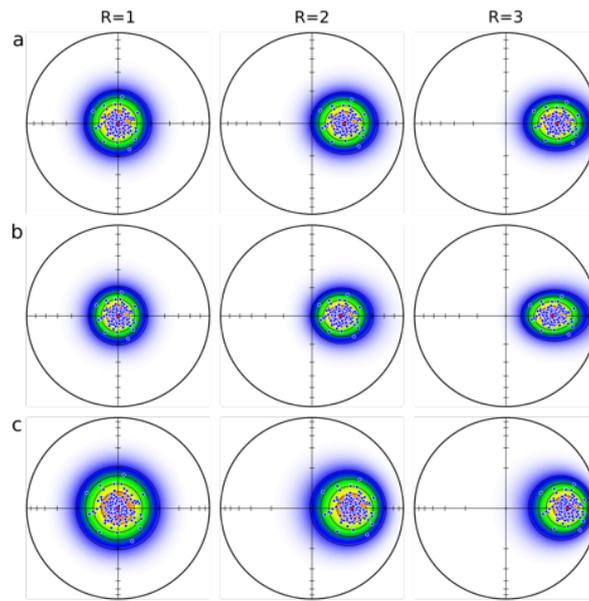


Figure 6.5: Synthetic data of 200 ellipses strained to values of $R = 2$ and $R = 3$ displayed on hyperboloidal azimuthal projections. (a) equidistant (Elliott), (b) equal-area, and (c) stereographic. From Vollmer (2018b).

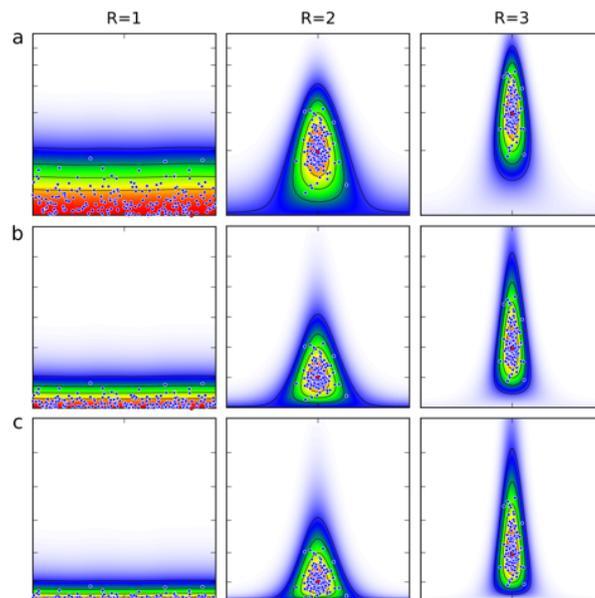


Figure 6.6: Synthetic data of 200 ellipses displayed on hyperboloidal cylindrical projections. (a) equidistant cylindrical ($\ln R_f/\phi$) (b) exponential (linear R_f/ϕ), and (c) radial. From Vollmer (2018b).

6.2.4 Cloos Plot

Ernst Cloos' work (Cloos, 1947, 1971) on the deformation of oolites associated with the South Mountain anticline in the Appalachian Mountains was foundational in detailed regional strain analysis. Cloos used oriented thin sections (Figure 6.1), using cleavage and lineations as reference directions, to determine strain ellipsoid axial ratios and orientations. This data was presented on maps (Figure 6.7), Schmidt plots, and axial ratio ($C/A = \text{Min}/\text{Max}$) plots (Cloos, 1971, Figures 14 and 15). The *Cloos Plot* command produces similar plots (Figure 6.8). The plot includes a best fit solution for the ratio (shown in red), which is reported in the *Log* window. This is not, however, the best estimate of the mean fabric ellipse, which should be calculated separately (Section 6.5).

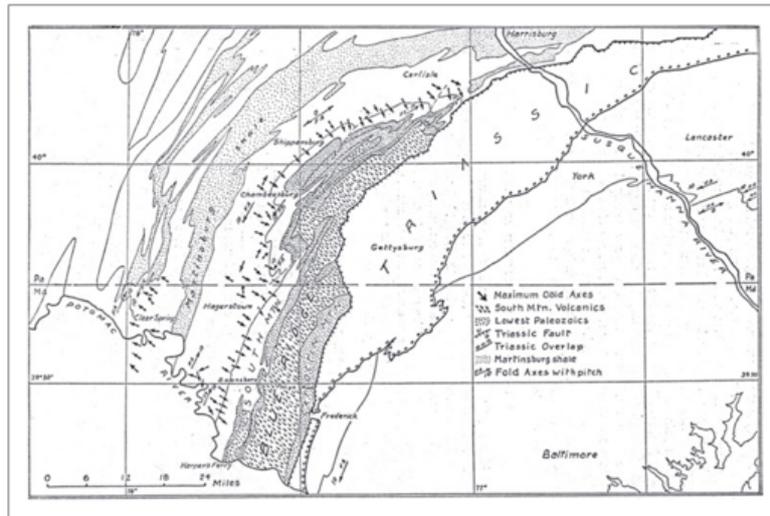


Figure 6.7: Map of oolite outcrops along the South Mountain anticline in the Appalachian Mountains with directions of long axes (Cloos, 1971). Ernst Cloos' work (Cloos, 1947, 1971) was foundational in regional strain analysis.

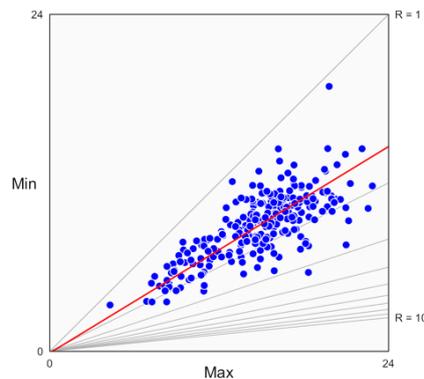


Figure 6.8: Cloos plot of axial ratios from deformed oolite digitized from Ramsay and Huber (1983). The red line is the least squares best fit solution, which is reported in the *Log* window, note, however, that it is not the best estimate of the mean fabric ellipse (Section 6.5).

6.3 Contouring Fabric Data

Fabric plots are used to evaluate a sample of fabric ellipses prior to further analysis, so it is important to plot the data in such a way that can identify outliers, modes, and asymmetries. Such a plot is an exploratory evaluation of the density distribution of the data to determine if it can be characterized statistically by a mean and confidence interval, or if it represents a more complex distribution (Elliott, 1970).

Orientation data, common in geology, is generally plotted on Schmidt plots, and contoured to examine the density distribution for outliers and asymmetries (Schmidt, 1925; Kamb, 1959; Fisher et al., 1987; Vollmer, 1995). Similarly, it is desirable to have a contouring method for fabric data for preliminary analysis of modes and asymmetries. Vollmer (2018b) gives an algorithm for the automatic contouring of fabric and data on the unit hyperboloid (Figures 6.3, 6.5, and 6.6). Density calculations are made on the hyperboloid at the nodes of a back-projected grid, which is then contoured. This is analogous to the commonly used modified Kamb contouring (Vollmer, 1995), however density calculations are made on the hyperboloid rather than on the sphere.

The contours represent the density distribution on the hyperboloid, which is contoured as levels of the maximum density. For example, 5 levels gives contours at 20%, 40%, 60%, and 80% of the maximum density. Additional options include the number of grid nodes, 50 is the default, 100 may be more suitable for high resolution figures for publication. A weighting factor, κ , based on the cumulative distribution function for a unit hyperboloid, controls smoothing of the contours, the default is 40 (Vollmer, 2018b).

Contouring can be done on any of the hyperboloidal plots, including the Elliott and $\ln R_f/\phi$ plots. These two plots are the most common in the geological literature, however the *equal-area fabric plot* (Section 6.3.1) gives an unbiased representation of the density distribution (Yamaji, 2013; Vollmer, 2018b), and is recommended, for example, when trying to identify asymmetries or multiple modes in the data. By analogy with spherical projections, an equal-area (Schmidt) plot is preferred when examining the data density of directional data.

6.3.1 Equal-Area Fabric Plot

As noted in Section 6.2, fabric plots provide an exploratory evaluation of the density distribution of the data to determine if it can be characterized statistically by a mean and confidence interval, or if it represents a more complex distribution. The evaluation of the density distribution, therefore, should be done on a plot that minimizes density distortion. For the same reason, geologic orientation data are generally displayed on Schmidt plots that use the equal-area projection, and not using a stereonet which uses the stereographic (equal angle) projection.

The hyperboloidal azimuthal equal-area plot, or *equal-area fabric plot*, is a plot that preserves area and is therefore suitable for examining density distributions of fabric data for outliers, modes, and anisotropy (Yamaji, 2008, 2013; Vollmer, 2018b). Figure 6.9 shows three data samples that illustrate how contouring on equal-area fabric plots can highlight anisotropies. Each sample is first transformed so the mean lies at the center of the plot, at $R = 1$ (Section 6.7), and then contoured. Deviations of the contours from circularity are then readily apparent.

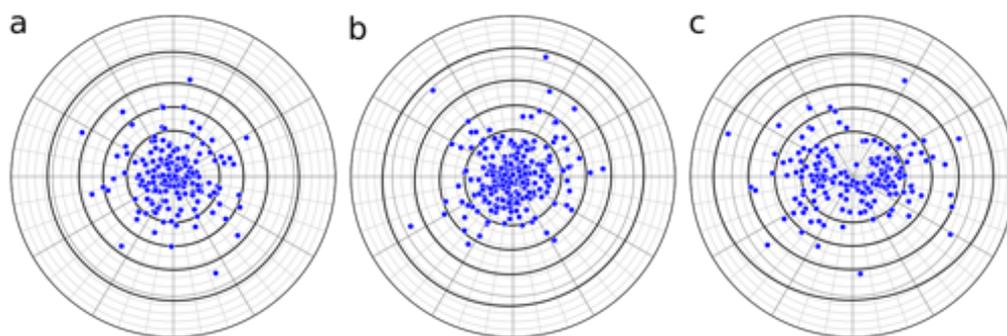


Figure 6.9: Contoured *equal-area* fabric plots of data samples retrodeformed so the mean lies at $R = 1$, to illustrate sample anisotropy. (a) Nearly isotropic synthetic fabric. The anisotropy index (Section 6.4) is $I_a = 0.139$. (b) Oolite data shown in Figure 3.6. The contours deviate little from circularity, suggesting an approximately isotropic initial fabric. $I_a = 0.333$. (c) Synthetic bimodal fabric. The ovoid shapes of the contours confirm it is not an isotropic fabric. This stronger anisotropy gives $I_a = 0.668$. From Vollmer (2018b).

6.4 Fabric Anisotropy

The equal-area fabric plot is a useful tool for examining fabric data for outliers, modes, and asymmetries, however it is also useful to have a numerical measure of anisotropy. Vollmer (2018b) proposed an anisotropy index, I_a , based on the moments of the distribution about the hyperboloid axis x_0 (Figure 6.4a):

$$I_a = 1 - (\varepsilon_2/\varepsilon_1) \quad (6.1)$$

where ε_1 and ε_2 are the maximum and minimum eigenvalues of the matrix Q calculated from the $[x_1, x_2]$ coordinates of n points. Taking $q_i = [x_{1i}, x_{2i}]^T$

$$Q = \frac{1}{n} \sum_{i=1}^n q_i q_i^T \quad (6.2)$$

I_a will equal 0 for a distribution perfectly isotropic about the x_0 axis, and increases to 1 with anisotropy. The *Data / Calculate Ellipse* dialog box has an option to calculate the anisotropy index.

The index increases with strain, and is meant to be calculated on pre-strain fabrics, so strained samples should be retrodeformed using the method outlined in Section 6.7. Note that this method removes the mean final fabric ellipse, which may include sedimentary fabrics and compaction. A high anisotropy index suggests an initial anisotropic fabric, or anisotropic strain, and the sample should be regarded as suspect. Figure 6.9 shows samples with varying anisotropy indexes, on equal-area fabric plots. Vollmer (2018b) suggests that values of $I_a \geq 0.5$ be provisionally marked for reevaluation.

6.5 Mean Ellipse Calculation

Determination of the best-fit, or mean, ellipse from a sample of fabric ellipses is of considerable importance for geological strain analysis and numerous graphical and mathematical techniques have been proposed, including various arithmetic means, ellipse plot centroids, and fitting of $\ln R_f/\phi$ data to theoretical curves (Ramsay, 1967; Ramsay and Huber, 1983; Lisle, 1985). The most rigorous approach, however, is a direct numerical calculation of the mean (Shimamoto and Ikeda, 1976; Mulchrone et al., 2003; Yamaji, 2008).

Selecting multiple rows in the data window that contain $[R, \phi]$ data, will calculate the mean of those rows, and display it in the status bar. If two rows are selected that contain $[R, \phi]$ data, the hyperbolic distance, d_H , (Section 6.2.3) between the two is also displayed.

6.5.1 Simple Means and Centroids

The *Centroids* and *Simple means* options give approximations less accurate than the true mean, and are provided for comparison only. This includes vector, arithmetic, and harmonic means. The centroids of the polar, R_f/ϕ , and other hyperboloidal plots can also be calculated and plotted for comparison, but should not be confused with the true mean.

In particular, the centroid of the Elliott polar plot has been suggested to be equal to the mean (Lisle, 2010), however, it is not equal to the true mean, and the error increases with strain (Holst, 1982). The centroid of the hyperboloidal stereographic projection is a better estimate, but is still approximate. The centroid of the $\ln R_f/\phi$ plot is not a reliable estimate, and can deviate significantly from the true mean Vollmer (2018b).

Graphical techniques using R_f/ϕ plots have been commonly used to estimate the fabric mean by identifying maxima on the plot, or by comparing plots to *reference curves* drawn for different values of strain (Ramsay and Huber, 1983; Lisle, 1985). However numerical methods are now fast and readily available, making graphical estimation unnecessary.

6.5.2 Shape Matrix Eigenvector

Shimamoto and Ikeda (1976) devised a numerical solution to calculate a mean ellipse involving the determination of the eigenvectors of the mean *shape matrix*, sometimes referred to as the *inverse shape matrix* (Wheeler, 1986; Robin, 2002), a symmetric two by two matrix representing an ellipse, formed by summing the components of particle ellipses, normalizing the matrix, and computing the eigenvectors to give the mean ellipse.

The general equation for an ellipse centered at the origin can be written

$$b_{11}x_1^2 + b_{22}x_2^2 + 2b_{12}x_1x_2 = 1 \quad (6.3)$$

or in matrix form

$$x^T b x = 1 \quad (6.4)$$

where b is the shape matrix, and x are the coordinates defining the ellipse. In expanded form

$$\begin{bmatrix} x_1 & x_2 \end{bmatrix} \begin{bmatrix} b_{11} & b_{12} \\ b_{12} & b_{22} \end{bmatrix} \begin{bmatrix} x_1 \\ x_2 \end{bmatrix} = 1$$

after normalizing to a unit area by using the axial ratio R , since the size of the ellipse is not considered, b is

$$\begin{aligned} b_{11} &= (1/R) \cos^2 \phi + R \sin^2 \phi \\ b_{22} &= (1/R) \sin^2 \phi + R \cos^2 \phi \\ b_{12} &= (1/R - R) \sin \phi \cos \phi \end{aligned}$$

which expresses it as a rotation, ϕ , of a unit ellipse with axes parallel to the coordinate axes.

A mean ellipse can then be found for a sample of n ellipses by forming the mean shape matrix

$$\bar{b} = \frac{1}{n} \sum_{i=1}^n b_i \quad (6.5)$$

The principal axes and their orientations are found by taking the eigenvectors of the mean shape matrix, which can be determined algebraically from a quadratic equation (Davis, 1986, p. 126-139). The two eigenvalues, λ , give the principal axes, $S = 1/\sqrt{\lambda}$. Shimamoto and Ikeda (1976) extend this method to three-dimensional ellipsoids, but more general approaches have since been devised (Section 7.3).

6.5.3 Mean Radial Length

Mulchrone et al. (2003) devised an alternative mean ellipse calculation that determines the *mean radial length* (MRL). This calculation does not require eigenvector calculation, potentially giving an advantage. However, the eigenvectors this case can be determined algebraically from a quadratic equation (Section 6.5.2), so the MRL calculation does not necessarily offer an advantage over the shape matrix mean in simplicity of implementation or processing speed.

6.5.4 Hyperbolic Vector Mean

Yamaji (2008) showed that using non-Euclidian hyperbolic geometry, the mean is calculated simply as the hyperbolic vector mean. This provides an elegant mathematical solution which illustrates the simplicity and utility of the hyperboloid model in understanding strain transformations and projections. In terms of programing, the algorithm is simple, but requires transformations to and from hyperboloidal coordinates.

6.5.5 Comparison of Mean Calculations

When calculating the mean ellipse using the *Calculate Ellipse* command, the method can be selected among *Eigenvector*, *Mean radial length*, and *Hyperbolic mean* options. These three methods are mathematically equivalent, and have been verified computationally to give identical results (Vollmer, 2010), so only one need be selected. The shape matrix eigenvector method (Shimamoto and Ikeda, 1976) is the default, as it is marginally faster. The speed differential between the three methods is small, and is only important during bootstrap analysis (Section 6.6), when thousands of such calculations are required. The simple means and centroids are only provided for comparison, as they are approximations of the mean.

Table 6.1 compares results for the three numerical methods. As the methods are mathematically equivalent, these tests were done to verify that, and to insure that the methods were all implemented correctly. The calculated means are identical to numerical precision for all three methods, confirming correct implementation.

Data Set	Imposed R, ϕ	Eigenvector	MRL	Hyperbolic
Oolith, n = 252	1, 0	1.628, 25.74	1.628, 25.74	1.628, 25.74
	0.614, 25.74	1.000, 113.32	1.000, 113.32	1.000, 113.32
Synth 1, n = 300	1, 0	1.031, 40.20	1.031, 40.20	1.031, 40.20
	2, 0	2.012, 1.16	2.012, 1.16	2.012, 1.16
	4, 0	4.023, 0.46	4.023, 0.46	4.023, 0.46
Synth 2, n = 1000	1, 0	1.016, 146.03	1.016, 146.03	1.016, 146.03
	2, 0	2.012, 179.46	2.012, 179.46	2.012, 179.46
	4, 0	4.024, 179.78	4.024, 179.78	4.024, 179.78

Table 6.1: Comparative results for ellipse-fitting calculations. *Eigenvector* - Shape matrix eigenvectors (Shimamoto and Ikeda, 1976). *MRL* - Mean radial length (Mulchrone et al., 2003). *Hyperbolic* - Hyperbolic vector mean (Yamaji, 2008). All three calculation give identical results. From Vollmer (2010).

6.6 Error Analysis

A calculation of the mean fabric ellipse should also include a measure of the confidence in that calculation. Error analysis is done by bootstrapping, a nonparametric method that requires no assumptions about the underlying distribution, and is applicable to small samples. It has the additional advantage of allowing the errors in section ellipses to be utilized in calculating confidence regions for three-dimensional ellipsoids. Bootstrap error for void-fitting methods is discussed in Section 3.3.7, and can also be utilized for determining confidence regions for fabric ellipsoids (Section 7.4.3).

As discussed in Section 3.3.7 for void-fitting methods, bootstrap error analysis (Efron, 1979) offers a powerful technique for calculating confidence regions. The technique is nonparametric, meaning that it is not necessary to assume the sample comes from a particular distribution, and it may be applied to small samples, less than 25 data points. Resamples of the sample are created by random resampling with replacement, and the mean is calculated of the resample. This is done thousands of times to create a sample of means. The dispersion in these means is used to determine confidence intervals (Figure 6.10).

Bootstrap error analysis is readily done for mean ellipse calculations (Section 6.5). While the resampling technique is straightforward, one question involves the choice of parameters to be used for the confidence intervals. That is, if R and ϕ are to be considered as independent parameters (Mulchrone et al., 2003), or if the hyperbolic distance, d_H (Section 6.2.3), is considered as a single parameter (Yamaji, 2008). For values of R near one, the value of ϕ is not well constrained, so the confidence interval for ϕ is dependent on R , suggesting that d_H is a better choice.

If the error in d_H is calculated, the errors in R and ϕ are derived from that, and are not calculated independently. When the bootstrap resample means are retrodeformed to the sample mean, the radial distance of a resample mean from the center of an equidistant (Elliott) polar plot represents the error in the bootstrap resample (Figure 6.10). Bootstrapping with the d_H option is the default option.

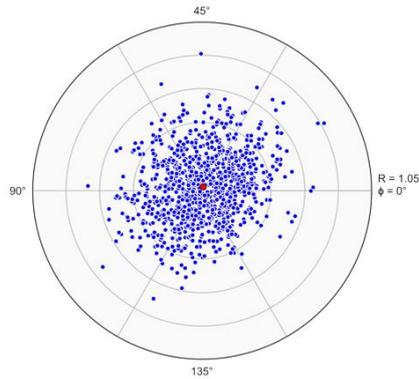


Figure 6.10: Example of error analysis shown on an equidistant (Elliott) polar fabric plot of the bootstrap means of 1000 resamples from the oolite data. The sample mean is rotated (retrodeformed) to C ($R = 1$). The red symbol is the mean of the bootstrap means, which can differ from the sample mean. The dispersion of the points is a measure of the error in the best-fit ellipse, from which confidence intervals are determined. The radial distance of each resample mean from the center represents the hyperbolic distance (Section 6.2.3) error used to calculate d_H 95%.

6.7 Data Transformation

The *Transform Data* dialog (Figure 6.11) allows sequential homogeneous coordinate transformations of the data, including applying a strain, unstraining (retrodeforming), shear, rotation, and translation. Transformations can be sequentially applied, and undone. Selecting *Accept* applies the transformation to the data set. Be sure to make a backup copy of your data file before transforming it!

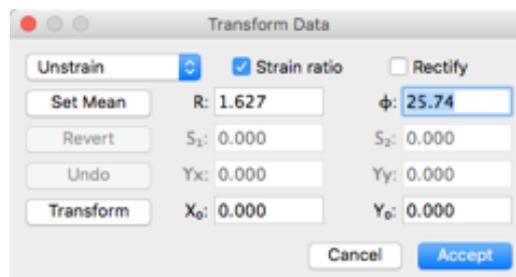


Figure 6.11: The *Transform Data* dialog which allows the sequential application of homogeneous coordinate transformations, strains, rotations or translations, to the data.

Data transformation is useful for the examination of fabric anisotropy as discussed in Section 6.3 and 6.4. For this type of analysis, select *Unstrain*, then *Set Mean*, *Transform*, and *Accept*. This calculates the mean strain and transforms the data to remove it, so potential anisotropies can be examined. The *Rectify* option is used to keep the data rectified to an image. See Section 3.1 for an example application.

6.8 Data Synthesis

The *Data - Synthesize Data* command allows the construction of synthetic data sets. The ellipse ratios, R , can be selected randomly within limits, or from a Gaussian distribution with a selected mean and standard deviation. The ellipse orientation, ϕ , can similarly be selected randomly within limits, or from a selected Von Mises distribution. The particle size can be constant with an area of π , or selected from a Gaussian distribution with a mean of π . The number of particles, n , is also variable.

The particle spacing is determined by a snowball packing algorithm that drops particles from a random position and looks for collisions, the number of iterations determines the number of tries before discarding a particle. Checking *Radial* gives a circular area, unchecking it results in a square area.

7 Fabric and Strain Ellipsoids

For regional strain studies it is generally desirable to determine the three-dimensional strain ellipsoid, whose axes are given by three principle stretches, S_k , and their orientations, commonly expressed as trends and plunges, $[t_k, p_k]$. The calculation can be simplified if assumptions can be made about the relationship between foliations and strain, for example, slaty cleavage is commonly assumed to be perpendicular to S_3 . However, in the general case it is necessary to determine the two-dimensional strain on a number of different planes through a hand sample or outcrop, and combine them to determine the strain ellipsoid in three dimensions. This also avoids user bias in the determination of strain axes in outcrop or hand sample. Calculation of an ellipsoid from section ellipses is an overdetermined mathematical problem, and numerous solutions have been proposed to calculate the optimal solution (Shimamoto and Ikeda, 1976; Owens, 1984; Robin, 2002; Shan, 2008; Mookerjee and Nickleach, 2011). The methods of Robin (2002) and Shan (2008) are implemented here (Section 7.3).

The following are some terms used here for ellipsoid calculation and error analysis. A *section* is one of, usually, three or more surfaces for which a fabric ellipse has been estimated, these are designated using the subscript j . A *section ellipse* is the best-fit ellipse for a section, typically derived by point distribution analysis (Section 3) or mean ellipse calculation (Section 6.5). The *section data* are the individual ellipses used to estimate the section ellipse, and are designated using the subscript ji . A *section ellipse resample* is a bootstrap resample of a section ellipse used for error analysis, while a *section data resample* is a bootstrap resample of the section data used to create a section ellipse resample. The term *resample* may be replaced by *simulation*, depending on the error analysis method. Note that for point distribution analysis, the section data are not normally available, however section data resamples may be (Section 3.3.7).

7.1 Ellipsoid Plots

A number of plots have been developed to display the shape of strain, or other, ellipsoids using their three principal axes. Such plots allow comparison of a measure of the magnitude of the strain, as well as a measure of the symmetry of the ellipsoid. The symmetry expresses variations in the relative ratios of the three axes, distinguishing, for example, prolate (cigar-shaped) versus oblate (pancake-shaped) ellipsoids.

Zingg (1935, p. 45-55) proposed a plot to describe the shapes of approximately ellipsoidal pebbles, using ratios B/A versus C/B ($1/R_{AB}$ versus $1/R_{BC}$), which range from 0 to 1. A related diagram for plotting strain ellipsoids was introduced by Flinn (1956), and modified by Ramsay (1967) for natural (logarithmic) strain. Hsu (1966), following Nadai (1963, p.70-76, cited in Hossack, 1968), introduced an alternative plot based on a projection of three-dimensional natural strain space to two dimensions, which was applied by Hossack (1968) for geologic strain analysis. An additional ellipsoid plot, useful for visualizing an individual ellipsoid is a projected *ellipsoid shade plot*.

Each of these plots is displayed in a separate window. The Flinn-Ramsay and Nadai-Hsu plots are interactive, selecting a point in one will automatically select the corresponding data point on the other plot, as well as in the *Data* window, and a shade plot.

7.1.1 Flinn-Ramsay Plot

A *Flinn plot* is a plot of the ratios R_{AB} versus R_{BC} , the natural logarithmic version of this plot, $\ln R_{AB}$ versus $\ln R_{BC}$, is known as a *Ramsay plot* (Ramsay, 1967; Ramsay and Huber, 1983). The latter is generally preferred for plotting geologic finite strain data due the applicability of natural (logarithmic) strain to progressive deformation, however both plots are used for displaying strain ellipsoid data.

Figure 7.1 compares Flinn and Ramsay plots of deformed conglomerate ellipsoids from the Bygdin area, Norway (Figure 7.3), data from Hossack (1968). The Flinn plot, Figure 7.1a, shows a stronger clustering at low strains, compared to the Ramsay plot, Figure 7.1b, which more readily allows discrimination among data points, especially at low strains. More significantly, the

logarithmic plot uses natural strain values, which are compatible with studies of progressive deformation.

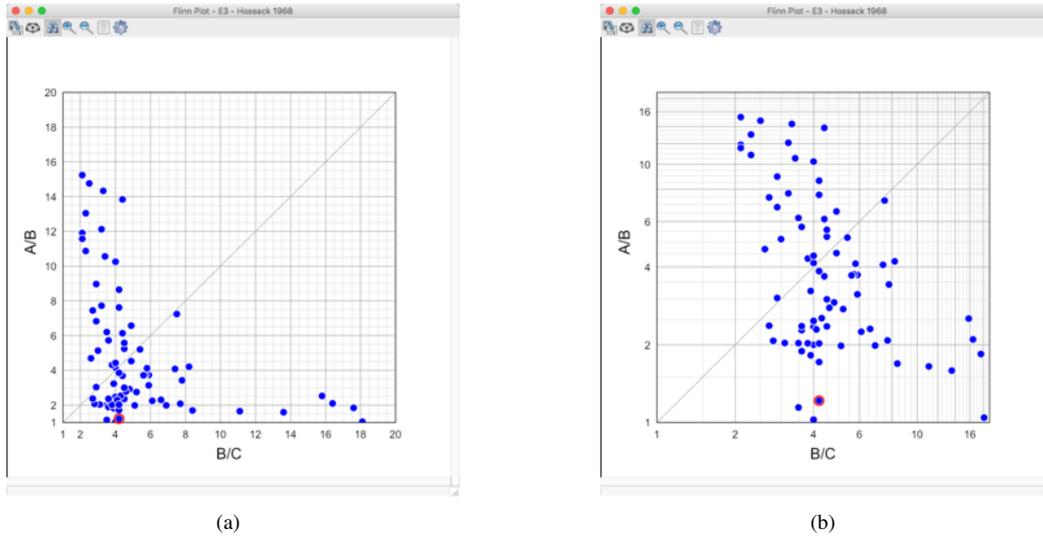


Figure 7.1: Flinn and Ramsay plots of deformed conglomerate ellipsoids, Bygdin area, Norway. The same data point is selected in both plots. Data from Hossack (1968) (a) Flinn plot. Note the clustering of data points at lower strains. (b) Ramsay (natural logarithmic Flinn) plot. The data shows less clustering at low strains, allowing better discrimination among data points. The natural strain values on this plot are more suitable for progressive deformation studies.

A shape parameter k_F is given by the slope on the Flinn plot

$$k_F = (R_{AB} - 1)/(R_{BC} - 1) \quad (7.1)$$

which varies from 0 to ∞ . The diagonal line $k = 1$ is the line of apparent plane strain (isochoric or constant volume plane strain), and separates the fields of oblate ($k_F < 1$) and prolate ($k_F > 1$) ellipsoids. The related shape parameter k_R is given by the slope on the Ramsay plot

$$k_R = \ln(R_{AB})/\ln(R_{BC}) \quad (7.2)$$

Similar to k_F , k_R varies from 0 to ∞ , and the $k_R = 1$ line of apparent plane strain separates the fields of oblate ($k_R < 1$) and prolate ($k_R > 1$) ellipsoids.

7.1.2 Nadai-Hsu Plot

The Nadai-Hsu plot (Hossack, 1968) is based on natural, or logarithmic, strain. In three dimensions, states of strain can be plotted using three orthogonal natural strain axes ε_1 , ε_2 , and ε_3 . A two-dimensional plot can be derived by projecting the points onto the plane

$$\varepsilon_1 + \varepsilon_2 + \varepsilon_3 = 0 \quad (7.3)$$

the strain plane. Although several variations of this plot are possible (Hsu, 1966), the polar version introduced by Hossack (1968) for geologic strain analysis is commonly used (Hobbs et al., 1976; Ramsay and Huber, 1983; Fossen, 2016). This plot uses two parameters, a radial parameter, quantifying the amount of strain

$$\varepsilon_S = (\sqrt{3}/2)\gamma_0 \quad (7.4)$$

where γ_0 , the natural octahedral unit shear, is given by

$$\gamma_0 = (2/3)[(\varepsilon_1 - \varepsilon_2)^2 + (\varepsilon_2 - \varepsilon_3)^2 + (\varepsilon_3 - \varepsilon_1)^2]^{1/2} \quad (7.5)$$

and a polar parameter, ν , Lode's ratio, which quantifies the strain symmetry

$$\nu = (2\varepsilon_2 - \varepsilon_1 - \varepsilon_3)/(\varepsilon_1 - \varepsilon_3) \quad (7.6)$$

Lode's ratio varies from -1 to 1. A value of $\nu = -1$ represents a prolate ellipsoid, and is equivalent to $k_R = \infty$, a value of $\nu = 1$ represents an oblate ellipsoid, equivalent to $k_R = 0$, and $\nu = 0$ represents apparent plane strain, equivalent to $k_R = 1$.

The symmetry of Lode's ratio, which ranges from -1 to 1, in contrast to the range of k_R from ∞ to 0, provides a natural equivalence between prolate and oblate ellipsoids. The plot provides a less distorted representation of the natural deviatoric strains than the Flinn or Ramsay plots, and is preferred for that reason (Brandon, 1995; Mookerjee and Peek, 2014; Fossen, 2016). To visualize the three-dimensional ellipsoid represented by a point on the plot, an ellipsoid shade plot (Section 7.1.3) can be displayed, as shown in Figure 7.2b. The shade plot is automatically updated to display the selected ellipsoid.

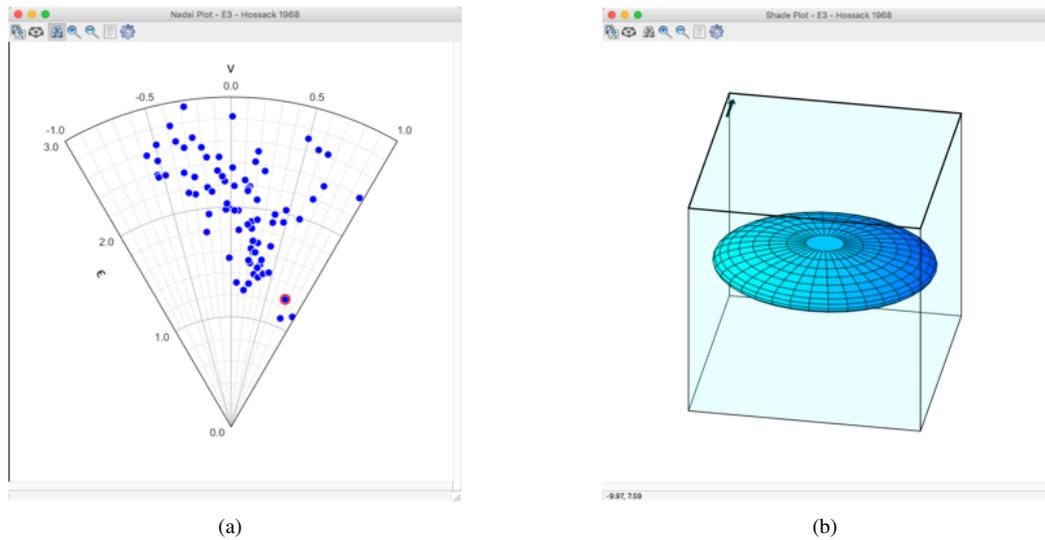


Figure 7.2: (a) Nadai-Hsu plot window displaying deformed conglomerate ellipsoids, Bygdin area, Norway, data from Hossack (1968). This plot is interactive, with the *Find Tool* selected, data points can be selected and will be simultaneously updated on the Flinn plot and in the *Data* window, the selected data point is also displayed in Figure 7.1 (b) An ellipsoid shade plot (Section 7.1.3) displaying the selected ellipsoid. The shade plot is updated to display any selected ellipsoid. This ellipsoid lies in the oblate field, $\nu = 0.76$, and can be interactively rotated with the mouse.



Figure 7.3: Deformed conglomerate, Bygdin area, Norway, where the data plotted in Figures 7.1 and 7.2 was collected by Hossack (1968). Photograph by F.W. Vollmer.

7.1.3 Shade Plot

To give a three-dimensional representation of a fabric ellipsoid an ellipsoid shade plot can be generated with the *Ellipsoid Shade Plot* command. Figure 7.4 shows the *Shade Plot* pane in the preferences dialog with available options. Shading is done by applying a color gradient by distance along a three-dimensional diagonal line, the *Light* option allows illumination from one of four quadrants (NW, NE, SE, or SW) from above or below. Default views include *Map*, *Isometric*, *Dimetric*, and *Trimetric*, however the plot can be rotated to any orientation by changing the *Rotation* (vertical axis) and *Tilt* (horizontal axis) angles, or by rotating it interactively using the mouse.

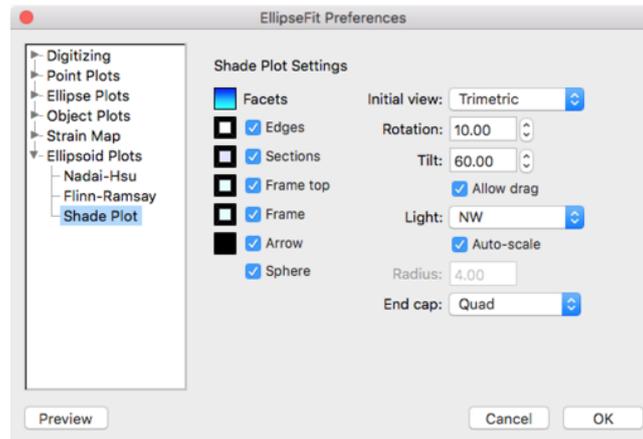


Figure 7.4: The *Shade Plot* pane in the *Preferences* dialog showing available options.

A three-dimensional cube frame can be drawn enclosing the plot to give coordinate information, along with an optional north arrow. By default the frame is colored with 5% opacity, and the top surface edges are drawn with a stroke of 2 points, to aid in depth perception. Figure 7.5 shows example plots of fabric ellipsoids generated from section data (Section 7.3). The plots are interactive, and can be rotated using the mouse, or in the preference dialog *Shade plot* preferences pane, Figure 7.4. The section planes can also be displayed, as illustrated in Figure 7.6. The section planes are displayed when selected in the data window.

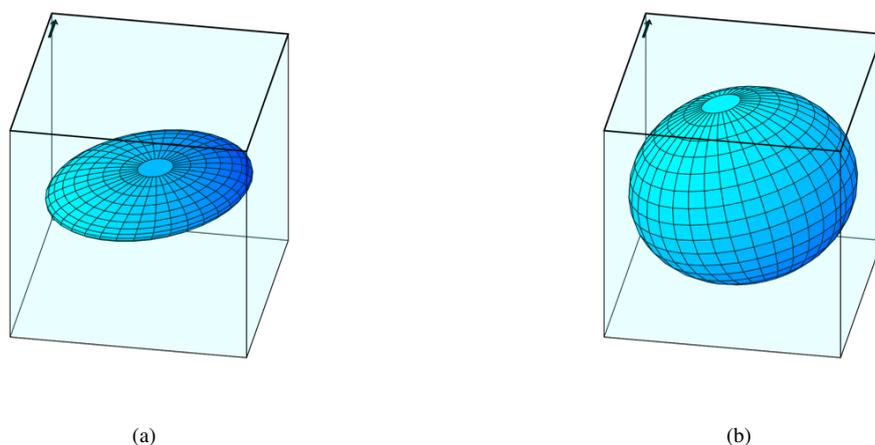


Figure 7.5: Shade plots of ellipsoids calculated using Shan's method (Section 7.3.2). (a) Ellipsoid generated from a sample of slate from North Wales, data from Owens (1984). (b) Ellipsoid calculated from a sample of Shawangunk Formation conglomerate, New York (Klemm et al., 2012, 2013).

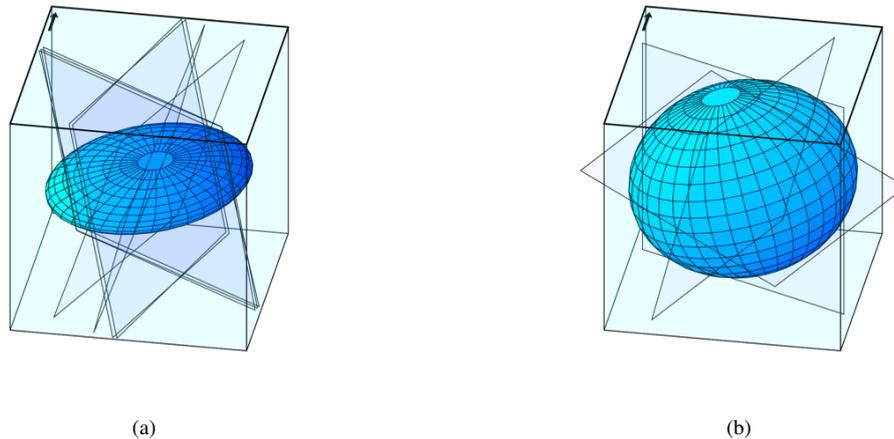


Figure 7.6: Shade plots of ellipsoids calculated using Shan's method (Section 7.3.2), with section planes displayed. The sections must be selected in the *Data* window to be displayed. (a) Plot as in Figure 7.5a showing seven sections used to calculate the ellipsoid. (b) Plot as in Figure 7.5b showing the three sections used to calculate the ellipsoid.

7.2 Global Coordinates and Sample Collection

The two-dimensional strain ellipses considered thus far have been referred to X, Y coordinates, where X is to the right, and Y is down on the image. These coordinate axes are indicated by the reference lines on the top and left of the *Image* window. The angle ϕ is the positive angle (clockwise) from X . This coordinate system was chosen to simplify the relationship to the global coordinates referred to here as X', Y', Z' , and to simplify the calculation of the three-dimensional strain ellipsoid. The global coordinates are equivalent to North, East, Down (NED).

In Figure 7.7 the shaded plane is a *section* plane that corresponds to an image analyzed for two-dimensional strain as discussed in earlier chapters. The X axis is parallel to the strike of the plane, using the (American) right hand rule (Pollard and Fletcher, 2005; Twiss and Moores, 2007; Fossen, 2016). The strike is given by θ , the standard azimuth as a clockwise angle from North in degrees. The dip of the plane is the angle δ from horizontal. The calculated strain ellipse is given by $R = a/b$, and ϕ , the angle from X , its pitch in the section plane. The calculated ellipse in an oriented section is a *section ellipse*.

In order to calculate the strain ellipsoid from the section ellipses, each section ellipse must undergo a coordinate transformation from local X, Y coordinates to global X', Y', Z' coordinates. This is done automatically, but the user must take care to properly prepare samples. Time taken at this stage will save aggravation later on. A sample collected in the field must be carefully oriented, recording its strike and dip (other conventions are fine, but the strike is the X coordinate axis so is used here). A suitable marking is a strike arrow and a dip tick (Figure 7.7), if possible on a surface that is not overhanging.

A minimum of three sections must be made through the sample, although more are preferred. Shan's method relaxes this requirement if lineation data is used as well, but the error range in natural samples can be large (Vollmer, 2010), so a minimum of three sections is still required. If available, lineation data can supplement the section ellipses (Section 7.3.4).

The sections should be at high angles to one another, but do not need to be at 90° angles, a restriction of some methods (Shimamoto and Ikeda, 1976). In making the cuts with a rock saw care must be taken not to destroy the strike arrow and dip tick. The sample is then taken outside, away from magnetic fields, and reoriented by fixing it in a block of clay or an orientable jig. The strikes and dips of the section planes are then measured, and strike arrows and dip ticks marked on each face. The faces are photographed, or made into thin sections. Depending on the grain size, thin section photographs can be made using a high resolution scanner, petrographic microscope camera, or scanning electron microscope. If extra large thin sections can be made, they will yield a larger

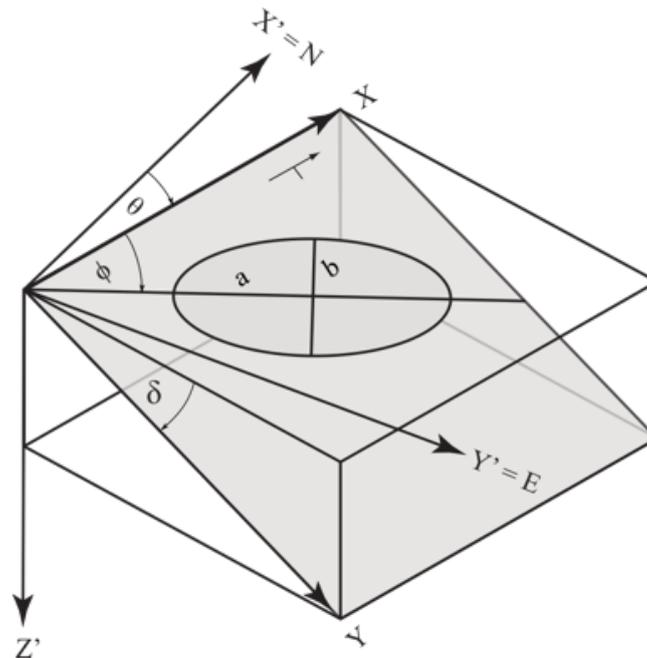


Figure 7.7: Coordinate system for section ellipses. The global coordinates are X' = North, Y' = East, and Z' = Down (NED). The plane with the section ellipse has a strike, θ (using the right hand rule), and dip, δ . The section ellipse has a pitch, ϕ , and ratio, $R = a/b$, where a and b are the lengths of the maximum and minimum axes. A suggested strike arrow and dip tick for marking a sample is shown.

sample size.

When making thin sections, keep the strike arrow parallel to one side and pointing right if possible, and similarly orient each photograph with the section strike to the right, and the dip line down. If necessary the photograph or the data can be rotated (Sections 3.1 and 6.7), but it is simpler to carefully orient the samples before digitizing.

One last detail is to keep track of the viewing direction. The strike arrow should point to the right in the section image, which means it is dipping towards the viewer. If the strike arrow points left, the view is of the *underside* of the section and it is dipping away from the viewer. If so, the image needs to be flipped horizontally about a vertical axis. The command *Image / Rotate Image / Flip Horizontal*, can be used to do this, but it is better to orient the photographs correctly before this stage. Vertical sections are not a problem if the recorded strike is kept to the right in the images.

7.3 Ellipsoid Calculation

Two methods for fabric ellipsoid calculation are implemented, the methods of Robin (2002) and Shan (2008). These are both direct non-iterative calculations with similarities to the method of Owens (1984). The iterative method of Mookerjee and Nickleach (2011) is not implemented, but is readily available as Mathematica scripts.

An ellipsoid can be represented by a shape matrix (or *inverse* shape matrix), b , and the desired solution is the optimal shape matrix, b^* . This matrix is the three dimensional equivalent of the (inverse) shape matrix for an ellipse (Section 6.5.2). The general equation of an ellipsoid centered at the origin, referred to three orthogonal coordinate axes, x , is the quadratic equation

$$b_{11}x_1^2 + b_{22}x_2^2 + b_{33}x_3^2 + 2b_{12}x_1x_2 + 2b_{13}x_1x_3 + 2b_{23}x_2x_3 = 1 \quad (7.7)$$

where x_1 , x_2 , and x_3 are points on the ellipsoid. In matrix form

$$x^T b x = 1 \quad (7.8)$$

where

$$\begin{aligned}
 b &= \begin{bmatrix} b_{11} & b_{12} & b_{13} \\ b_{12} & b_{22} & b_{23} \\ b_{13} & b_{23} & b_{33} \end{bmatrix} \\
 x &= \begin{bmatrix} x_1 \\ x_2 \\ x_3 \end{bmatrix} \\
 x^T &= [x_1 \quad x_2 \quad x_3]
 \end{aligned} \tag{7.9}$$

For an ellipsoid the eigenvalues of the matrix are positive numbers with principle values $b_1 \geq b_2 \geq b_3$. The eigenvectors give the orientations of the ellipsoid axes, and the magnitudes are given by

$$A = \frac{1}{\sqrt{b_3}}, \quad B = \frac{1}{\sqrt{b_2}}, \quad C = \frac{1}{\sqrt{b_1}} \tag{7.10}$$

Given three or more arbitrarily oriented section ellipses the goal is to find the optimal value, b^* , that satisfies some error minimizing criteria. The planes need not be perpendicular, although a robust solution requires the sections to include at least three at high angles (approximately 90°) to each other. Robin showed the solution to be a system of linear equations, and that a solution can always be found. Shan solved the problem by assuming the matrix can be located on a six-dimensional hypersphere centered at the origin, and recognized that the smallest eigenvector of the data matrix is the optimal solution.

7.3.1 Robin Method

Robin (2002) noted that the section fabric ellipse measured on any given face differs, by some error, from a section of the solution ellipsoid. That error can be represented by an error matrix, and by a squared norm for that error matrix. The best-fitting values for the parameters of the ellipsoid are those that minimize the sum of squared norms of the error matrices for all faces.

Robin distinguished two cases, depending on whether or not sectional measurements yield information on the areas of the sectional ellipses. In Case 1 (absolute ellipsoid), sectional measurements give information on areas, and the parameters describing the ellipsoid are the solution of a system of six linear equations. The data required for Case 1 is very difficult to obtain, because sections cutting through ellipsoidal particles rarely contain the ellipsoid center. In Case 2 (relative ellipsoid), measurements only provide an axial ratio and an angle for the sectional ellipses, ellipsoid parameters and the unknown scale factors are solutions of a system of linear equations. Robin's method was implemented by Launeau and Robin (2005), Webber and Klepeis (2018) implemented Case 2 in R, and Case 2 is implemented here (Vollmer, 2018a).

After calculation of the optimal ellipsoid, b^* , using Robin's method, the ellipsoid major axes are reported as stretches, and their orientations as trends and plunges (declinations and inclinations). Misfit residuals are calculated for each section ellipse to aid in detecting errors, such as incorrectly orientated sections. Section misfit residuals are discussed in Section 7.3.2, and complete examples with confidence calculations are given in Section 7.4.

7.3.2 Shan Method

The method of Shan (2008) is similar in theory to that of Robin (2002), but can also incorporate the long axes of strain ellipses, such those inferred from stretching lineations. Shan noted that it is not necessary to estimate both the relative and absolute strain ellipsoids at the same time, as Robin (2002), and others, did. He solved the problem under the assumption that the shape-matrix vector, b , can be located on a unit hypersphere centered at the origin, recognizing that the eigenvector of data matrix associated with the least eigenvalue is an optimal solution, b^* , of the shape matrix vector.

The directness of the eigenvalue solution makes the implementation compact and rapid, and it is implemented here (Vollmer, 2010).

Table 7.1 contains the results of a test of Shan's method using reduction spot data from Owens (1984). The test involves calculating the strain ellipsoid, b^* , from eight section ellipses, then, from the calculated ellipsoid, determining the section ellipses corresponding to the input section ellipses. These are reported as R_j^*, ϕ_j^* . The differences between the input section ellipses, R_j, ϕ_j , and the calculated R_j^*, ϕ_j^* are misfit section residuals $\Delta R_j, \Delta \phi_j$. Section ellipses are then calculated from the ellipsoid, and used to recalculate the ellipsoid, b^{T*} . The misfit section residuals, $\Delta R_j^T, \Delta \phi_j^T$, are next calculated. These residuals are negligible, indicating b^* was correctly retrieved.

For an ellipsoid calculation using Shan's method, the ellipsoid major axes are returned as stretches, and their orientations as trends and plunges (declinations and inclinations). Misfit residuals are calculated for each section ellipse to aid in detecting errors, such as incorrectly orientated sections. Complete examples, including confidence calculations, are given in Section 7.4.

j	θ	δ	a	b	R	ϕ	R^*	ϕ^*	ΔR	$\Delta \phi$	R_T^*	ϕ_T^*	ΔR_T	$\Delta \phi_T$
1	302	78	16.5	4.5	3.670	165	3.083	165.700	0.587	0.700	3.082	165.700	0.002	0.000
2	301	77	9.5	3.5	2.710	166	3.076	165.380	0.366	0.620	3.075	165.380	0.005	0.000
3	302	75	20.5	6.8	3.010	166	3.024	165.310	0.014	0.690	3.023	165.310	0.003	0.010
4	201	71	37.0	6.0	6.170	173	6.418	172.780	0.248	0.220	6.420	172.780	0.001	0.000
5	178	71	7.5	1.5	5.000	0	4.618	179.090	0.382	0.910	4.618	179.090	0.002	0.000
6	18	79	16.7	3.0	5.570	10	5.923	7.870	0.353	2.130	5.924	7.870	0.004	0.000
7	17	78	22.0	4.0	5.500	8	5.792	7.710	0.292	0.290	5.793	7.710	0.003	0.000
8	19	78	18.0	3.0	6.000	7	5.987	8.200	0.013	1.200	5.989	8.200	0.001	0.000

Table 7.1: Results of test of Shan's (Shan, 2008) method using data from Owens (1984). R^*, ϕ^* are the calculated b^* (Table 7.2) section ellipses. Misfit residuals $\Delta R, \Delta \phi$ indicate the error between calculated and measured ellipses. Calculated section ellipses were used to back-calculate b^{**} (Table 7.2) and R_T^*, ϕ_T^* . Misfit residuals $\Delta R_T, \Delta \phi_T$ indicate that the method does retrieve b^* . From Vollmer (2010).

7.3.3 Comparison of Ellipsoid Methods

Before giving example calculations, it is useful to compare the methods. Shan's method has been tested on synthetic and natural samples, the following are some of the results from Vollmer (2010). Owens (1984) tested his method on a sample of slate from Dinorwic North Wales, for which the strains had been calculated from reduction spots on 8 sections. His data was also used by Launeau and Robin (2005) to test Robin's (Robin, 2002) method. Table 7.1 shows results from Vollmer (2010) of tests on Shan's method using Owen's data.

Table 7.2 compares the results of ellipsoid calculations from this sample using the methods of Owens (1984), Robin (2002), and Shan (2008). The results are compared graphically in Figure 7.8. The calculations and plots were done in EllipseFit 2 and Orient 2 (Vollmer, 2010). There are negligible differences between the results using the methods of Robin and Shan, the results using the method of Owens deviate a small amount from them. Additional comparisons of Robin's and Shan's methods, done by generating 95% bootstrap confidence regions, are given in Section 7.4.

Axis	Owens	Robin	Shan (b^*)	b^{**}
S_1	2.340	2.626	2.565	2.567
t_1	29.000	37.100	34.960	34.970
p_1	10.000	11.300	10.890	10.890
S_2	1.197	1.112	1.131	1.131
t_2	122.000	129.500	127.350	127.360
p_2	14.000	11.700	12.230	12.230
S_3	0.357	0.343	0.345	0.345
t_3	265.000	264.500	264.440	264.440
p_3	73.000	73.600	73.510	73.510

Table 7.2: Comparison of calculated strain ellipsoids. *Owens* - Owens (1984). *Robin* - Launeau and Robin (2005), unweighted method of Robin (2002). *Shan (b^*)* - Vollmer (2010), using Shan's (Shan, 2008) method. b^{**} - Test to retrieve b^* from back-calculated section ellipses. The data is plotted in Figure 7.8. S are the principle axis stretches, t are their trends, and p are their plunges. From Vollmer (2010).

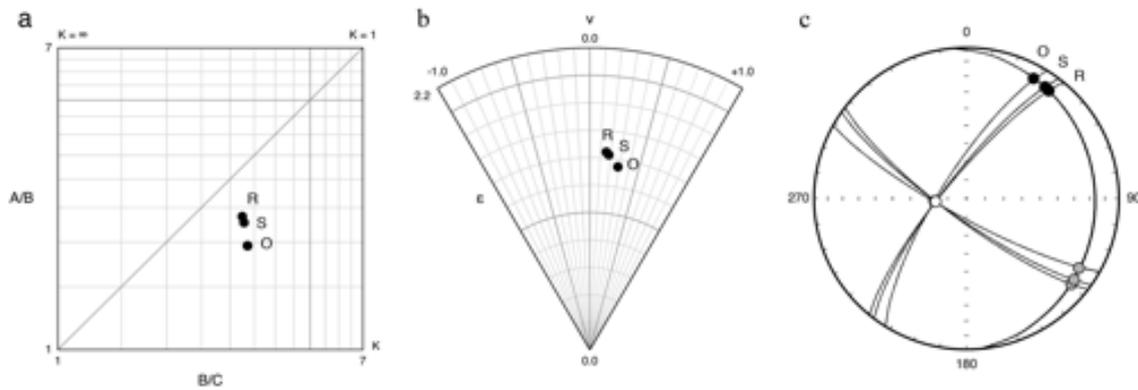


Figure 7.8: Comparison of calculated strain ellipsoids. (a) Ramsay plot, (b) Nadia-Hsu plot, (c) Schmidt plot. O - Owens (1984). R - Launeau and Robin (2005) using unweighted method of (Robin, 2002). S - Vollmer (2010) using Shan's (Shan, 2008) method. From Vollmer (2010).

7.3.4 Lineation Data

Shan's (Shan, 2008) method for ellipsoid calculation allows the use of section stretching lineations, an estimate of the maximum ellipse axes, in addition to ellipse data, that is, using sections that contain only the orientation of the section ellipse and not its axial ratio. Vollmer (2010) conducted tests of the lineation method using data from Owens (1984). The first test used the eight section ellipses in their original orientations, but constructed from the calculated best-fit ellipsoid. These idealized sections should, therefore, return the same final ellipsoid as calculated from the section ellipse data. Ten combinations of two ellipses, excluding those that were close in orientation, and six lineations were used to calculate an ellipsoid. As shown in Table 7.3, the calculations correctly return the correct ellipsoid within small errors. This affirms that the calculation works with ideal data.

Axis	b_{T14}^*	b_{T24}^*	b_{T34}^*	b_{T45}^*	b_{T46}^*	b_{T47}^*	b_{T48}^*	b_{T56}^*	b_{T57}^*	b_{T58}^*
S_1	2.569	2.570	2.570	2.570	2.569	2.569	2.570	2.568	2.568	2.570
t_1	35.060	35.100	35.010	35.180	35.030	35.030	35.010	35.230	35.220	35.010
p_1	10.900	10.910	10.890	10.930	10.900	10.900	10.890	10.940	10.940	10.890
S_2	1.130	1.131	1.130	1.132	1.130	1.130	1.130	1.133	1.133	1.130
t_2	127.450	127.490	127.400	127.570	127.420	127.420	127.400	127.620	127.610	127.400
p_2	12.210	12.200	12.220	12.190	12.220	12.220	12.220	12.180	12.180	12.220
S_3	0.344	0.344	0.344	0.344	0.344	0.344	0.344	0.344	0.344	0.344
t_3	264.450	264.440	264.450	264.440	264.450	264.450	264.450	264.440	264.440	264.450
p_3	73.510	73.520	73.510	73.520	73.510	73.510	73.510	73.520	73.520	73.510

Table 7.3: Test results of ellipsoid fitting using two ellipses and six lineations from perfect synthetic section ellipses calculated from b^* . For ten tests six of the eight R values were omitted, using only ϕ as lineations. Subscripts indicate the sections using with R data. The results are essentially identical down to round-off error. From Vollmer (2010).

The same sections were then used with the original input data to see if the same calculated ellipsoid would be returned. In this case the resulting calculated ellipsoids were highly variable, particularly in axial ratios (Table 7.4, Figure 7.9). While a limited test, it shows that natural samples using only two sectional ellipses with additional lineation data will not produce reliable results, and that a minimum of three section ellipses, at high angles to one another, should be used, which may be supplemented by additional lineation data.

Axis	b_{14}^*	b_{24}^*	b_{34}^*	b_{45}^*	b_{46}^*	b_{47}^*	b_{48}^*	b_{56}^*	b_{57}^*	b_{58}^*
S_1	nan	3.422	4.379	3.196	3.389	3.371	3.469	3.126	3.301	3.127
t_1	nan	41.760	47.150	43.140	20.310	20.330	20.320	42.680	45.960	37.500
p_1	nan	11.690	12.580	12.310	8.060	8.060	8.060	12.240	12.790	11.280
S_2	nan	0.902	0.836	1.052	0.584	0.585	0.578	0.301	1.054	1.021
t_2	nan	133.950	139.230	135.430	235.100	234.930	235.570	264.470	138.190	129.850
p_2	nan	10.430	9.240	10.370	80.220	80.240	80.160	73.780	9.730	11.610
S_3	nan	0.323	0.273	0.297	0.505	0.507	0.499	0.561	0.287	0.313
t_3	nan	264.630	264.590	264.450	111.090	111.110	111.110	264.470	264.450	264.490
p_3	nan	74.230	74.300	73.800	5.510	5.470	5.600	73.780	73.830	73.700

Table 7.4: Test of ellipsoid-fitting using two ellipses and six lineations from eight measured section ellipses from Owens (1984). For ten tests six of the eight R values were omitted. Subscripts indicate the sections with R data. The results are highly variable, especially as axial ratios, which are plotted in Figure 7.9. From Vollmer (2010).

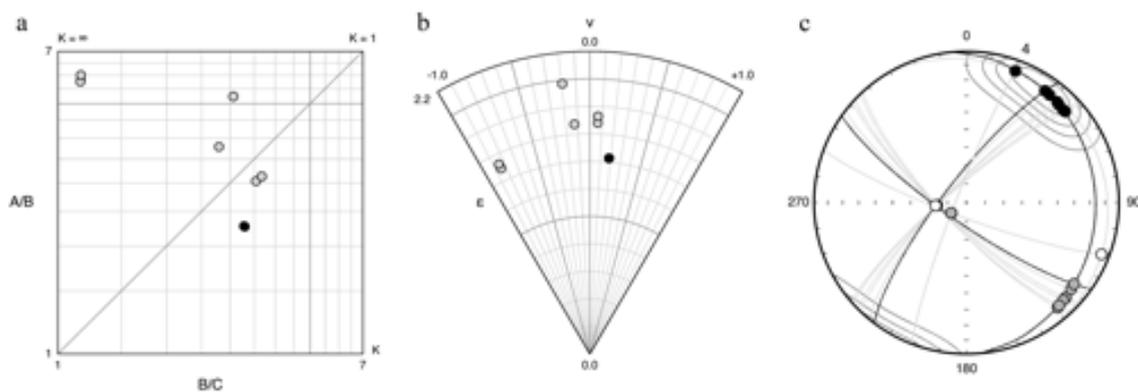


Figure 7.9: Test of ellipsoid-fitting using two ellipses and six lineations from eight measured section ellipses (Table 7.4). For ten tests six of the eight R values were omitted. The filled circles in (a) and (b), and the dark great circles in (c), represent the solution using all eight sections. The results, especially the axial ratios, are highly variable. This suggests that, for natural samples, using only two sections with lineation data is not valid. (a) Ramsay plot. (b) Nadia-Hsu plot. (c) Schmidt plot. From Vollmer (2010).

7.4 Error Analysis

Analyzing errors, or, more accurately, the *residuals*, to derive confidence regions in a three-dimensional analysis is complicated by the number of variables and how to address all possible measurement errors. One possibility is to weight each section ellipse by the confidence one has in it. This option is addressed by the methods of Owens (1984), Robin (2002), and Shan (2008), however deciding on a weight for a given section is not straightforward to implement objectively. An alternative is to create hundreds or thousands of randomized resamples or simulations that represent possible ellipsoid solutions, and to use these to estimate confidence intervals or regions.

A Monte Carlo type analysis can be used to randomly perturb the section ellipse parameters thousands of times, and recalculate the ellipsoid each time. Each of these simulations is saved, resulting in vectors of ellipsoid parameters that can be examined to determine confidence intervals (Mookerjee and Nickleach, 2011). This requires the choice of a method to select the random perturbations, the choice made here is to select them randomly from a bivariate normal distribution. This requires a

selection of the standard deviations, σ_R and σ_ϕ . If section data are available, the section data can be used to estimate them for each section using the *Section data* option (Section 7.4.1). If section data are not available, these can be estimated from the solution ellipsoid residuals (Section 7.4.2).

An alternative method is bootstrap analysis. In this case thousands of resamples are made to calculate potential ellipsoid solutions. For each ellipsoid resample, the section data for each section are randomly resampled with replacement to create a section resample. These section resamples are then used to calculate a resample ellipsoid. This method ties errors in the ellipsoid calculation directly to errors in the section ellipses, as the section ellipse resamples are derived from the section data. It is nonparametric, and does not require the assumption that the errors in R_j and ϕ_j follow a bivariate normal distribution. It is also flexible because, if section ellipse data are not available, but section data resamples are (Section 3.3.7), it is possible to use those. Webber and Klepeis (2018) suggest a similar technique. For these reasons, the bootstrap analysis is favored if section data or section data resamples are available.

Both methods give thousands of ellipsoid solutions that can be used to determine confidence regions on the ellipsoid shape, axes, and orientations. The errors are assumed to be in the calculations of the section ellipses, R_j, ϕ_j , so these parameters are randomly simulated or resampled. Measurement errors in the orientations of the sections also contribute to total error (Mookerjee and Nickleach, 2011), however, it is assumed here that the orientations of the sections are more accurately known than the section fabric ellipses.

7.4.1 Monte Carlo With Section Data

A Monte Carlo analysis creates hundreds or thousands of *simulations* by randomly perturbing, for each section, j , the ellipse parameters, R_j, ϕ_j , and recalculating the ellipsoid each time. Each of these simulations is saved, resulting in vectors of ellipsoid parameters that can be examined to determine confidence intervals. If the standard deviations, $\sigma_{R_j}, \sigma_{\phi_j}$, are known for each section, the perturbations can be selected from a bivariate normal distribution with these parameters. If the section data ellipses are available, as would be the case when digitizing sections with numerous shapes, it is possible to use the section ellipse data to estimate them. This method is similar to that used by Mookerjee and Nickleach (2011).

Using the section ellipse samples gives a connection from errors in the collected data to the ellipsoid calculation. The Monte Carlo method with the *Section data* option is described here using an example from a sample of the weakly deformed Shawangunk Formation conglomerate (Klemm et al., 2012, 2013). For each section the parameters σ_{R_j} and σ_{ϕ_j} are calculated as the standard errors of R_{ji} and ϕ_{ji} (standard deviation divided by $\sqrt{n_j}$), and used to determine random perturbations from a bivariate normal distribution with a mean of zero.

In the Example Data/Ellipsoid/Gunks folder are four files. Three are the input section ellipse data files, digitized from photomicrographs of three approximately perpendicular sections using the EllipseFit digitizing functions (Section 2.2):

```
KB32_IDP.csv
KB32_PTB.csv
KB32_PTS.csv
```

The last file:

```
Ellipse_Sections_KB32.tsv
```

contains the section ellipses (R, Φ), the orientations of the three sections (*Strike, Dip*), and the names of the corresponding data files (Figure 7.10). This file can be used for either Monte Carlo or bootstrap error analysis (Section 7.4.3).

To run the calculation, open the files (select all four in the *File Open Data* dialog). Then, using

	ID	R	Phi	Strike	Dip	Data File	Notes
1	1	1.159	8.27	203.00	75.00	KB32_PTS	PTS
2	2	1.032	248.36	23.00	15.00	KB32_PTB	PTB
3	3	1.149	159.42	113.00	90.00	KB32_IDP	IDP
4							

Figure 7.10: Data file for an ellipsoid calculation of the Shawangunk conglomerate sample KB32. The file contains the section ellipses (R , Φ), the section orientations ($Strike$, Dip), and the names of the files containing section ellipse data samples ($Data File$). This file can be used for either Monte Carlo or bootstrap error analysis.

the *Calculate Ellipsoid* command, select the *Error analysis*, *Monte Carlo*, and *Section data* options, and run the calculation using Shan's method (Figure 7.11). The *Append results* option appends the ellipsoid results to the open data list, so it can be plotted on Flinn-Ramsay, and Nadia-Hsu plots. Checking *Save orientations* will save the trends and plunges of the principal axes to a file that can be opened in Orient for plotting the ellipsoid axes on a Schmidt plot (Vollmer, 1995, 2015). The *Save resamples* option allows saving the bootstrap resample ellipsoid solutions as an EllipseFit file.

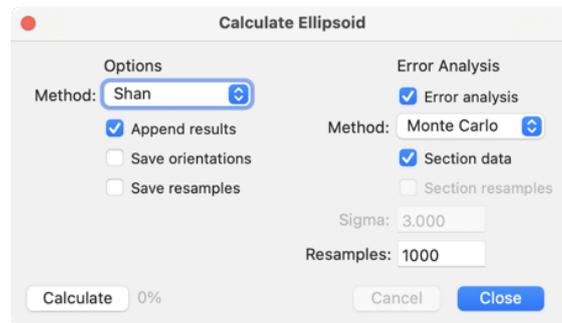


Figure 7.11: The *Calculate Ellipsoid* dialog showing options selected for a Shan method ellipsoid calculation using Monte Carlo error analysis with the *Section data* option. This uses the section data ellipses to estimate the standard deviations for the perturbations applied to the section ellipses. The *Save orientations* option allows saving the trends and plunges of the principal axes to a file that can be opened in Orient (Vollmer, 1995, 2015). The *Save resamples* option allows saving the bootstrap resample ellipsoid solutions as an EllipseFit file.

The fabric in this sample is very weak, so confidence intervals are particularly important. After selecting *Calculate*, the log file contains the following:

Best-Fit Ellipsoid Calculations

Ellipse_Sections_KB32

2020-06-27 15:53:46

=====

N = 3

Shan method

Ellipsoid axes as stretches:

Maximum (A)	=	1.083
Trend	=	255.45°
Plunge	=	13.23°
Intermediate (B)	=	1.020
Trend	=	346.32°
Plunge	=	3.69°
Minimum (C)	=	0.905
Trend	=	91.60°
Plunge	=	76.24°

Root mean square of section residuals:

R rms	= 0.025
ϕ rms	= 16.35°
Dist (dH) rms	= 2.34°

See data grid for section residuals

Confidence intervals:

Monte Carlo : 1000 simulations

Maximum (A):

Stretch 95%	= 0.021
Trend 95%	= 15.28°
Plunge 95%	= 6.61°
Alpha 95%	= 15.38°

Intermediate (B):

Stretch 95%	= 0.019
Trend 95%	= 15.19°
Plunge 95%	= 7.81°
Alpha 95%	= 15.95°

Minimum (C):

Stretch 95%	= 0.015
Trend 95%	= 38.24°
Plunge 95%	= 6.76°
Alpha 95%	= 10.09°

This includes all 3 principal stretches, and their trends and plunges, with 95% confidence levels. *Alpha 95%* is the angular error expressed as a semi-apical angle about the ellipsoid axis. To view the results graphically, first open a Flinn-Ramsay Plot, showing the Max/Int (S_1/S_2) versus Int/Min (S_2/S_3) ratios. The natural log Flinn, or Ramsay plot generally preferred (Section 7.1.1). A confidence polygon, or ellipse, is drawn covering the extent of ellipsoids within the 95% confidence range of the three axes.

The *Data* window (Figure 7.12) now displays the ellipsoid principal axes *Max*, *Int*, *Min* as stretches (S_1, S_2, S_3), and the calculated 95% confidence intervals. The section ellipses show the back-calculated values for *R* and ϕ (*R Est*, *Phi Est*), and the corresponding residuals (*R Res*, *Phi Res*). The hyperbolic distance, d_H , residuals (*Dist Res*) are a single parameter that indicates the section misfits in degrees, which is useful for identifying sections with the greatest misfit.

For comparison, the ellipsoid calculation can be repeated using the Robin method, which generates a similar output in the log. Figure 7.13 shows the 95% confidence regions calculated using both Shan and Robin methods of the KB32 conglomerate data on Ramsay and Nadia-Hsu plots respectively. In each case the Robin solution is shifted slightly down and to the right.

Figure 7.14a is a Schmidt plot of the ellipsoid axes with 95% Monte Carlo confidence cones plotted using Orient (Vollmer, 1995, 2015). Figure 7.14b is an ellipsoid shade plot of the solutions for KB32 conglomerate sample data with section planes displayed, plots for the Shan and Robin solutions are indistinguishable. These results are consistent with a weak, but statistically significant, flattening fabric.

	ID	Max	Int	Min	R	Phi	Max/Min	Int/Min	Max/Int	KF	KR	Epsilon	Nu	Strike	Dip	Max Dec
1	1				1.159	8.27	1.159							203.00	75.00	
2	2				1.032	68.36	1.032							23.00	15.00	
3	3				1.149	159.42	1.149							113.00	90.00	
4	4	1.083	1.020	0.905	1.196		1.196	1.127	1.061	0.484	0.499	0.129	0.335			255.45

(a)

	x Dec	Max Inc	Int Dec	Int Inc	Min Dec	Min Inc	R Est	Phi Est	R Res	Phi Res	Dist Res	Max 95...	Int 95%	Min 95%	Data File	Notes
1							1.122	11.60	0.037	3.33	2.04				KB32_PTS	PTS
2							1.043	29.15	-0.011	39.21	2.69				KB32_PTB	PTB
3							1.169	166.38	-0.020	6.96	2.28				KB32_IDP	IDP
4	55.45	13.23	346.32	3.69	91.60	76.24						0.021	0.019	0.014		

(b)

Figure 7.12: The *Data* window after calculating the optimal ellipse using Shan’s method. (a) Scrolled left, new columns display: ellipsoid axial ratios (*Max/Min*, *Max/Int*, *Int/Min*), Flinn plot parameter *KF*, Ramsay plot parameter *KR*, and Nadia-Hsu parameters *Epsilon*, and *Nu* (Section 7.1). (b) Scrolled right, new columns display: section ellipse estimates calculated from the estimated ellipsoid (*R Est*, *Phi Est*), with residuals (*R Res*, *Phi Res*), the hyperbolic distance (Section 6.2.3) residuals in degrees (*Dist Res*), and the bootstrap 95% confidence on the ellipsoid axes. Additional results are given in the *Log* window.

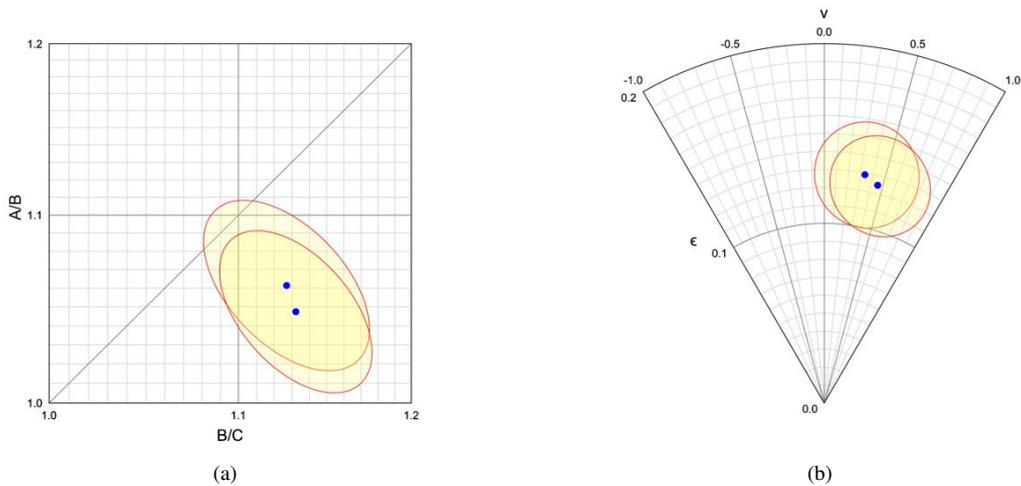


Figure 7.13: Shape plots of the KB32 conglomerate sample data with 95% confidence regions determined using Monte Carlo error analysis with the *Section data* option, showing solutions for Shan and Robin methods. The Robin solution is shifted slightly down and to the right on both plots. (a) Ramsay plot. (b) Nadia-Hsu plot.

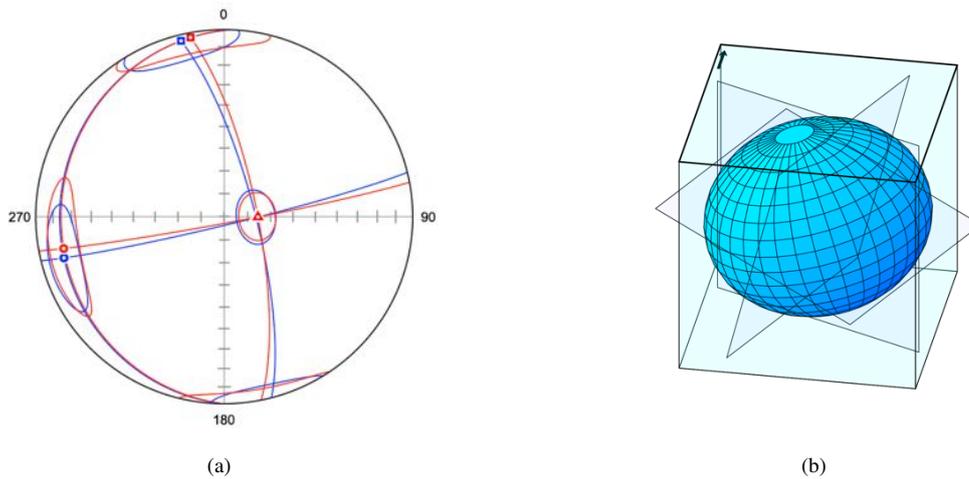


Figure 7.14: Plots of the Shawangunk KB32 conglomerate ellipsoid solution using Monte Carlo simulations. (a) Schmidt plot of ellipsoid axes calculated using Shan (blue) and Robin (red) methods with 95% confidence cones (circle = S_1 , square = S_2 , triangle = S_3). Plotted using Orient (Vollmer, 1995, 2015). (b) Ellipsoid shade plot with section planes displayed, plots for the Shan and Robin solutions are indistinguishable. These are consistent with a weak, but statistically significant, flattening fabric.

7.4.2 Monte Carlo Without Section Data

In a Monte Carlo simulation the input section ellipses R_j, ϕ_j are perturbed thousands of times, ellipsoids are calculated for each of these simulations, and vectors of ellipsoid parameters are created, which can be examined to determine confidence intervals or regions. In this section, the situation in which section ellipse data samples are *not* available is treated, see Section 7.4.1 for a more robust method that uses section ellipse data samples, if available, to estimate the perturbations.

In order to determine a suitable magnitude of perturbation, the section ellipse misfit residuals, $\Delta R_j, \Delta \phi_j$, are examined. The maximum residual is taken by default to represent 3.0 standard deviations, that is, all residuals are assumed to lie within three standard deviations of the mean, and perturbations are selected randomly from that normal distribution.

The following example illustrates this technique using Shan's method, but the procedure is identical for Robin's method. The file:

Owens 1984 T1.csv

contains 8 section ellipses measured from a sample of slate with reduction spots from Dinorwic, North Wales (Owens, 1984). The data as displayed in the *Data* window is shown in Figure 7.15.

ID	Max	Min	Area	R	Phi	Strike	Dip		
1	16.500	4.500	233.263	3.670	165.00	302.00	78.00		
2	9.500	3.500	104.458	2.710	166.00	301.00	77.00		
3	20.500	6.800	437.938	3.010	166.00	302.00	75.00		
4	37.000	6.000	697.434	6.170	173.00	201.00	71.00		
5	7.500	1.500	35.343	5.000	0.00	178.00	71.00		
6	16.700	3.000	157.394	5.570	10.00	18.00	79.00		
7	22.000	4.000	276.460	5.500	8.00	17.00	78.00		
8	18.000	3.000	169.646	6.000	7.00	19.00	78.00		
9									
10									

Figure 7.15: Section data measured from a sample of slate with reduction spots from Dinorwic, North Wales (Owens, 1984), displayed in the *Data* window.

Figure 7.16 shows the *Calculate Ellipsoid* dialog and the options for the calculation. Set the *Method* to *Shan*, select *Error analysis*, *Monte Carlo*, and deselect *Section data*, as the section data is

not available for this data set. *Sigma* is the value used in determining the magnitude of the random perturbation, leave this at the default value of 3.0. The number of simulations for a Monte Carlo analysis is specified in the *Resamples* edit box, 1000 is the default value. Press *Calculate* to start the calculation, and shortly the results appear in the *Data* window (Figure 7.17) and the *Log* window.

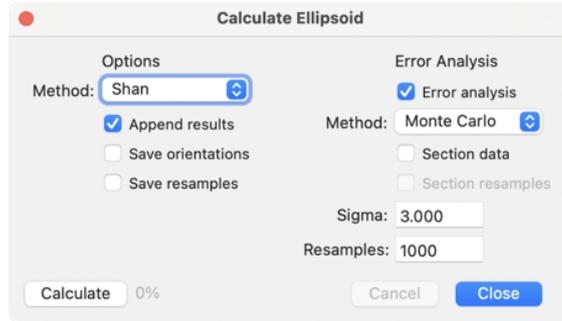


Figure 7.16: The *Calculate Ellipsoid* dialog showing options selected for a Shan method ellipsoid calculation with Monte Carlo error analysis. Section data ellipses are not available for this data set, so *Section data* must be unchecked.

The *Data* window now displays the ellipsoid principal axes *Max*, *Int*, *Min* as stretches (S_1, S_2, S_3), and the calculated 95% confidence intervals. The section ellipses show the back-calculated values for *R* and ϕ (*R Est*, *Phi Est*), and the corresponding residuals (*R Res*, *Phi Res*). The hyperbolic distance, d_H , residuals (*Dist Res*) are a single parameter that indicates the section misfits in degrees, which is useful for identifying sections with the greatest misfit.

	ID	Max	Int	Min	Area	R	Phi	Max/Min	Int/Min	Max/Int	KF	KR	Epsilon	Nu	Strike
1	1	16.500		4.500	233.263	3.670	165.00	3.670							302.00
2	2	9.500		3.500	104.458	2.710	166.00	2.710							301.00
3	3	20.500		6.800	437.938	3.010	166.00	3.010							302.00
4	4	37.000		6.000	697.434	6.170	173.00	6.170							201.00
5	5	7.500		1.500	35.343	5.000	0.00	5.000							178.00
6	6	16.700		3.000	157.394	5.570	10.00	5.570							18.00
7	7	22.000		4.000	276.460	5.500	8.00	5.500							17.00
8	8	18.000		3.000	169.646	6.000	7.00	6.000							19.00
9	9	2.565	1.131	0.345		7.445		7.445	3.283	2.268	0.555	0.689	1.428	0.184	

(a)

	Dip	Max Dec	Max Inc	Int Dec	Int Inc	Min Dec	Min Inc	R Est	Phi Est	R Res	Phi Res	Dist Res	Max 95%	Int 95%	Min 95%
1	78.00							3.083	165.70	0.587	0.70	10.22			
2	77.00							3.076	165.38	-0.366	0.62	7.43			
3	75.00							3.024	165.31	-0.014	0.69	1.88			
4	71.00							6.418	172.78	-0.248	0.22	2.64			
5	71.00							4.618	179.09	0.382	0.91	6.19			
6	79.00							5.923	7.87	-0.353	2.13	12.36			
7	78.00							5.792	7.71	-0.292	0.29	3.35			
8	78.00							5.987	8.20	0.013	1.20	6.97			
9		34.96	10.89	127.35	12.23	264.44	73.51						1.054	0.195	0.052

(b)

Figure 7.17: The *Data* window after calculating the optimal ellipse using Shan’s method. (a) Scrolled left, new columns display: ellipsoid axial ratios (*Max/Min*, *Max/Int*, *Int/Min*), Flinn plot parameter *KF*, Ramsay plot parameter *KR*, and Nadia-Hsu parameters *Epsilon*, and *Nu* (Section 7.1). (a) Scrolled right, new columns display: section ellipse estimates back-calculated from the estimated ellipsoid (*R Est*, *Phi Est*), with residuals (*R Res*, *Phi Res*), the hyperbolic distance (Section 6.2.3) residuals in degrees (*Dist Res*), and the bootstrap 95% confidence on the ellipsoid axes. Additional results are given in the *Log* window.

The *Log* window displays the values for all 3 principal stretches, and their trends and plunges, with 95% confidence levels. *Alpha 95%* is the angular error expressed as a semi-apical angle about the ellipsoid axis. To view the results graphically, first open a Flinn-Ramsay plot (Section 7.1.1). A

confidence polygon, or ellipse, is drawn covering the extent of ellipsoids within the 95% confidence range of the three axes.

Next open a Nadai-Hsu plot, which is based on natural, or logarithmic strain, which is also the basis for equidistant hyperbolic projections discussed in Section 6.2.3. This provides a less distorted representation of the deviatoric strains and is preferred for that reason (Section 7.1.2). This plot similarly shows a confidence polygon, or ellipse, covering the extent of ellipsoids within the 95% confidence range of the three axes.

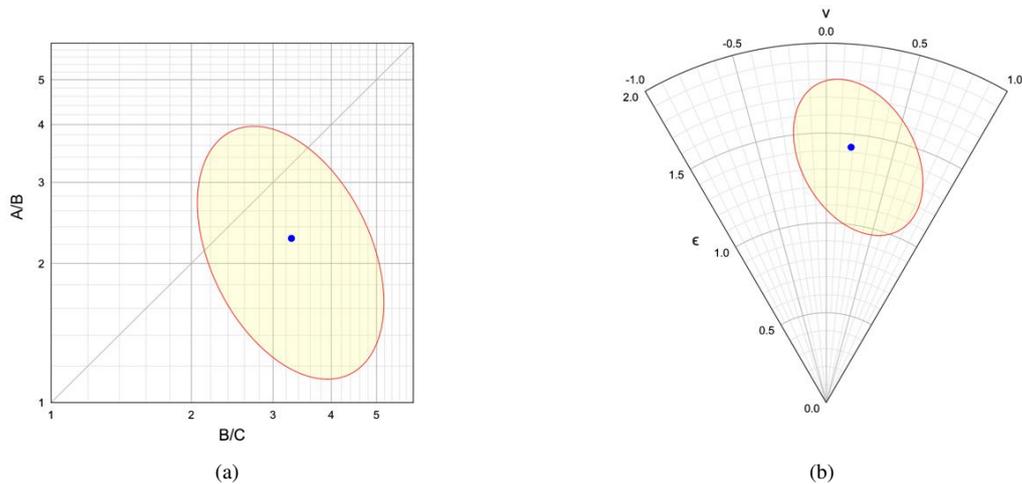


Figure 7.18: Shape plots of the ellipsoid axial ratios determined from the Shan calculation using data from all 8 sections (Figure 7.15), with the 95% confidence region. (a) Ramsay (logarithmic Flinn) plot. (b) Nadai-Hsu plot.

The calculated strain has a large 95% error region as shown in both plots (Figure 7.18). Examining the data (Figure 7.17b), shows that section 6 has the largest distance residual (*Dist Res*). Select it, delete it and repeat the calculation. Figure 7.19 shows the updated Flinn-Ramsay plot, which now shows both solutions. The Nadai-Hsu plot is also updated to reflect the newly calculated results. Deleting the outlier has significantly decreased the size of the confidence regions.

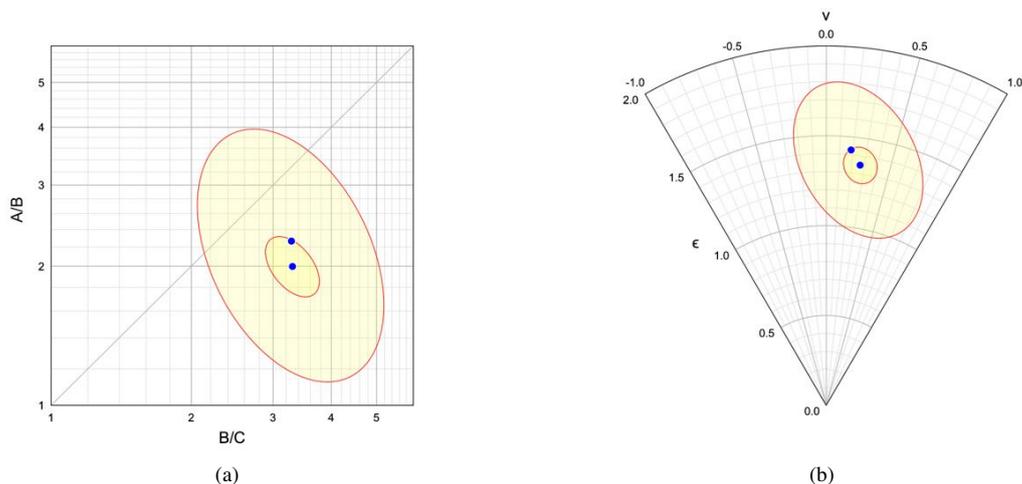


Figure 7.19: Shape plots of the ellipsoid axial ratios determined from the Shan calculation after deleting one section with the greatest combined residual (*Dist Res*), and repeating the calculation with the remaining 7 sections (Figure 7.15), with the 95% confidence region. (a) Ramsay (logarithmic Flinn) plot. (b) Nadai-Hsu plot.

Finally for comparison, the results with section 6 removed using both Shan's and Robin's method are plotted in Figure 7.20. The solutions are nearly identical with similar confidence regions, although Shan's method produces slightly smaller confidence regions.

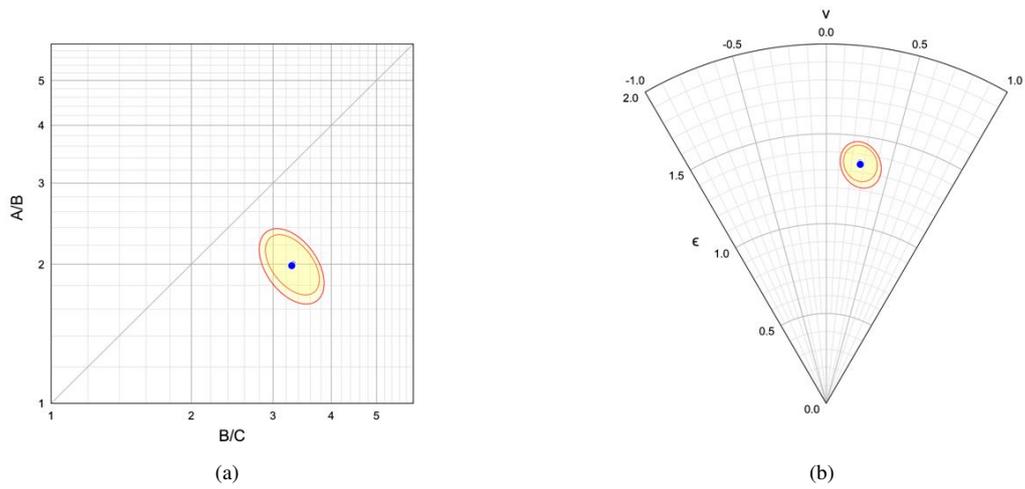


Figure 7.20: Plots of the ellipsoid axial ratios of the Owens T1 data calculated using both Shan and Robin methods, with 95% confidence regions, after deleting section 6. The solution to Shan's method has the smaller confidence region. (a) Ramsay plot. (b) Nadia-Hsu plot.

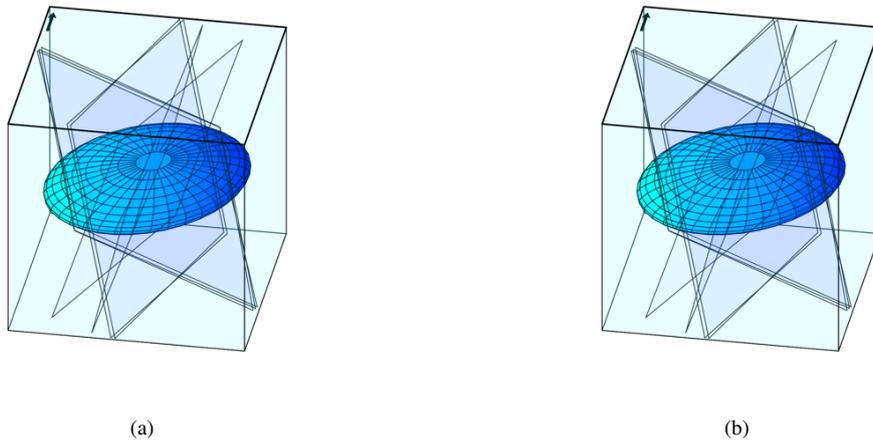


Figure 7.21: Ellipsoid shade plots of the solution after removing section 6. (a) Shan's method. (b) Robin's method.

7.4.3 Bootstrap With Section Data

Monte Carlo analysis using section data (Section 7.4.1) ties the ellipsoid analysis to the variability of the section data by using that variability to choose σ values for simulation parameters, however another option is to do a bootstrap analysis that resamples the section data to calculate thousands of potential ellipsoid solutions. This directly ties errors in measured section data to errors in the ellipsoid calculation, using resamples of the original data, rather than simulations. It is nonparametric, so does not require that errors in R_j and ϕ_j be selected from a bivariate normal distribution.

For bootstrap analysis the number of resamples is chosen, normally a minimum of one thousand. For each resample, section ellipse resamples are calculated from random resamples of the section data with replacement. These section ellipse resamples are then used to calculate an ellipsoid resample solution. The resulting vector of ellipsoid resample solutions can then be examined for confidence intervals for the ellipsoid axes and their orientations.

This analysis is explained using an example from a sample of the weakly deformed Shawangunk Formation conglomerate (Klemm et al., 2012, 2013). In the Example Data/Ellipsoid/Gunks folder are four files. Three files are the input section ellipse data files, digitized from photomicrographs of three approximately perpendicular sections using the EllipseFit digitizing functions (Section 2.2):

KB32_IDP.csv
KB32_PTB.csv
KB32_PTS.csv

The last file:

Ellipse_Sections_KB32.tsv

contains the section ellipses (R , Φ), the orientations of the three sections ($Strike$, Dip), and the names of the corresponding data files (Figure 7.10). To run the calculation, open the files (select all four in the *File Open Data* dialog). In the *Calculate Ellipsoid* dialog, select *Shan*, *Error analysis*, and *Bootstrap* (*Section resamples* should not be checked). Figure 7.22 shows plots of 1000 bootstrap resample ellipsoids used to calculate the confidence regions. The bootstrap resample ellipsoids are not automatically displayed, but can be saved to files using the *Save resamples* and *Save orientations* options.

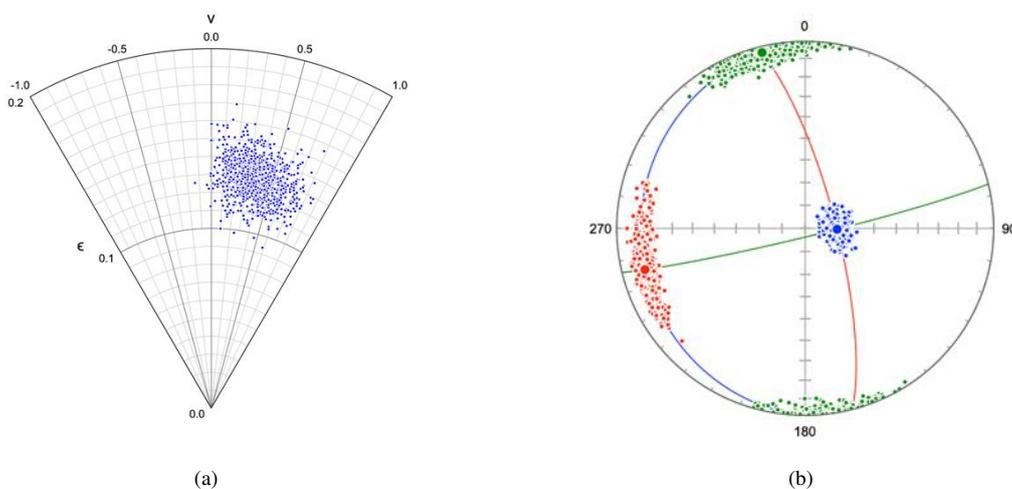


Figure 7.22: Plots of bootstrap resample ellipsoids for Shan method used to estimate confidence regions. (a) Nadia-Hsu plot of resample ellipsoid shapes saved using the *Save resamples* option. (b) Schmidt plot of ellipsoid axes saved using the *Save orientations* option, and plotted using Orient (red - S_1 , green - S_2 , blue - S_3).

For comparison, the ellipsoid calculation can be repeated using the Robin method, which generates

a similar output in the log. Figure 7.23 shows the 95% confidence regions calculated using both Shan and Robin methods of the KB32 conglomerate data on Ramsay and Nadia-Hsu plots respectively. In each case the Robin solution is shifted slightly down and to the right.

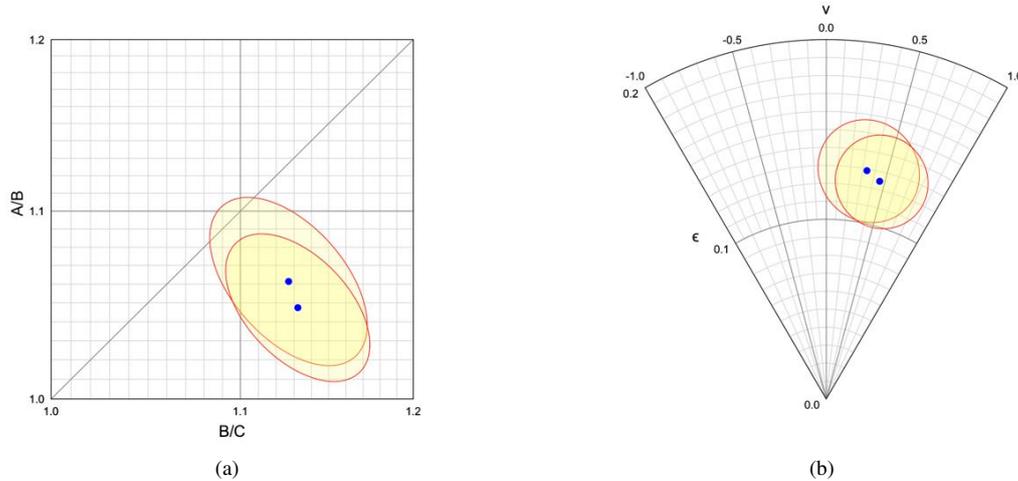


Figure 7.23: Shape plots of the KB32 sample solution with 95% confidence regions determined using bootstrap error analysis, for Shan and Robin methods. The Robin solution is shifted slightly down and to the right on both plots. (a) Ramsay plot. (b) Nadia-Hsu plot.

Figure 7.24a is a Schmidt plot of the ellipsoid axes with 95% bootstrap confidence cones plotted using Orient (Vollmer, 1995, 2015). Figure 7.24b is an ellipsoid shade plot of the solutions for KB32 conglomerate sample data with section planes displayed, plots for the Shan and Robin solutions are indistinguishable. These results are consistent with a weak, but statistically significant, flattening fabric. These results are similar to those found using Monte Carlo simulations (Section 7.4.1), however, bootstrapping the section ellipses from the section data is nonparametric, and does not require the assumption that the errors in R_j and ϕ_j follow a bivariate normal distribution.

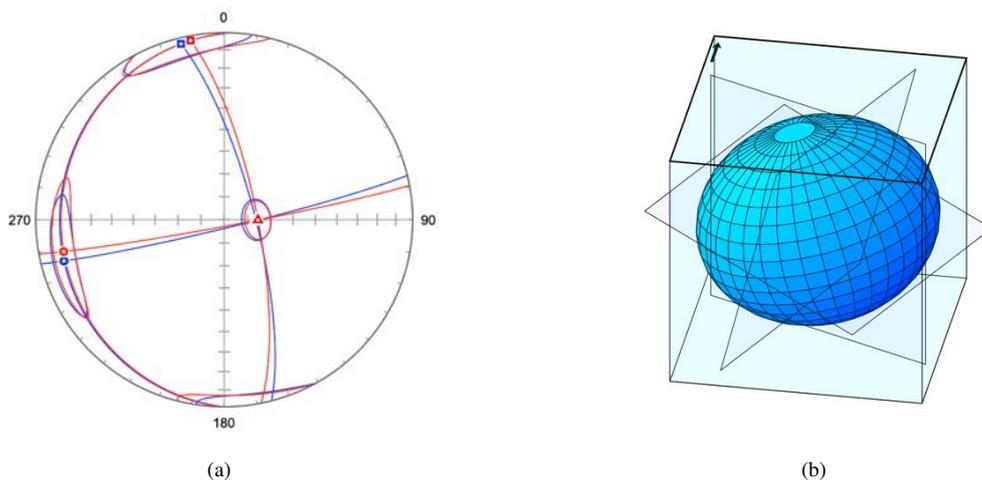


Figure 7.24: Plots of the Shawangunk conglomerate KB32 ellipsoid calculation solution using section data ellipses. (a) Schmidt plot of ellipsoid axes with 95% confidence regions calculated using Shan (blue) and Robin (red) methods (circle - S_1 , square - S_2 , triangle - S_3). Plotted using Orient (Vollmer, 1995, 2015). (b) Ellipsoid shade plot with section planes displayed, plots for the Shan and Robin solutions are indistinguishable. These are consistent with a weak, but statistically significant, flattening fabric.

7.4.4 Bootstrap With Section Resamples

In some cases, for example when using Fry or point distribution analysis (Section 3), section data ellipses may not be available, since only one ellipse is determined for each section. However, for some objective void-fitting methods (Section 3.3) it is possible to calculate, and save, bootstrap section resamples for error analysis (Section 3.3.7). In this case, a similar procedure to that in Section 7.4.3 is followed, except the section data files must contain bootstrap *section resamples* (Figure 7.25), rather than *section data ellipses*. The *Section resamples* option must be selected (Figure 7.26), and the files are assumed to contain previously calculated bootstrap resample means. Rather than calculating a new section resample mean for each iteration, an already calculated resample mean is sequentially selected from the section file. Note that, in this case, setting the number of resamples to a value greater than the number of resample means available in the data files does not increase confidence in the result. Example data files are provided in the example data folder Ellipsoid/Gunks/Bootstrap. Figure 7.27 shows Nadai-Hsu and Schmidt plots for the solution ellipsoids with 95% confidence regions.

	ID	R	Phi	Strike	Dip	Data File	Notes
1	1	1.159	8.27	203.00	75.00	KB32_PTS-BS	PTS
2	2	1.032	68.36	23.00	15.00	KB32_PTB-BS	PTB
3	3	1.149	159.42	113.00	90.00	KB32_IDP-BS	IDP
4							

Figure 7.25: Data file for an ellipsoid calculation of the Shawangunk conglomerate sample KB32 using previously saved section bootstrap files. The file contains the section ellipses (R , Φ), the section orientations ($Strike$, Dip), and the names of the files containing section bootstrap *resample means* ($Data File$).

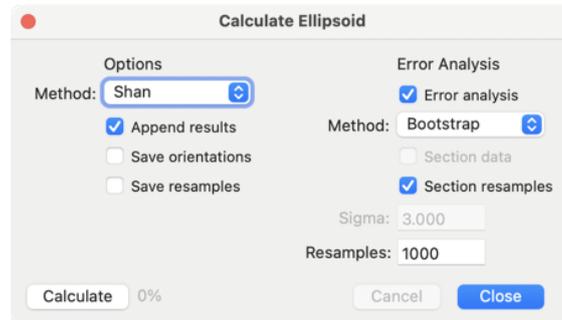


Figure 7.26: The *Calculate Ellipsoid* dialog showing options selected for a Shan method ellipsoid calculation with bootstrap error analysis using section resample data, the *Bootstrap* and *Section resamples* are selected. In this case, the data files must contain section resample means, rather than section data ellipses.

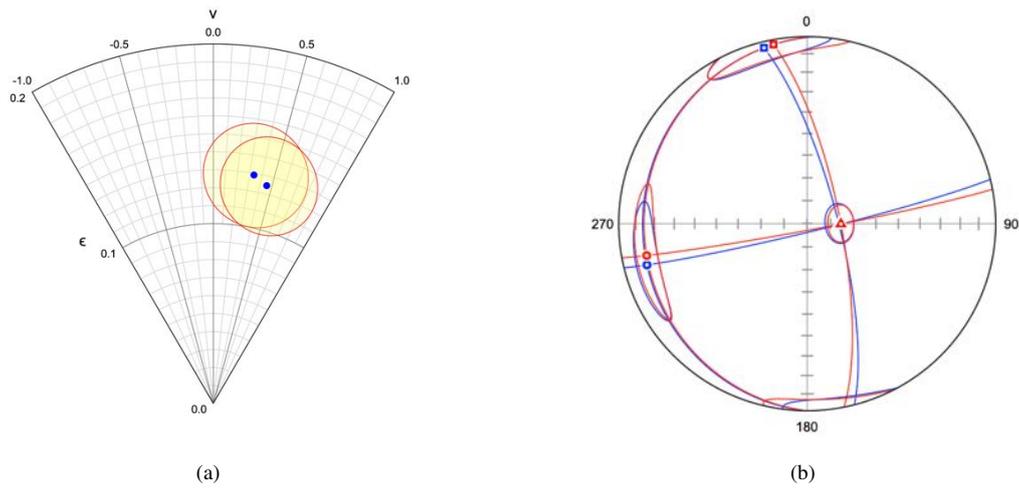


Figure 7.27: Plots of the Shawangunk conglomerate KB32 ellipsoid solution with 95% confidence regions using bootstrap section resamples. (a) Nadai-Hsu shape plot, the Robin solution is shifted slightly down and to the right. (b) Schmidt plot of ellipsoid axes calculated using Shan (blue) and Robin (red) methods (circle - S1, square - S2, triangle - S3). Plotted using Orient (Vollmer, 1995, 2015).

8 Image Processing

Although the manual outlining or digitizing of particles is generally required for fabric analysis, advances have been made in the automatic detection of fabrics. EBSD analysis can be used to identify grain shapes using orientation mismatches with software such as MTEX (Bachmann et al., 2011), x-ray tomography allows three-dimensional fabric analysis, and magnetic AMS fabrics have been found useful as strain indicators (Burmeister et al., 2009). Section 8.1 discusses the implementation of rapid objective fabric analysis from images using *edge detection* techniques (Glazner and Walker, 2020).

When the manual outlining or digitizing of particles is necessary, image processing can assist in detecting object outlines. The *Image Filters* dialog implements some common image filters, and the *Edge Detection* dialog implements edge detection algorithms (Efford, 2000; Parker, 2011).

8.1 Edge Fabric Ellipse

Edge detection (Section 8.2.2) is a common technique in image analysis (Efford, 2000; Parker, 2011), and can be applied to fabric shape analysis (Glazner and Walker, 2020). Prewitt edge detection uses the kernels (Efford, 2000, p. 164)

$$\begin{aligned} h_x &= \begin{bmatrix} -1 & 0 & 1 \\ -1 & 0 & 1 \\ -1 & 0 & 1 \end{bmatrix} \\ h_y &= \begin{bmatrix} -1 & -1 & -1 \\ 0 & 0 & 0 \\ 1 & 1 & 1 \end{bmatrix} \end{aligned} \quad (8.1)$$

The Sobel kernels (Efford, 2000, p. 165), which weight adjacent pixels more heavily, are an alternative

$$\begin{aligned} h_x &= \begin{bmatrix} -1 & 0 & 1 \\ -2 & 0 & 2 \\ -1 & 0 & 1 \end{bmatrix} \\ h_y &= \begin{bmatrix} -1 & -2 & -1 \\ 0 & 0 & 0 \\ 1 & 2 & 1 \end{bmatrix} \end{aligned} \quad (8.2)$$

These kernels are *correlated* with an image, by moving the kernel from pixel to pixel, multiplying the kernel elements by the lightness of the neighboring pixels, and summing them. The h_x kernel gives a gradient in the x direction, and the h_y kernel gives a gradient in the y direction. The lightness gradient is given by a vector

$$\vec{g} = \begin{bmatrix} g_x \\ g_y \end{bmatrix} \quad (8.3)$$

whose magnitude and direction are

$$\begin{aligned} g &= \sqrt{g_x^2 + g_y^2} \\ \phi &= \arctan(g_y/g_x) \end{aligned} \quad (8.4)$$

A variance-covariance matrix of the pixel gradients is

$$V = \frac{1}{n_p - 1} \sum_{k=1}^{n_p} \begin{bmatrix} (g_{xk} - \bar{g}_x)^2 & (g_{xk} - \bar{g}_x)(g_{yk} - \bar{g}_y) \\ (g_{yk} - \bar{g}_y)(g_{xk} - \bar{g}_x) & (g_{yk} - \bar{g}_y)^2 \end{bmatrix} \quad (8.5)$$

where the summation is over n_p image pixels, and \bar{g}_x, \bar{g}_y are the mean values. The eigenvectors of this matrix give the magnitudes and orientations of the principal edge gradient axes. The fabric ellipse

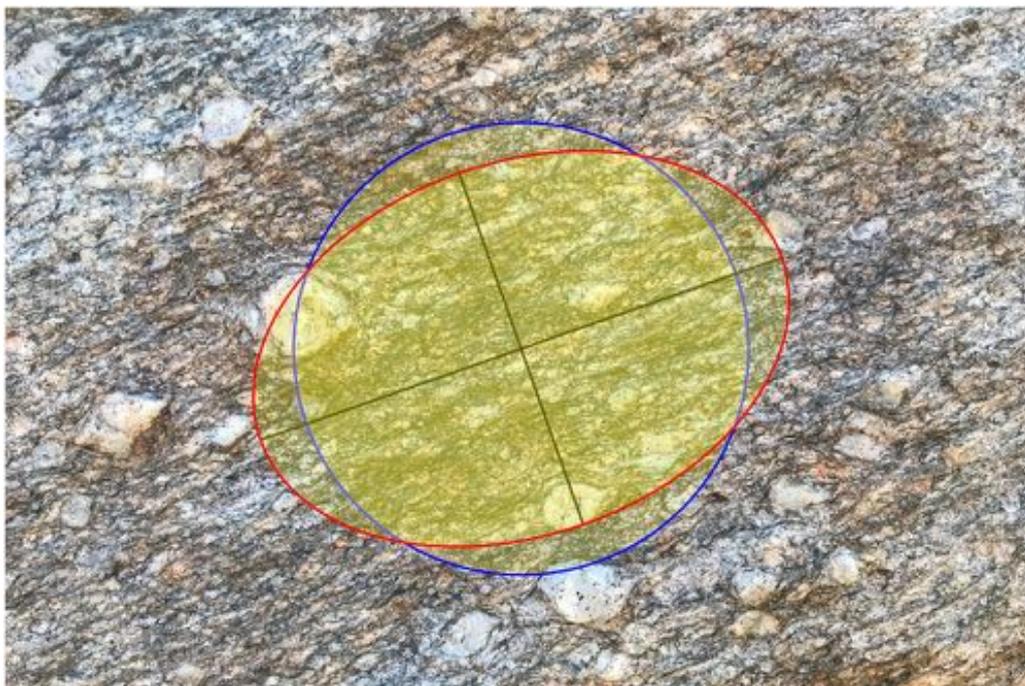


Figure 8.1: Example of an edge fabric ellipse using image A of Glazner and Walker (2020, Figure 1, and Supplementary Materials), a deformed granite from the Inyo Range, California. The calculation was done using the *Sobel* and *Lightness* options (Table 8.1), on the original image with a width of 3000 pixels. The blue circle is a reference circle with the same area.

ratio is equal to the square root of the ratio of the edge gradient magnitudes, with the maximum fabric ellipse axis parallel to the minimum edge gradient axis.

Two options are available, the first is the choice of the kernels, Prewitt or Sobel. The Sobel kernels give greater weight to adjacent pixels, and may produce better results (less noise) than the Prewitt. A second option is the choice of the grayscale conversion. The *Lightness* model is a gamma corrected lightness where 0 is black and 65535 is white. This should give the widest range of values to compare over the image. The *Grayscale* model converts the image after gamma expansion to a weighted RGB grayscale from 0 to 255. Gamma correction takes into account that the color space is non-linear, allowing a greater range of values to be included. The images are analyzed at full resolution and require two passes, so, for example, a 3000 by 2000 pixel image generates 6 million vectors, \vec{g} , and requires 12 million pixel operations.

Figure 8.1 is an example image, and Table 8.1 compares results to those reported by Glazner and Walker (2020, Figure 1, and Supplementary Materials) using *StraboTools* software. *StraboTools* uses Sobel kernels with images downsampled to 1000 pixels width. The samples are a deformed granite from the Inyo Range, California, (A), and a deformed image of granodiorite from Yosemite National Park, California, (B). The results are similar, the small variations (d_H) are likely due to differences in grayscale conversion and downsampling algorithms.

It must be kept in mind that the edge fabric ellipse is based only on gradients of image lightness. These gradients can be caused by many factors, including fractures, weathering patterns, shadows, and surface features such as lichens, so caution must be used in interpreting the result as a rock fabric, and, with much more caution, a strain. Nevertheless, this technique provides a rapid, quantitative, and reproducible estimate of rock fabric orientation and strength.

Sample		R	θ	ϕ	d_H
A	S	1.28	70	160	
	L	1.214		160.60	3.04
	G	1.225		160.26	2.52
B	S	1.11	30	120	
	L	1.107		125.47	1.14
	G	1.106		126.14	1.28

Table 8.1: Comparison of results calculated from images A and B of Glazner and Walker (2020, Figure 1, and Supplementary Materials). S - Glazner and Walker (2020) *StraboTools* software results, which uses Sobel kernels with images downsampled to 1000 pixels width. They report an azimuth, θ , which is converted to pitch, ϕ , for comparison. L - Calculation using the *Sobel* and *Lightness* options, G - Calculation using *Sobel* and *Grayscale* options. L and G are calculated using the original image width of 3000 pixels. d_H are the hyperbolic distances in degrees from the S result. d_H better represents the differences between the solutions, since ϕ at $R \approx 1$ has little significance (Section 6.2.3).

8.2 Filters and Edge Detection

Image analysis may allow better resolution of particle outlines, for example by applying contrast or edge detection filters (Efford, 2000; Parker, 2011). Some potentially useful filters are provided in *EllipseFit*, using the *Image Filters* and *Edge Detection* commands. Similar filters can be found in image software such as *ImageJ*, *MATLAB*, *Adobe Photoshop*, and *GIMP*.

8.2.1 Image Filters

Contrast - Linearly rescales the image pixels using contrast (gain) and lightness (bias) values. The range can also be thresholded using the black and white threshold sliders.

Normalize - Rescales the pixels to use the whole available range of values, making dark colors darkest possible and light colors as light as possible.

Threshold - Sets pixels with intensities below the black threshold to black, and pixels with intensities above the white threshold to white.

Remap - Does a linear rescaling by setting the gain and bias to rescale the image pixels to the black and white thresholding values.

Lightness - Increases or decreases the perceived lightness of the image.

Intensity - Increases or decreases the values of the pixel intensities.

Grayscale - Converts color values to grayscale.

Negative - Inverts the pixel values.

Sharpen - Adds contrast between pixels to enhance edges.

Blur - Applies a radial blur applies a blur, so each pixel is merged with pixels within the specified radius.

Median - Computes the median of colors around each pixel.

Convert BW - Converts pixels with low intensities to black, and pixels with high intensities to white.

Invert BW - Converts pixels with low intensities to white, and pixels with high intensities to black.

8.2.2 Edge Detection

Laplacian - Convolves the pixels by a symmetric kernel to approximate the second-order derivative of the intensity.

Contour - Computes a contour, as if the image was drawn with a 2 pixels-wide black pencil.

Prewitt - Convolves the pixels by a pair of asymmetric kernels to enhance the gradient in the x and y directions.

Sobel - Convolves the pixels by a pair of asymmetric kernels to enhance the gradient in the x and y directions. This is similar to Prewitt, but gives a greater weight to adjacent pixels, and may produce less noise.

Kirsch - Convolves the pixels using eight asymmetric kernels to enhance the gradients.

DoG - Performs weighted difference of Gaussian edge detection.

Acknowledgements

I thank Y. Shan, P-Y.F. Robin, K. Burmeister, S. Treagus, G. Mitra, S. Wojtal, H. Fossen, P. Karabinos, M. Mookerjee, J. Davis, W. Dunn, E. Erslev, Y. Kuiper, R. Bauer, D. Wise, D. Czeck, N. Mancktelow, J.M. Crespi, B.M. Klemm, J. Robinson, J. Waldron, J.R. Webber, and J. Singleton for suggestions, comments, discussions, and encouragement. I especially thank R. Twiss, W. Means, and P.J. Hudleston, mentors whose clear thinking and quantitative approaches inspired me as a student.

Thanks to Jinxi Li (University of Technology Sichuan, China), Julian Mecklenburgh (University of Manchester, UK), Scott Wilkerson (DePauw University, IN), Sebastian Dirringer (SUNY New Paltz), Nate Eichelberger (Princeton University), Raphaël Gottardi (University of Louisiana), Laurence N. Warr (Ernst Moritz Arndt University of Greifswald), Chirantan Parui (IISER, West Bengal), Gabriele Casale (Appalachian State University), Christopher Dale Loyacano (University of Memphis), Graham D.M. Andrews (West Virginia University), Pragnyadipta Sen (University of Virginia), Oxana Befous (University of Hamburg), and Patrick McCarthy (California State University, Sacramento) for suggestions and bug reports.

References

- Bachmann F, Hielscher R, Schaeben H (2011) Grain detection from 2d and 3d EBSD data-Specification of the MTEX algorithm. *Ultramicroscopy* 111(12):1720–1733, ISSN 03043991
- Brandon MT (1995) Analysis of geologic strain data in strain-magnitude space. *Journal of Structural Geology* 17(10):1375–1385, ISSN 01918141
- Burmeister K C, Harrison M J, Marshak S, Ferré E C, Bannister R A, Kodama K P (2009) Comparison of Fry strain ellipse and AMS ellipsoid trends to tectonic fabric trends in very low-strain sandstone of the Appalachian fold-thrust belt. *Journal of Structural Geology* 31(9):1028–1038, ISSN 01918141
- Cardiel N (2009) Data boundary fitting using a generalized least-squares method. *Monthly Notices of the Royal Astronomical Society* 396(2):680–695, ISSN 00358711
- Cashman K V, Marsh B D (1988) Crystal size distribution (csd) in rocks and the kinetics and dynamics of crystallisation ii. makaopuhi lava lake. *Contributions to Mineralogy and Petrology* 99:292–305
- Cloos E (1947) Oolite deformation in the south mountain fold, maryland. *Geological Society of America Bulletin* 58:843–918
- Cloos E (1971) *Microtectonics along the western edge of the Blue Ridge, Maryland and Virginia*. Baltimore and London: The Johns Hopkins Press
- Crespi J M (1986) Some guidelines for the practical application of fry's method of strain analysis. *Journal of Structural Geology* 16:1327–1330
- Davis G H, Reynolds S J, Kluth C F (2011) *Structural geology of rocks and regions*. Wiley, 3 edition
- Davis J C (1986) *Statistics and Data Analysis in Geology*. New York: Wiley, 2 edition
- Dirringer S, Vollmer F W (2013) A test of the analytical wellman and mean polygon moment ellipse methods of strain analysis using a sample of deformed ordoevian graptoliferous slate from the taconic orogen, new york. *Geological Society of America Abstracts with Programs* 52:247
- Dunne W M, Onasch C M, Williams R T (1990) The problem of strain-marker centers and the fry method. *Journal of Structural Geology* 12:933–1990
- Dunnet D (1969) A technique of finite strain analysis using elliptical particle. *Tectonophysics* 7:117–136
- Efford N (2000) *Digital Image Processing - A Practical Introduction Using Java*. Pearson
- Efron B (1979) Bootstrap methods: Another look at the jackknife. *Annals of Statistics* 7:1–26
- Elliott D (1970) Determination of finite strain and initial shape from deformed elliptical objects. *Geological Society of America Bulletin* 81:2221–2236
- Erslev E A (1988) Normalized center-to-center strain analysis of packed aggregates. *Journal of Structural Geology* 10:201–209
- Erslev E A, Ge H (1990) Least squares center-to-center and mean object ellipse fabric analysis. *Journal of Structural Geology* 8:1047–1059
- Fisher N, Lewis T, Embleton B (1987) *Statistical Analysis of Spherical Data*. Cambridge University Press
- Fitzgibbon A W, Pilu M, Fisher R B (1996) Direct least squares fitting of ellipses. *IEEE Transactions on Pattern Analysis and Machine Intelligence* 21:476–480
- Flinn D (1956) On the deformation of the Funzie conglomerate, Fetlar, Shetland. *The Journal of Geology* 64(5):480–505
- Fossen H (1988) The ulriken gneiss complex and the rundemanen formation: a basement-cover relationship in the bergen arcs, west norway. *Norges Geologiske Undersøkelse Bulletin* 412:67–86
- Fossen H (2016) *Structural Geology*. Cambridge: Cambridge University Press, 2 edition
- Fry N (1979) Random point distributions and strain measurement in rocks. *Tectonophysics* 60:806–807
- Glazner A, Walker J D (2020) StraboTools: A Mobile App for Quantifying Fabric in Geology. *GSA Today* 30, ISSN 10525173
- Goldstein A, Knight J, Kimball K (1998) Deformed graptolites, finite strain and volume loss during cleavage formation in rocks of the taconic slate belt, New York and Vermont, U.S.A. *Journal of Structural Geology* 20(12):1769–1782, ISSN 01918141
- Haliř R, Flusser J (1998) Numerically stable direct least squares fitting of ellipses. *Proc 6th International Conference in Central Europe on Computer Graphics and Visualization 98 (WSCG)*:125–132
- Hanna S S, Fry N (1979) A comparison of methods of strain determination in rocks from southwest dyfed (pembrokeshire) and adjacent areas. *Journal of Structural Geology* 2:155–162
- Heckbert P S (1990) A seed fill algorithm. In Glassner A S, editor, *Graphics Gems*, chapter 4, AP Professional, 275–277
- Higgins M D (2000) Measurement of crystal size distributions. *American Mineralogist* 85:1105–1116
- Hobbs B, Means W D, Williams P F (1976) *An Outline of Structural Geology*. New York: Wiley
- Holst T B (1982) The role of initial fabric on strain determination from deformed ellipsoidal objects. *Tectonics* 82:329–350
- Holst T B, Fossen H (1987) Strain distribution in a fold in the west norwegian caledonides. *Journal of Structural Geology* 9:915–924
- Hossack J R (1968) Pebble deformation and thrusting in the bygdin area (southern norway). *Tectonophysics* 5(315-339)
- Hossain K M (1979) Determination of strain from stretched belemnites. *Tectonophysics* 60(3):279–288, ISSN 0040-1951
- Hsu T C (1966) The characteristics of coaxial and non-coaxial strain paths. *The Journal of Strain Analysis for Engineering Design* 1(3):216–222
- Kamb W B (1959) Ice petrofabric observations from Blue Glacier, Washington, in relation to theory and experiment. *Journal of Geophysical Research* 64(11):1891–1909, ISSN 0148-0227
- Klemm B, Burmeister K, Giorgis S, Vollmer F W (2013) Post-folding vertical flattening strain fabrics in mechanically rigid rocks deformed under sub-metamorphic conditions in a foreland fold-thrust belt. *Geological Society of America Abstracts with Programs* 45(5)

- Klemm B M, Vollmer F W, Burmeister K (2012) Preliminary finite strain and fabric analysis of conglomerate from the shawangunk formation; northern appalachian fold-thrust belt, hudson valley, new york. *Geological Society of America Abstracts with Programs* 44(7):241
- Kumar R, Srivastava D C, Ojha A K (2014) A comparison of the methods for objective strain estimation from the fry plots. *Journal of Structural Geology* 63:76–90
- Launeau P, Robin P Y F (2005) Determination of fabric and strain ellipsoids from measured sectional ellipses - Implementation and applications. *Journal of Structural Geology* 27(12):2223–2233, ISSN 01918141
- Letsch D (2016) Swiss contributions to mid-nineteenth century tectonic research: A step backwards or the prologue to the nappe tectonics revolution? *Geological Society London Special Publications* 442:105–116
- Lisle R (1985) The use of the orientation tensor for the description and statistical testing of fabrics. *Journal of Structural Geology* 7:115–117
- Lisle R J (2010) Strain analysis from point fabric patterns: an objective variant of the fry method. *Journal of Structural Geology* 32:975–981
- Lloyd G E, Ferguson C C (1989) Belemnites, strain analysis and regional tectonics: a critical appraisal. *Tectonophysics* 168(4):239–253, ISSN 0040-1951
- Malvern L E (1969) *Introduction to the mechanics of a continuous medium*. New Jersey: Prentice-Hall, Inc
- Marsh B (1988) Crystal size distribution (csd) in rocks and the kinetics and dynamics of crystallization i. theory. *Contributions to Mineralogy and Petrology* 99:277–291
- Marshak S, Mitra G (1988) *Basic Methods of Structural Geology*. Prentice Hall
- McNaught M A (1994) Modifying the normalized fry method for aggregates of non-elliptical grains. *Journal of Structural Geology* 16:493–503
- McNaught M A (2002) Estimating uncertainty in normalized fry plots using a bootstrap approach. *Journal of Structural Geology* 24:311–322
- Means W D (1976) *Stress and strain: basic concepts of continuum mechanics for geologists*. New York: Springer-Verlag
- Means W D (1983) Microstructure and micromotion in recrystallization flow of octochloropropane: a first look. *Geologische Rundschau* 72:511–528.
- Mitra S (1978) Microscopic deformation mechanisms and flow laws in quartzites within the south mountain anticline. *Journal of Geology* 86:129–152
- Mookerjee M, Nickleach S (2011) Three-dimensional strain analysis using Mathematica. *Journal of Structural Geology* 33(10):1467–1476, ISSN 01918141
- Mookerjee M, Peek S (2014) Evaluating the effectiveness of Flinn's k-value versus Lode's ratio. *Journal of Structural Geology* 68(PA):33–43, ISSN 01918141
- Mulchrone K F (2002) Application of delaunay triangulation to the nearest neighbour method of strain analysis. *Journal of Structural Geology* 25:689–702
- Mulchrone K F (2013) Fitting the void: Data boundaries, point distributions and strain analysis. *Journal of Structural Geology* 46:22–33, ISSN 01918141
- Mulchrone K F, Choudhury R (2004) Fitting an ellipse to an arbitrary shape: implications for strain analysis. *Journal of Structural Geology* 26:143–153
- Mulchrone K F, O'Sullivan F, Meere P A (2003) Finite strain estimation using the mean radial length of elliptical objects with bootstrap confidence intervals. *Journal of Structural Geology* 25(4):529–539, ISSN 01918141
- Mulchrone K F, Pastor-Galán D, Gutiérrez-Alonso G (2013) Mathematica code for least-squares cone fitting and equal-area stereonet representation. *Computers and Geosciences* 54:203–210, ISSN 00983004
- Nadai A (1963) *Theory of Flow and Fracture of Solids - Engineering Societies Monographs*. New York: McGraw-Hill
- Onasch C M (1986) Ability of the fry method to characterize pressure-solution deformation. *Tectonophysics* 122:187–193
- Owens W H (1984) The calculation of a best-fit ellipsoid from elliptical sections on arbitrarily orientated planes. *Journal of Structural Geology* 6:571–578
- Parker J (2011) *Algorithms for Image Processing and Computer Vision*. Wiley, 2 edition
- Pollard D D, Fletcher R C (2005) *Fundamentals of Structural Geology*. Cambridge: Cambridge University Press
- Preparata F P, Shamos M I (1985) *Computational Geometry*. New York: Springer-Verlag
- Press W H, Teukolsky S A, Vetterling W T, Flannery B P (2007) *Numerical Recipes: The Art of Scientific Computing*, 3rd edition. Cambridge University Press, Cambridge, 1235 p. Press, W.H, Teukolsky, S.A., Vetterling, W.T., and Flannery, B.P., 2007. *Numerical Recipes: The Art of Scientific Computing*. Cambridge: Cambridge University Press, 3 edition
- Ragan D (2009) *Structural Geology: An Introduction to Geometrical Techniques*. Cambridge: Cambridge University Press, 4 edition
- Ragan D M (1985) *Structural Geology, An Introduction to Geometrical Techniques*. John Wiley and Sons, Inc, 3 edition
- Ramsay J G (1967) *Folding and Fracturing of Rocks*. New York: McGraw-Hill Book Company
- Ramsay J G, Huber M I (1983) *The Techniques of Modern Structural Geology: Volume 1: Strain. Analysis*. London: Academic Press
- Reddy Vinta B S S, Srivastava D C (2012) Rapid extraction of central vacancy by image-analysis of Fry plots. *Journal of Structural Geology* 40:44–53, ISSN 01918141
- Reynolds W F (1993) Hyperbolic geometry on a hyperboloid. *American Mathematical Monthly* 100(5):442–455
- Robin P F (2002) Determination of fabric and strain ellipsoids from measured sectional ellipses – theory. *Journal of Structural Geology* 24:531–544
- Robin P Y F (2019) 'Strain probe': Best-fitting a homogeneous strain to the motions of scattered points. *Journal of Structural Geology* 124(December 2018):211–224, ISSN 01918141
- Schmidt W (1925) Gefügestatistik. *Tschermaks Mineralogische und Petrographische Mitteilungen* 38:392–423
- Shan Y (2008) An analytical approach for determining strain ellipsoids from measurements on planar surfaces. *Journal of Structural Geology* 30:539–546
- Shan Y, Xiao W (2011) A statistical examination of the fry method of strain analysis. *Journal of Structural Geology* 33:1000–1009
- Shimamoto T, Ikeda Y (1976) A simple algebraic method for strain estimation from ellipsoidal objects. *Tectonophysics* 36:315–337
- Snyder J P (1987) *Map projections: A working manual*. Professional Paper 1395, United States Geological Survey
- Steger C (1996) On the calculation of moments of polygons. Technical Report FGBV-96-05, Technische Universität München
- Twiss R J, Moores E M (2007) *Structural Geology*. New York: W.H. Freeman, 2 edition
- Van der Pluijm B, Marshak S (2004) *Earth Structure*. New York: W. W. Norton, 2 edition
- Vincenty T (1975) Direct and inverse solutions of geodesics on the ellipsoid with application of nested equation. *Survey Review* XXII(179):88–93
- Vollmer F W (1995) C program for automatic contouring of spherical orientation data using a modified Kamb method. *Computers & Geosciences* 21(1):31–49, ISSN 00983004
- Vollmer F W (1998) Ellipsefit 1 strain analysis program
- Vollmer F W (2010) A comparison of ellipse-fitting techniques for two and three-dimensional strain analysis, and their implementation in an integrated computer program designed for field-based studies. *EOS, American Geophysical Union Transactions* :T21B–2166
- Vollmer F W (2011a) Automatic contouring of two-dimensional finite strain data on the unit hyperboloid and the use of hyperboloidal stereographic, equal-area and other projections for strain analysis. *Geological Society of America Abstracts with Programs* 43(5):605
- Vollmer F W (2011b) Best-fit strain from multiple angles of shear and implementation in a computer program for geological strain analysis. *Geological Society of America Abstracts with Programs* 43(1):147
- Vollmer F W (2015) Orient 3: A new integrated software program for orientation data analysis, kinematic analysis, spherical projections, and schmidt plots. *Geological Society of America Abstracts with Programs* 47(7):49
- Vollmer F W (2018a) Automated calculation and error analysis of fabric and strain ellipsoids from multiple section data. *Geological Society of America Abstracts with Programs* 50(6)

- Vollmer F W (2018b) Automatic contouring of geologic fabric and finite strain data on the unit hyperboloid. *Computers & Geosciences* 115:134–142
- Vollmer F W (2019) Calculation of the best-fit homogeneous strain from a displacement field using displacement stretch plot and strain probe theory. *Geological Society of America Abstracts with Programs* 51(5)
- Waldron J W F (1988) Determination of finite strain in bedding surfaces using sedimentary structures and trace fossils: a comparison of techniques. *Journal of Structural Geology* 10:273–281
- Waldron J W F, Wallace K D (2007) Objective fitting of ellipses in the centre-to-centre (fry) method of strain analysis. *Journal of Structural Geology* 29:1430–1444
- Webber J R, Klepeis K A (2018) An objective approach to the quantification of strain in three-dimensions with consideration of error assessment. *Geological Society of America Abstracts with Programs* 50
- Wellman H G (1962) A graphic method for analyzing fossil distortion caused by tectonic deformation. *Geological Magazine* 99.:384–352
- Wheeler J (1986) Average properties of ellipsoidal fabrics: implications for two- and three-dimensional methods of strain analysis. *Tectonophysics* 126:259–270
- Yamaji A (2008) Theories of strain analysis from shape fabrics: A perspective using hyperbolic geometry. *Journal of Structural Geology* 30:1451–1465
- Yamaji A (2013) Comparison of methods of algebraic strain estimation from rf/ϕ data: A unified theory of 2d strain analysis. *Journal of Structural Geology* 49:4–12
- Yamaji A, Maeda H (2013) Determination of 2d strain from a fragmented single ammonoid. *Island Arc* 22:126–132
- Yonkee A W, Czeck D M, Nachbor A C, Barszewski C, Pantone S, Balgord E A, Johnson K R (2013) Strain accumulation and fluid-rock interaction in a naturally deformed diamictite, Willard thrust system, Utah (USA): Implications for crustal rheology and strain softening. *Journal of Structural Geology* 50:91–118, ISSN 01918141
- Zingg (1935) Beitrag zur schotteranalyse. *Schweizerische Mineralogische und Petrographische Mitteilungen* 15:39–140

This page intentionally left blank

